Chem Soc Rev

ROYAL SOCIETY OF CHEMISTRY

REVIEW ARTICLE

View Article Online
View Journal | View Issue

Cite this: *Chem. Soc. Rev.*, 2025, **54**, 10796

Efficient green synthesis of ammonia: from mechanistic understanding to reactor design for potential production

Zhenhui Kou,[a] Dong Shi,[a] Bin Yang,[a] Zhongjian Li,[a] Qinghua Zhang,[a] Jianguo Lu,[e] Tao Zhang,[c] Lecheng Lei,[a] Yuanyuan Li,[f] Liming Dai *[d] and Yang Hou *[ab]

Received 8th September 2025

DOI: 10.1039/d5cs00969c

rsc.li/chem-soc-rev

Ammonia (NH_3), one of the world's most vital chemicals and energy carriers, has attracted wide attention. Currently, NH_3 is mainly produced using the traditional, energy-intensive Haber–Bosch (H–B) technology, which has a large impact on the environment. Therefore, developing a low-cost, high-efficiency, and eco-friendly way to produce NH_3 is highly desirable. Photo-, electro-, photoelectro-, and alkali–metal-mediated catalytic reactions powered by renewable and clean energy under ambient conditions offer alternatives to the H–B process and have recently gained significant interest. However, efficient nitrogen reduction is a key requirement, limiting the selectivity and activity for the green synthesis of NH_3 because the N_2 activation process in a green catalytic system is difficult to complete due to its thermodynamic instability and chemical inertness. Compared to the reduction of N_2, the catalytic reduction of some soluble and harmful high-valent sources (*e.g.*, NO, NO_2^-, and NO_3^-) is considered an effective method for increasing NH_3 synthesis efficiency. This review article focuses on the important features of the green catalytic conversion of multiple nitrogen resources into NH_3 by summarizing the fundamental mechanistic understanding, catalytic descriptors, and current advances, along with the various catalysts used for these conversion strategies and their structure–activity relationships. Meanwhile, opportunities and prospects for reactor design and construction for potential NH_3 production at high current densities are also discussed, focusing on achieving a high yield rate, Faraday efficiency, and energy efficiency. This will provide valuable guidance for constructing catalysts and optimizing reaction systems that can meet the needs of practical applications.

1. Introduction

Ammonia (NH_3) is an essential raw material for fertilizers, chemicals, and medical products, playing a important role in the development and progress of society.[1–3] Specifically, a sufficient amount of NH_3 is required to produce nitrogen-based fertilizers like NH_4NO_3 and urea, as well as other nitrogenous compounds, leading to a seven- to eight-fold increase in food production.[4–6] Beyond its primary uses, NH_3 serves as a critical precursor in diverse sectors, including national defense (explosives), plastics, dyes, synthetic fibers, and resins.[7–10] Furthermore, NH_3 is also an ideal eco-friendly energy storage species and a carbon-free energy carrier[11–13] because of its large hydrogen content (17.6 wt%) and high energy density (4.32 kWh L^{-1} or 6.25 kWh kg^{-1})[14] and the ease with which it can be liquefied for storage and transportation.[10,15] Therefore, research into NH_3 preparation pathways is attractive.

Currently, the Haber–Bosch (H–B) process is the primary method for large-scale NH_3 production, converting N_2 and H_2 into NH_3.[16–18] However, the H–B process still has numerous problems. First, the sluggish exothermic reaction ($N_2 + 3H_2 \rightarrow 2NH_3$, $\Delta H_{298K} = -45.9$ kJ mol^{-1}, $\Delta G_{298K} = -16.4$ kJ mol^{-1}) between inert N_2 and H_2 requires harsh conditions.[19–23] Second, the H–B technique consumes about 1% of the world's energy supply and leaves a major carbon footprint.[24,25] Third, the

---

[a] *Key Laboratory of Biomass Chemical Engineering of Ministry of Education, College of Chemical and Biological Engineering, Zhejiang University, Hangzhou 310027, China. E-mail: yhou@zju.edu.cn*

[b] *Zhejiang University Hydrogen Energy Institute, Hangzhou 310027, China*

[c] *Key Laboratory of Marine Materials and Related Technologies, Ningbo Institute of Materials Technology and Engineering, Chinese Academy of Sciences, Ningbo 315201, China*

[d] *ARC Centre of Excellence for Carbon Science and Innovation, Australian Carbon Materials Centre, School of Chemical Engineering, The University of New South Wales Sydney, Sydney, NSW 2052, Australia. E-mail: l.dai@unsw.edu.au*

[e] *State Key Laboratory of Silicon and Advanced Semiconductor Materials, School of Materials Science and Engineering, Zhejiang University, Hangzhou 310027, China*

[f] *Wallenberg Wood Science Center, Department of Fiber and Polymer Technology, KTH Royal Institute of Technology, Stockholm, 10044, Sweden*

hydrogen produced through steam methane reforming or coal gasification has led to more than 420 million tons of carbon dioxide emissions.[26,27] These negative factors make the H–B method an energy-intensive industrial technique. Additionally, the efficiency of the H–B technology is low, with an NH_3 yield of about 15–20% in a single pass, although a 97% yield can be achieved by recycling the gas reactants multiple times.[28] Therefore, it is very important to overcome these limitations. Considering the increasing global energy demand and environmental concerns, the scientific community should focus on how sustainable energy can support reactions at mild temperatures and pressures and how to synthesize NH_3 on a large scale using this green conversion pathway. Therefore, developing green synthesis technologies is important.

Inspired by biological N_2 fixation,[29] where many plants use nitrogenase to convert N_2 from the air into NH_3 fertilizer under sunlight for self-growth,[30] recent studies show that nitrogenase displays photocatalytic conversion activity and plays a significant role in NH_3 synthesis.[31] However, due to the unsatisfactory conversion rate of photo-assisted N_2 fixation, recent work has mainly focused on developing more efficient strategies. Using renewable electricity instead of fossil fuels has been widely accepted.[16] An efficient technology for obtaining green NH_3 is to use the electrocatalytic water splitting process, which produces the solvent and proton source.[32] Its raw materials are H_2O and N_2, and the overall reaction is $3H_2O + N_2 \rightarrow 2NH_3 + 3/2O_2$, driven only by renewable electricity.[31] The efficient transformation of renewable energy and the conversion of clean electricity into chemical energy are critical for energy and environmental protection.[33–35] Therefore, this has aroused widespread interest among scientists worldwide. More importantly, photoelectrochemical, alkali metal-mediated, and other conversion technologies have also been proposed to further improve or optimize the Faraday efficiency (FE), energy efficiency (EE), current density, reaction speed, and yield rate of NH_3.[36–42]

Furthermore, to facilitate the practical applications of green catalytic conversion methods, the United States Department of Energy has set key parameters as benchmarks. The current FE remains at 60%, a value below the target of over 90%. Meanwhile, the current activity indexes for electrocatalytic NH_3 synthesis are two to three orders of magnitude below the target standards.[20,43,44]

Therefore, despite ongoing research, green NH_3 synthesis is far from large-scale applications for the following reasons: (a) the thermodynamic energy barrier of the competing hydrogen evolution reaction (HER) is lower than that of the NH_3 synthesis reaction.[45] (b) The chemically inert N_2 molecule has a strong $N\equiv N$ bond energy (941 kJ mol^{-1}), requiring a massive energy input to cleave the first bond. (c) N_2 molecules are electronically stable due to a high ionization energy of 1525 kJ mol^{-1} and a large energy gap of 1044 kJ mol^{-1}, which makes transferring an electron to N_2 molecules kinetically difficult. (d) N_2 protonation is the rate-determining step (RDS) because N_2 has a lower proton affinity compared to reaction intermediates like diazene (N_2H_2) and hydrazine (N_2H_4).[6,20,46] (e) The limited solubility of N_2 molecules in aqueous solutions generates a low current density and a low production rate.[47,48] Thus, building suitable catalysts to activate N_2 molecules, through methods such as doping engineering, defect engineering, crystal facet engineering, and dimensional engineering,[49–51] is the first step for high-efficiency NH_3 production.

In addition to constructing efficient catalysts, using alternative nitrogen sources, such as nitric oxide or nitrogen dioxide (NO or NO_2) with low dissociation energy and nitrate or nitrite (NO_3^-, NO_2^-) with high solubility, is considered an effective way to decrease energy consumption and increase the production rate

Zhenhui Kou

Zhenhui Kou is completing his PhD degree under Prof. Yang Hou at the College of Chemical and Biological Engineering at Zhejiang University. His current interests focus on electrocatalytic reduction reaction technology.

Liming Dai

Prof. Liming Dai is a Professor at the School of Chemical Engineering at the University of New South Wales. His current research mainly focuses on the synthesis, functionalization, and device fabrication of conjugated polymers and carbon nanomaterials for energy-related and biomedical applications.

Yang Hou

Prof. Yang Hou is a Professor at the College of Chemical and Biological Engineering at Zhejiang University. His current research mainly focuses on the design and synthesis of carbon-based materials for energy and environmental applications.

and selectivity of NH_3.[7,21,52,53] Among these, NO is one of the major pollutants produced by the burning of fossil fuels.[54,55] As its concentration increases, it causes serious ecological problems such as acid rain, ozone depletion, and haze,[56] with potential risks about 300 times greater than those associated with CO_2 emissions. Meanwhile, the high solubility of NO_x^- makes it difficult to remove from water, resulting in a series of physiological diseases.[58,59] The contaminant NO_2^- can also cause cancer,[60] while NO_3^- can disrupt the human endocrine system. The World Health Organization has recommended a maximum contaminant level of 50 mg L^{-1} in drinking water to minimize the adverse health effects of nitrogen oxides.[57] Thus, in addition to alleviating energy and resource shortages, reducing NO, NO_2^-, and NO_3^- to NH_3 is very beneficial for controlling wastewater pollution, as these processes involve the low dissociation energy (204 kJ mol^{-1}) of N$=$O bonds.[61] Moreover, NO_3^- and NO_2^- usually tend to be adsorbed and activated by catalytic materials, which effectively settle the insoluble difficulty of N_2, setting the fundamental for large-scale NH_3 synthesis.[21] However, there are also certain limitations. Take the NO_3^- reduction reaction (NO_3RR) ($NO_3^- + 9H^+ + 8e^- \rightarrow NH_3 + 3H_2O$) as an example. Undesired by-products like NO_2^-, N_2 and N_2H_4 are inevitably produced during the process.[62,63] The selectivity of the NO_3RR depends on the overpotential and current density.[9,64] Therefore, a timely summary of various catalysts in NH_3 synthesis will not only improve the understanding of current progress but also inspire the construction of advanced catalysts, achieving the effect of 'killing two birds with one stone'. Meanwhile, the innovation of catalytic materials and reactors also plays an important role in reaction system engineering, and further optimization of synthetic NH_3 systems requires innovation in reactor engineering. Thus, an advanced synthetic NH_3 system can only be achieved through joint optimization and innovation. This article will focus on developing high-performance reaction units to minimize the mass transfer limit of the reactants, thereby significantly improving key parameters such as system current density, FE, EE, and running time. Finally, the transformation of green synthetic NH_3 technology from the laboratory to an industrial scale is expected to be realized.

To our knowledge, many review papers have been published on this popular topic, covering NH_3 synthesis methods, types of advanced catalysts, structure–activity relationships, reaction pathways, and mechanisms.[20,28,44,65–70] However, most of these reviews focus on a specific topic, limited to a single catalytic conversion strategy (*e.g.*, photocatalytic, electrocatalytic, or thermocatalytic), a specific electrocatalyst (*e.g.*, two-dimensional monoelemental materials, transition metal dichalcogenides, MXenes, or molecular catalysts), or one type of nitrogen source (*e.g.*, nitrogen, nitric oxide, nitrite, or nitrate). In recent decades, much research has been done to develop promising green NH_3 synthesis by designing high-performance catalysts using theoretical calculations and advanced synthesis technologies, which requires a timely, comprehensive review of this rapidly developing field. Therefore, instead of focusing on a single topic as in previous reviews, this article presents a comprehensive review covering recent research progress in value-added NH_3 production through photo-, electro-, photo/electrochemical, lithium-mediated, calcium-mediated and other advanced green pathways. We will provide an overview of the history and fundamental science behind traditional NH_3 synthesis technology and its existing problems, along with the outlook on green NH_3, given the high global demand for ammonia. Special emphasis will be placed on the state-of-the-art catalytic technology, material design and preparation from different nitrogen sources (*e.g.*, nitrogen, nitric oxide, nitrite, or nitrate), structural characterization, and performance evaluation, as well as the main factors influencing selectivity and activity, the development of reactors for green NH_3 synthesis, and the associated theoretical calculations on reaction mechanisms for different catalysts. Finally, the outlook on NH_3 synthesis using multiple catalysts, including challenges and opportunities for developing new catalysts, novel catalytic methods, and reactor devices, provided in recently reported *operando* fundamental studies, and potential industrial applications will be summarized and discussed (Fig. 1).

2. Fundamentals of ammonia synthesis

To provide comprehensive and systematic information about green NH_3 synthesis, a thorough and fundamental summary of the topic is necessary. In this section, we briefly summarize the reaction mechanisms and specific pathways for different nitrogen resources (N_2, NO, NO_2^-, and NO_3^-), including the multiple intermediates, conversion steps, and reaction pathways. After explaining the basic mechanism, we will comprehensively summarize various methods for NH_3 synthesis, including the design and construction of reactors, testing methods for NH_3 products, error removal strategies, and performance evaluation criteria. Finally, we will describe in detail the various catalytic activity descriptors, such as FE, NH_3 yield, EE, and stability, used to evaluate catalytic performance in real time to further optimize the experiments.

2.1 Mechanism of ammonia synthesis

2.1.1 Mechanism of the nitrogen reduction reaction. There are several possible mechanisms (dissociative, associative, and Mars–van Krevelen (MvK) pathway) for converting N_2 to NH_3.[27,48,71,72] In the dissociative mechanism, the N$\equiv$N bonds break at high temperature and pressure to produce NH_3. In contrast, in the associative mechanism, the N$\equiv$N bonds are not completely broken until the first NH_3 molecule is released. Specifically, the associative pathway includes distal, alternating, and enzymatic hydrogenation. In the distal and alternating pathways, N_2 molecules bind end-on to the catalyst's surface. In the distal mechanism, the distant N atom first combines with H to form $*NH_3$, while the other N atom does not combine with H until the first NH_3 molecule is released. In contrast, in the alternating pathway, the two N atoms are hydrogenated in turn before both NH_3 molecules are released at the same time. In the enzymatic pathway, the linear N_2 molecules are parallel to the electrode surface, where they react with H to produce the target products alternately or concurrently. Recently, the MvK pathway has also been proposed. In general, the production of NH_3

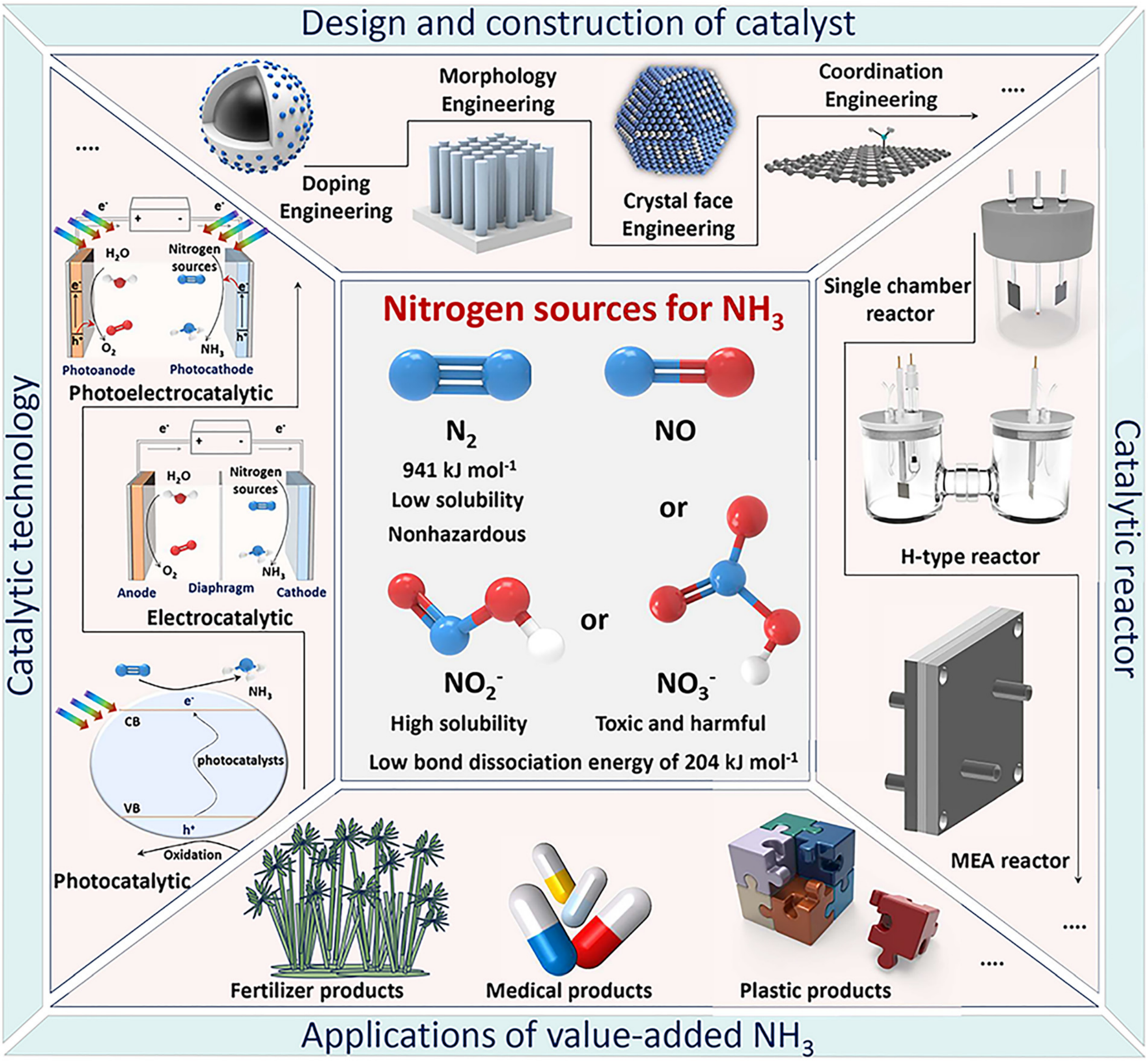

Fig. 1 Schematic illustration of efficient value-added NH_3 product synthesis by various green catalytic conversion technologies from different nitrogen sources.

via transition metal nitrides (TMNs) usually follows the MvK pathway. In the MvK mechanism, N atoms from the TMNs are reduced to NH_3 and external N_2 fills the vacancy to complete the recovery of the TMNs and begin a new NH_3 synthesis process.[73] Compared to other pathways, the MvK pathway greatly improves mass transfer kinetics and overcomes the poor solubility of N_2 molecules because the 'gas–liquid–solid' three-phase reaction is divided into 'liquid–solid' and 'gas–solid' reactions.[10] Currently, work investigating the catalytic mechanism usually depends on theoretical calculations, with a few actual experiments. Therefore, more *in situ* electrochemical characterization techniques can be used to determine the key conversion steps from N_2 to NH_3, such as *in situ* electrochemical scanning tunneling microscopy, *in situ* electrochemical atomic force microscopy, *in situ* Fourier transform infrared spectroscopy, *in situ* Raman spectroscopy, and *in situ* mass spectrometry, to track real-time changes in the surface structure of electrocatalysts and surface electrocatalytic processes. Furthermore, combining experiments with theoretical calculations can clearly explain the mechanism for a specific catalytic reaction process, which will have a major impact on the development of NH_3 synthesis.

2.1.2 Mechanism of the nitric oxide reduction reaction. NO is a vital intermediate in the nitrogen conversion process. However, the increased emission of NO has seriously disrupted the nitrogen cycle in nature, causing serious environmental problems and harm to all living systems.[74–76] Therefore, it is essential to develop green technology to control NO. The electrochemical NO reduction reaction (NORR), operating under mild conditions, offers a promising pathway and can even produce value-added NH_3.[77–79] To achieve a highly efficient process for converting NO-to-NH_3, understanding the fundamental mechanism of the NORR is key. Specifically, NH_3 and NH_2OH products are generated at relatively low potentials, N_2 products are formed at medium potentials, and N_2O products are generated at high potentials. At the same time, the competitive HER becomes dominant at 0 V *vs.* RHE.[80] The NORR in different potential ranges is shown in eqn (1)–(3).

$$NO + 5H^+ + 5e^- \rightarrow NH_3 + H_2O \quad (1)$$

$$2NO + 4H^+ + 4e^- \rightarrow N_2 + 2H_2O \quad (2)$$

$$2NO + 2H^+ + 2e^- \rightarrow N_2O + H_2O \quad (3)$$

Similar to the nitrogen reduction reaction (NRR), the NORR mechanism also includes dissociative and associative pathways.[76] In the dissociative mechanism, the N═O bond is first broken to produce *N and *O, and then the hydrogenation process begins. In contrast, during the associative pathway, NO is first hydrogenated to H_xNOH_y intermediates, which are then further protonated to NH_3. In these reaction paths, hydrogenation occurs through either the Tafel process, which involves the initial formation of adsorbed *H followed by surface hydrogenation, or the Heyrovsky process, where NO molecules and intermediates are directly protonated. Hence, there are four types of NORR mechanisms: Tafel combined with dissociative, Tafel combined with associative, Heyrovsky combined with dissociative, and Heyrovsky combined with associative. Among these, the hydrogenation steps in the associative Tafel and associative Heyrovsky mechanisms are further classified into distal or alternating pathways. In the distal pathway, O or N atoms are completely hydrogenated to H_2O or NH_3. In the alternating pathway, O or N atoms are alternately hydrogenated. The specific reaction processes are as follows in eqn (4)–(9):[78]

$$NO \rightarrow {}^*N + {}^*O \quad (4)$$

$$\text{Tafel-type: } H^+ + e^- \rightarrow {}^*H \quad (5)$$

$${}^*N + {}^*H \rightarrow {}^*NH \quad (6)$$

$$\text{Heyrovsky-type: } {}^*N + H^+ + e^- \rightarrow {}^*NH \quad (7)$$

$${}^*NH + {}^*H \rightarrow {}^*NH_2 \quad (8)$$

$${}^*NH_2 + {}^*H \rightarrow NH_3 \quad (9)$$

2.1.3 Mechanism of the ionic oxidized nitrogen oxyanion reduction reaction. Similar to NO species, the efficient conversion of harmful ionic oxidized nitrogen oxyanions (*e.g.*, NO_2^- and NO_3^-) can achieve both wastewater treatment and the electrosynthesis of NH_3 Therefore, clarifying the reaction mechanism from NO_x^- to NH_3 will contribute to the efficient green synthesis of NH_3.[76] The reduction of ionic oxidized forms of nitrogen is a complicated process involving the transfer of multiple electrons coupled with protons, which includes nitrogen species in different valence states. The detailed reaction is shown in eqn (10):

$$NO_3^- + 9H^+ + 8e^- \rightarrow NH_3 + 3H_2O \quad (10)$$

Specifically, taking the NO_3RR as an example, there are two ifferent pathways: indirect autocatalytic reduction and direct external-field-assisted catalytic reduction. A peracidic environment (pH < 0) and a high concentration (>1.0 mol L^{-1}) of NO_3^- favor the indirect autocatalytic pathway, where NO_3^- does not participate in the electron transfer process.[67,81–84] In contrast, direct external-field-assisted catalytic reduction, which usually operates at low concentrations (<1.0 mol L^{-1}),[76] involves an electron transfer process and includes two pathways: the first involves adsorbed *H and the second involves electrons from the catalysts. The first pathway involves reducing adsorbed H_2O molecules to produce *H, followed by the direct reduction of NO_3^- to NH_3 through a series of intermediate changes, such as $^*NO_2^-$, *NO, *N, *NH, and $^*NH_2$.[85] Notably, forming N–N bonds is kinetically less favorable than forming N–H bonds.[86] Therefore, the favorable adsorption of *H can boost NH_3 production. In the second pathway, the first step is the reduction of the intermediate $^*NO_3^-$ to $^*NO_2^-$.[87–89] Next, the $^*NO_2^-$ can be hydrogenated to produce *NO, which is then converted into NH_3 through a series of protonation processes. In this process, *HNO is formed first, which then converts[90] to $^*H_2NO$ and $^*NH_2OH$ and finally, the adsorbed $^*NH_2OH$ is reduced to NH_3.[67,84]

2.2 Research methods for ammonia synthesis

First, it is essential to thoroughly examine the reported overall NH_3 production, especially in aqueous systems, to confirm that it originates from N_2. Contamination from sources like catalysts, electrolytes, and reactants may result in false positives for NH_3 synthesis performance. At the same time, quantification techniques may not provide sufficient detection limits or consistency, since the NH_3 synthesis performance can easily be biased when NH_3 concentrations are not significantly higher than impurities. The high variance is likely a result of this.[91–93] Since NH_3 synthesis experiments can be ambiguous in identifying nitrogen sources, rigorous testing procedures have been proposed,[94–96] including performing NH_3 synthesis with non-catalyst electrodes, switching reactants from N_2 to Ar, and using quantitative isotope-labeled tests.[46] Second, other aspects of the reaction system may also compromise NH_3 production. A further study of catalytic reactor design and operation is especially vital, as this is essential for achieving a rational reaction system design and avoiding false positives. Under ideal operating conditions, modified reactor components have been shown to increase activity.[97,98] To minimize false positives, contamination-prone reactor components are removed, and rigorous reactor operation protocols are implemented.[91,92,99] Consequently, developing a reliable reactor along with strict and correct testing methods will improve the development of NH_3 synthesis.

2.2.1 Detection methods for ammonia synthesis. It is well known that the low NH_3 yield rate at ambient temperature and pressure means any contamination can easily influence the precision of experimental results. NH_3 is a common contaminant in chemicals and is prevalent in laboratory environments. Aqueous solutions and ordinary glassware can also accumulate NH_3 over time. At the same time, the use of unpurified catalysts, electrolytes, gases, and reactors also greatly impacts the accurate determination of NH_3. In addition, various sources of NH_3 pollutants, such as NO_x^- and gaseous reactants, cannot be ignored because they can be reduced to NH_3. To avoid inaccurate or incorrect detection of NH_3, effective removal strategies for N species and advanced NH_3 detection methods are key to obtaining true and reliable NH_3 synthesis performance.[68]

To avoid errors from nitrogen impurities, necessary purification measures must be taken, such as using sulfuric acid as an adsorbent to remove impurities from the raw reactants. Soluble nitrogen-containing impurities and poorly soluble nitrogen oxides also need to be removed *via* washing and selective reduction methods, respectively, followed by using H_2SO_4 to remove excess NH_3 species.[100] Poorly soluble impurities can also be oxidized to soluble impurities like NO using a $H_2O_2/S_2O_8^{2-}$ solution and then removed. If the reaction solvents or catalysts contain nitrogen impurities, they can be removed *via* heat treatment or alkali treatment. For ion exchange membranes used in a reactor, in addition to standard pretreatment, the treated membranes can be further sonicated in deionized water and dilute H_2SO_4.[101]

Besides, to precisely determine the catalytic activity and avoid false positive test results, the NH_3 produced must also be detected again using a reliable method. The most common detection methods include chemical detection using Nessler's reagent, indophenol blue, and salicylate, fluorometric detection, conductivity measurements, titrimetric methods, isotope labeling, ^1H NMR, electrode-based detection, ultraviolet and visible spectrophotometry, ion chromatography, and gas chromatography.[67,68] Notably, the detection results can be influenced by many kinds of metal ions, hydrazine, and carbonyl compounds. To minimize interference and prevent the formation of turbid samples when using the Nessler's reagent method,[102,103] Rochelle salt solution is usually added.[68] For the indophenol blue method, a blue product, indophenol, is produced through the reaction between NH_3, phenol, and hypochlorite in an alkaline solvent.[104] This method is less efficient when there is an excess of NH_3. In the salicylate method, sodium salicylate replaces phenol, which avoids producing toxic and volatile reaction products. Due to the low reactivity of salicylate, a higher concentration is needed to achieve sensitivity like the other methods.[105,106]

The fluorometric method mainly involves the interaction between NH_3, *o*-phthalaldehyde, and sulfite to produce a strongly fluorescent compound.[107] When the NH_3 concentration exceeds 1.0 μmol L^{-1}, the measured concentration and fluorescence intensity are not linearly related. Also, amines and amino acids can affect the results in aqueous solutions.[108,109]

Additionally, the conductivity method uses the reaction of NH_3 with acid, where the resulting salts reduce the solution's conductivity. A standard curve created with known NH_3 concentrations can be used to determine the exact NH_3 concentration in the solution based on the conductivity decrease.[110] However, the solution's conductivity can affect the detection.

For detecting NH_3 concentrations higher than 5.0 mg L^{-1}, the titrimetric method is often used. The method involves distilling the reaction solution and then titrating the NH_3 in the distilled products with an H_2SO_4 solution until the indicator changes color.[111] To determine if the prepared NH_3 comes from the N_2 reactants, especially for catalysts containing nitrogen, $^{15}N_2$ isotopic experiments are necessary. Additionally, ^1H NMR methods are required to detect and calibrate $^{15}NH_4^+$.[68,112]

Using a specific electrode to measure the NH_3 concentration is quick and simple,[113,114] including NH_3 sensing electrodes and NH_4^+ selective electrodes. The NH_3 sensing electrode consists of a membrane, a pH electrode, and a reference electrode, with an NH_4Cl solution used as the electrode solution. The pH of the solution being tested is increased by adding a base to convert NH_4^+ into NH_3 and the NH_3 then diffuses through the membrane until both sides have the same partial pressure. A standard curve generated with known NH_3 concentrations can be used to determine the NH_3 concentration in the internal solution, as the NH_3 concentration in the tested solution is proportional to the pH change in the electrode solution. The NH_4^+ selective electrode has a polyvinyl chloride film containing an NH_4^+ carrier and the pH of the solution being tested is decreased to convert NH_3 into NH_4^+. When a solution containing NH_4^+ meets the NH_4^+ selective electrode, a potential is generated on the membrane. Following this mechanism, a standard curve produced with known concentrations of NH_4^+ can be used to determine the concentration in the unknown solution.[6,109]

2.2.2 Reactors for ammonia synthesis. The main challenge in moving external-field-assisted NH_3 synthesis from laboratory settings to industrial applications is the low activity and selectivity under large-scale working conditions. Specifically, in most electrochemical systems at high current density, most electrons and protons are consumed by the HER reaction, rather than the reduction of nitrogen sources to NH_3. At the same time, the synthetic NH_3 reaction involves the interaction at a gas–liquid–solid three-phase interface. In a traditional single-cell or H-type reactor, the catalyst is also limited by the slow mass transfer of reactants, which ultimately leads to low FE and EE for the entire system. Conversely, at a very low current density, the reaction system can achieve ideal FE and other performance indicators, however, the NH_3 yield rate will be very low. Thus, at industrial current densities, there is currently no suitable electrochemical system that can achieve both high FE and high NH_3 yields.[20] Therefore, to achieve these goals, a major upgrade of the reactor design is required. The advanced electrocatalytic reaction systems that have been developed in recent years will be summarized in detail in the following chapters.

2.2.3 Measurements for ammonia synthesis. Long-term electrolysis for NH_3 synthesis usually uses two different operating modes, constant potential and constant current, which involve two kinds of electrolysis methods. Specifically, electrochemical measurements are usually performed in a traditional three-electrode system. The counter electrode (CE) and the working electrode (WE) together form a current circuit for the redox reaction to occur, and the reaction potential of the WE is regulated by the reference electrode (RE). In NH_3 synthesis, for example, the WE serves as the cathode to reduce the nitrogen sources in the electrolyte, while the CE serves as the anode and is involved in the oxidation reaction. In potentiostatic electrolysis, the input potential of the WE is kept constant relative to the RE, and the target products are then produced by the redox reaction. In an actual measurement, the measured potential is usually normalized to the standard hydrogen electrode (SHE), reversible hydrogen electrode (RHE), or normal hydrogen electrode (NHE). Ag/AgCl electrodes and saturated calomel electrodes with saturated KCl (E_0 = +0.197 V *vs.* SHE, and E_0 = +0.241 V *vs.* SHE, respectively) are commonly used as REs to control the operating potential of the WE. For specific test operations, an overpotential is required to initiate the electrochemical NH_3 synthesis reaction, which reflects the difference between the actual applied potential and the thermodynamic theoretical potential. A high overpotential indicates that a higher energy input and consumption are required to drive the reaction. Additionally, it is worth noting that when NH_3 synthesis is carried out at a high overpotential, the competitive HER takes place at the same time, resulting in a low FE for the system.[67]

In addition to the description of the electrochemical system above, specific performance measurements for the electrosynthesis of NH_3 usually involve linear sweep voltammetry (LSV), chronoamperometry (CA), cyclic voltammetry (CV), electrochemical impedance spectroscopy (EIS), multi-potential steps, and multi-current steps. LSV curves display the change in current density across a potential range for a given electrocatalytic process. By comparing the LSV curves measured in an Ar-saturated *versus* a N_2 saturated electrolyte, one can determine whether nitrogen reduction occurs at a certain potential range based on the difference in current density, in which this difference can be regarded as a contribution from the target reduction process. Regarding the CA technique, the current is monitored as a function of reaction time at a controlled potential. The obtained CA data can be used to calculate the FE of the electroreduction process and to evaluate the stability of catalysts under long-term electrolysis. The stability of the electrochemical reaction system can also be evaluated by comparing the LSV curves before and after repeated CV measurements. Besides this, a nearly constant conversion, selectivity, and FE for NH_3 can also illustrate that the electrocatalyst has good stability.[84] In addition, the CV technique can also be used to determine the double-layer capacitance for estimating the electrochemically active surface area of catalysts, which can be used to normalize the surface area of the electrode, thereby excluding the influence of surface roughness. EIS measurements can be used to evaluate the electrochemical reaction rate by analyzing the electrolyte resistance and charge-transfer resistance.[68]

2.3 Catalytic activity descriptors of ammonia synthesis

2.3.1 Faradaic efficiency. Since the NH_3 electrosynthesis reaction is usually accompanied by the competitive HER and the formation of by-products, it is vital to increase the selectivity for NH_3 in the catalytic system. Ideally, all the electricity supplied is used to generate NH_3. Thus, the ratio of the amount of charge used to synthesize NH_3 to the total amount of charge passed can be defined as the faradaic efficiency (FE). The FE directly indicates the influence of side reactions on NH_3 synthesis. Currently, NH_3 selectivity remains relatively low. It is worth noting that the NH_3 yield rate and FE often show a trade-off, usually resulting in a low FE at a high NH_3 yield or a high FE at a low NH_3 yield. According to the analysis of electrochemical measurements, the increase in the current density of the polarization curve is due to the production of reduction products. Therefore, the conversion rate of nitrogen sources, selectivity, and NH_3 FE at different potentials can be calculated, allowing the optimal reaction conditions for the highest electrochemical performance to be determined.

The conversion rate of the nitrogen source is calculated using the below formulas (11)–(13):[84]

$$\text{Conversion} = \Delta c_{\text{nitrogen source}}/c_0 \times 100\% \tag{11}$$

The selectivity for the NH_3 product is calculated using the formula below:

$$\text{Selectivity} = c/\Delta c_{\text{nitrogen source}} \times 100\% \tag{12}$$

The FE for NH_3 is calculated using the formula below:

$$\text{FE} = [(n \times 96\,485 \times c \times V)/(M \times Q)] \times 100\% \tag{13}$$

where c_0 is the initial concentration of the nitrogen source; $\Delta c_{\text{nitrogen source}}$ is the change in the concentration of the nitrogen source before and after electrolysis; c is the concentration of the produced NH_3; V is the volume of the electrolyte in the cathode compartment; n is the number of electrons transferred in the cathode reduction reaction; M is the molar mass of NH_3; and Q is the total amount of charge passed through the cathode during the reaction.

2.3.2 Ammonia yield. The large-scale production of NH_3, for example, from the gram to kilogram scale, is the primary and final goal of the green synthesis pathway. Therefore, objective and effective reporting of NH_3 production is essential to support further development in this field.[10] The yield rate of NH_3 is calculated using the formulas below ((14) and (15)):

$$\text{Yield} = (c \times V)/(t \times S) \tag{14}$$

$$\text{Yield} = (c \times V)/(t \times m) \tag{15}$$

where c and V are the same as in the formula for FE; t is the electrolysis time; S is the area of the WE; and m is the mass of the loaded catalyst.[84]

Based on the analysis above, the NH_3 yield rate is the amount of NH_3 produced per unit of time and per unit of catalyst mass (or electrode surface area), which reflects the reaction rate of NH_3 synthesis. It is also important that when using mg^{-1} as the standardized unit, some studies use the catalyst's total mass as the baseline, while others use the actual active sites for standardization. This can lead to unreliable comparisons of the NH_3 yield rate. Therefore, comparing performance using unified units is very important for progress in NH_3 synthesis.[10]

2.3.3 Energy efficiency. An electrolysis system's EE is a measure of how much energy is stored in the target products compared to the total amount of electricity input. It is well known that electricity accounts for a significant portion of NH_3 production costs.[115,116] From a techno-economic perspective, the EE must be increased as much as possible at commercially relevant current densities to reduce the total power input and improve economic efficiency. The EE is calculated using the formula below:[117]

$$\text{EE} = \text{Energy required}/\text{Energy input} = \Delta G^0 n/E_{\text{cell}}It \tag{16}$$

where ΔG^0 is the change in Gibbs free energy, n is the molar amount of the target product, I is the current, t is the running time, and E_{cell} is the full-cell voltage. A more specific transformation is shown in eqn (17) and (18):

$$\Delta G^0 n = zE^0 Fn = E^0 Q = E^0 It\text{FE} \quad (E^0 = E_{\text{anode}} - E_{\text{cathode}}) \tag{17}$$

$$E_{\text{cell}} = E_{\text{anode}} - E_{\text{cathode}} + \eta_{\text{cathode}} + \eta_{\text{anode}} + E_{\text{loss}} + \eta_{\text{mass transfer}} \tag{18}$$

where E^0 is the thermodynamic potential of the reaction; F is the Faraday constant; z is the number of electrons transferred in the cathode reduction reaction; Q is the amount of charge used in the cathode reduction reaction to produce NH_3; η_{cathode} and η_{anode} are the overpotentials of the redox reaction; $\eta_{\text{mass transfer}}$ represents the external overpotentials from mass transfer limitations; and E_{loss} is the ohmic dissipation, equal to the current multiplied by the resistance of the entire reaction system.

As seen in the formulas above, to achieve a high EE, the E_{cell} should be reduced, and the FE should be improved as much as possible. On the other hand, it is recognized that the oxygen evolution reaction has thermodynamic and kinetic difficulties, which consume a significant portion of the supplied electrical energy.[118,119] According to systematic analysis, the anode oxidation reaction, which produces low-value products, consumes more than 90% of the electrical energy, compared to less than 10% for the production of the target products at the cathode.[120] Therefore, optimizing the anode reaction in the NH_3 synthesis system can further reduce energy consumption and improve the system's economic efficiency.

2.3.4 Stability. Stability is a key indicator for evaluating the practical value of a green NH_3 synthesis pathway. In other words, even if a catalyst's initial NH_3 synthesis activity is excellent, its decomposition or inactivation during operation prevents its further use in industrial production. At low current densities, the NH_3 synthesis reaction has high selectivity and FE, meaning that almost all the input energy is used for NH_3 synthesis, and the competing HER is slow. However, at industrial current densities (>500 mA cm^{-2}), the competitive HER dominates the synthesis system. Therefore, highly active and stable catalysts must maintain their original yield rate, FE, and EE, or fluctuate only slightly, after repeated use for tens or even hundreds of hours to meet industrial standards.[10] Currently, stability tests check whether the yield rate, conversion, FE, and other indicators are maintained after long-term potentiostatic and galvanostatic electrolysis. At the same time, the structural stability of the catalyst is characterized by *in situ* spectroelectrochemical techniques and post-reaction electron microscopy, which can effectively confirm the system's stability.

3. Photochemical synthesis of ammonia

Inspired by how plant nitrogenases convert N_2 into NH_3 using solar energy, efficiently using renewable energy and converting it into chemical energy is crucial for protecting the environment and conserving energy. In this section, we first analyze the mechanism of photocatalytic NH_3 synthesis. Specifically, the photoreduction process includes two steps: (a) photoexcited electrons transfer from the valence band to the conduction band, leaving photogenerated holes in their original positions; (b) free photogenerated electrons and holes migrate to the photocatalyst surface to participate in redox reactions, while some electrons and holes recombine. Photocatalytic NH_3 synthesis is a six-electron, six-proton process that includes N_2 adsorption, activation, and cleavage of the $N{\equiv}N$ bond, combined with a hydrogenation process, and the production and desorption of NH_3.[31] However, most reported photocatalysts face key problems, such as severe photogenerated charge recombination, weak N_2 adsorption, difficult $N{\equiv}N$ bond dissociation, the poor proton affinity of the N_2 molecule preventing electron transport and Lewis acid–base reactions, and the difficult N_2 reaction caused by its large 10.82 eV energy gap,[121] all of which result in low photocatalytic NH_3 synthesis efficiency. Therefore, the rational design and preparation of efficient photocatalysts for N_2 reduction still present great challenges. We will first describe the photo-response of photocatalysts and the evaluation criteria for photocatalytic performance and then summarize engineering strategies for improving photocatalytic performance. Then, specific examples for each type of photocatalyst will be discussed in terms of catalyst design strategies, performance, and structure–activity relationship (Table 1).

The evaluation criteria for photocatalytic ammonia synthesis catalysts include two main aspects: (1) the evaluation of photoresponse includes (a) light absorption ability, determined by the absorption edge position, absorption intensity, and bandgap width to assess the visible-light response; (b) charge carrier separation efficiency, measured through photocurrent density and photoluminescence spectroscopy to determine charge separation effectiveness, with transient fluorescence lifetime tests further revealing carrier lifetime and migration ability; and (c) band structure alignment, where the valence and conduction band positions of the photocatalyst must match the required redox potentials to ensure the reaction proceeds efficiently. (2) The evaluation of photocatalytic activity involves key parameters including ammonia production rate, stability, turnover frequency, and quantum efficiency. The ammonia production rate, measured as the product yield per unit of time per unit of catalyst mass or area, is a metric used to compare different photocatalysts, with better performers showing higher yields. Stability is demonstrated by comparing ammonia production rates after multiple cycling tests or prolonged illumination. Faradaic efficiency, calculated as the ratio of electrons used for ammonia synthesis to the total electrons consumed, reflects the catalyst's selectivity for the target product, where high values indicate effective suppression of the competing hydrogen evolution reaction and preferential use of electrons for ammonia production. Turnover frequency measures the number of ammonia molecules produced per active site per unit of time and serves as an indicator of intrinsic catalytic activity. Quantum efficiency directly measures the proportion of incident

Table 1 Summary of the previously reported state-of-the-art catalysts for the efficient photocatalytic NH_3 synthesis

Catalysts	Nitrogen source	Experimental conditions	Yield rate	Reactor	Ref.
Al-PMOF(Fe)	N_2	Visible light, $\lambda > 420$ nm, 100 mW cm^{-2}	127 μg h^{-1} g^{-1} cat.	A custom-designed quartz reactor with magnetic stirring	122
FeS_2@V_N-CN	N_2	A doped Hg immersion lamp, 350 W	800 μg h^{-1}	A water-cooled quartz-glass inlay	123
MIL-100(Fe)-200W	N_2	300 W xenon lamp with a 420 nm cutoff filter, simulate visible light, 420–800 nm, 130 mW cm^{-2}	115.1 μmol g^{-1} h^{-1}	A reactor equipped with a circulating water outer jacket to maintain a temperature of 25 °C	124
ZnCr-LDH nanosheets	N_2	Simulated solar light irradiation, 300 W xenon lamp as the excitation source, 200–800 nm, 5.0 W cm^{-2}	33.19 μmol g^{-1} h^{-1}	A quartz reactor equipped with a circulating water outer jacket to maintain a constant temperature of 25 °C	125
P–Fe/$W_{18}O_{49}$	N_2	A xenon lamp used as a simulated solar light source, 100 mW cm^{-2}	187.6 μmol g^{-1} h^{-1}	A self-made mobile phase reaction cell with a circulating thermostatic water bath to maintain a constant temperature of 25 °C	126
Ru/RuO_2/C-TiO_x	N_2	300 W xenon lamp equipped with a 395 nm or 420 nm cut-off filter	109.3 μmol g^{-1} h^{-1}	A quartz reactor maintained below 25 °C	127
Ru-$K_2Ta_2O_{6-x}$	N_2	UV irradiation or visible light irradiation (>400 nm) from a 300 W xenon lamp equipped with cut-off filters	335 μg g^{-1} h^{-1}	An airtight quartz reactor with a vacuum environment	128
Au@UiO-66	N_2	Visible light (>400 nm, 100 mW cm^{-2})	18.9 mmol gAu^{-1} h^{-1}	A homemade outer irradiation-type gas-flow cell	129
GDY@Fe–B	N_2	Visible light irradiation ($\lambda \geqslant 400$ nm), using a 300 W xenon lamp	1762.35 ± 153.71 μmol h^{-1} $g_{cat.}{}^{-1}$	A gas recycling set-up	130
CuCr-LDH	N_2	Visible light irradiation ($\lambda \geqslant 400$ nm), using a 300 W xenon lamp	184.8 μmol L^{-1}	A quartz reactor maintained below 25 °C	131
FePc-POF	N_2	A 300 W xenon lamp equipped with a 400 nm cutoff filter, 200 mW cm^{-2}	1820.7 μmol g^{-1} h^{-1}	A solvent-in-gas reactor	132
TiO_2-B-2	N_2	A 300 W xenon lamp, $\lambda > 300$ nm	3.35 mg h^{-1} g^{-1}	A self-made quartz reactor	139
WO_3/CdS	N_2	A 300 W xenon lamp	35.8 μmol h^{-1} g^{-1}	A gas–solid reaction system	140
BCN	N_2	Light irradiation (with a cut-off filter, $\lambda > 400$ nm, a light intensity of 0.5 W cm^{-2}, 250 W Xe lamp)	313.9 μmol g^{-1} h^{-1}	A CEL-HPR100S + photocatalytic reactor	141
LiH	N_2	A xenon lamp with the UV cut-off filter (300–420 nm), 136.5 mW cm^{-2}	518 μmol g^{-1} h^{-1}	A quartz tube as a fixed-bed reactor	142
BaO_{NCs}-TNS	$NO_3{}^{-}$	300 W xenon lamp	89.79 mmol $g_{cat.}{}^{-1}$ h^{-1}	An MC-GF250 photocatalytic reactor	143

photons converted into electrons that participate in ammonia synthesis, effectively representing the catalyst's ability to harvest light and separate charges. When combined with turnover frequency, quantum efficiency helps evaluate catalytic performance issues. For instance, high light absorption and charge separation efficiencies coupled with a low quantum efficiency may suggest slow surface N_2 activation or proton transfer, requiring an evaluation of the intrinsic activity through turnover frequency analysis. Furthermore, the correlation between quantum efficiency and faradaic efficiency reveals how electrons are used. A high quantum efficiency with a low faradaic efficiency indicates that the hydrogen evolution side reaction is dominant, while high values for both parameters show the preferential use of electrons for ammonia synthesis.

To create efficient photocatalytic materials, inspired by the biological molecule chlorophyll, which has a favorable binding site for the N_2 atom, a porphyrin-based metal–organic framework (PMOF) was developed that contains atomically dispersed Al and Fe metal centers to promote the adsorption and activation of N_2 (Fig. 2(a) and (b)) (Al-PMOF(Fe)).[122] Al-PMOF(Fe) showed a remarkable production rate of 127 μg h^{-1} $g_{cat.}{}^{-1}$ (Fig. 2(c)), outperforming the Al-PMOF, which had a rate of 84.5 μg h^{-1} $g_{cat.}{}^{-1}$. The porphyrin ligand efficiently harvested light, and the active Fe–N sites lowered the difficulty of the rate-determining step, N_2 activation, thus improving the photocatalytic activity. Furthermore, inspired by the high optical absorption and high charge carrier mobility of biological enzymes, carbon nitride (CN) heterogeneous materials containing N defects and loaded with FeS_2 were created by high-temperature calcination and alkali treatment (Fig. 2(d)). Using the favorable light absorption and N_2 activation properties of the Fe–S system, as well as the high activity of the prepared CN (Fig. 2(e)), an NH_3 yield of up to 800 μg L^{-1} was obtained, which was about 400% higher than that of pristine CN.[123] FeS_2 acted like a cocatalyst, increasing the NH_3 yield through π-back-donation from Fe centers to the imine nitrogen of the defect-rich CN, thereby activating the structure and increasing NH_3 generation from cyano groups (Fig. 2(f)).

To address the key problems of adsorbing and activating inert N_2 molecules in photocatalytic NH_3 synthesis, a trinuclear Fe–O cluster-based MOF (MIL-100(Fe)) catalyst with dual defects was synthesized using a non-thermal plasma-assisted strategy (Fig. 3(a)).[124] By regulating the Fe–O coordination number with plasma power, the terminal ligand defects in the MIL-100(Fe)-200W catalyst were 7.7 times higher than that in the pristine catalyst under visible light irradiation (Fig. 3(b)). By accurately controlling the types and amounts of defects in MIL-100(Fe), the NH_3 yield rate was remarkably increased. This was due to the formation of abundant exposed, coordinatively unsaturated Fe sites, which injected more d-electrons into the

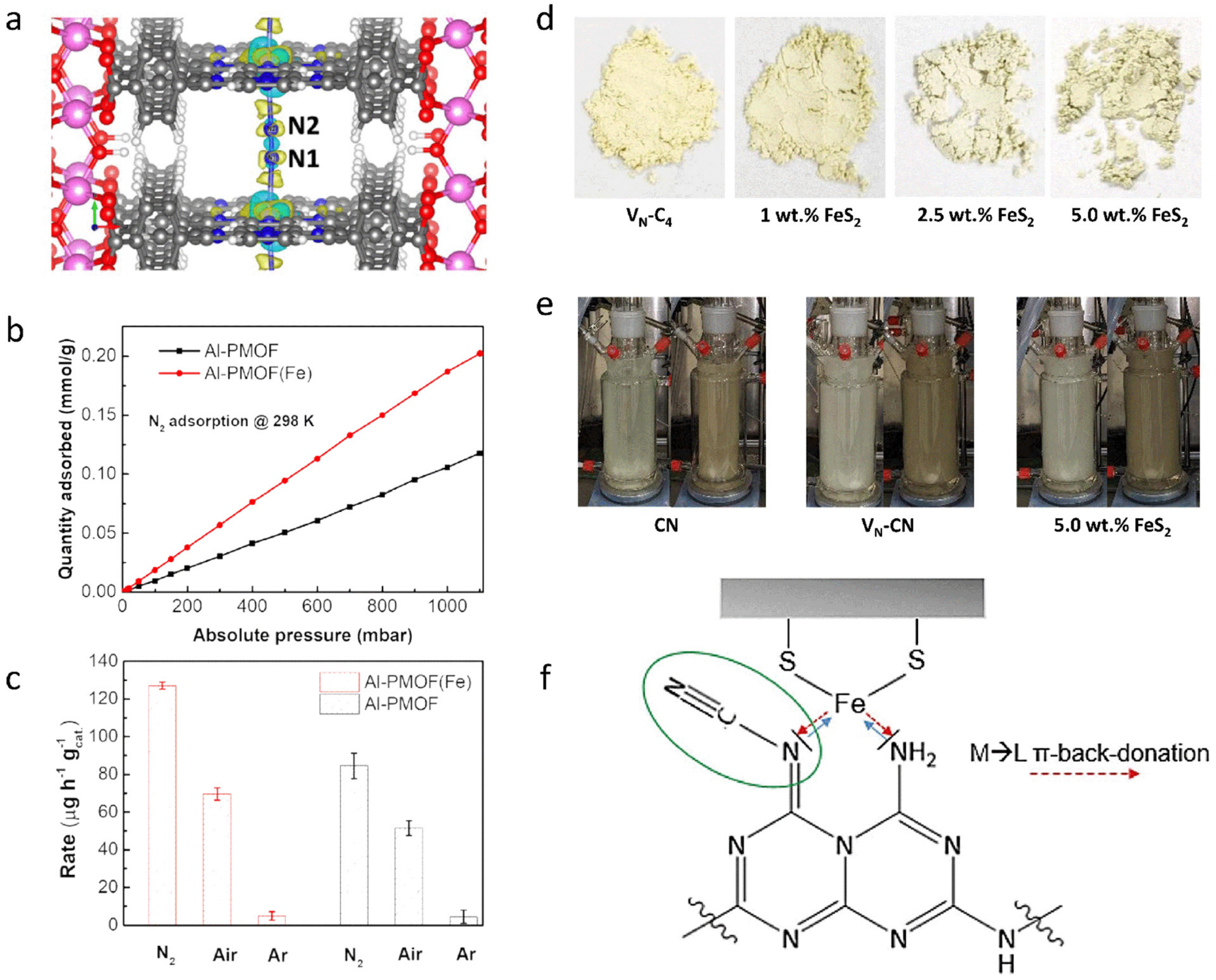

Fig. 2 (a) Adsorption model of the N_2 molecule for Al-PMOF(Fe). (b) N_2 gas adsorption isotherms for Al-PMOF and Al-PMOF(Fe) at 298 K. (c) NH_3 yield rates for Al-PMOF and Al-PMOF(Fe). (d) Photographs of V_N–C_4 and V_N–C_4 containing different amounts of FeS_2. (e) Photocatalyst process over different catalysts. (f) Activity enhancement mechanism diagram of the Fe–S system. Reproduced with permission from ref. 122 Copyright 2021, American Chemical Society. Ref. 123 Copyright 2022, Wiley-VCH.

N_2 molecules to produce the key intermediate *NNH, thereby decreasing the energy barrier of the RDS and efficiently activating N_2 (Fig. 3(c)). These methods could also be applied to common inorganic semiconductor photoelectrodes, improving their NH_3 synthesis performance by an order of magnitude or more through the rational manipulation of defect concentrations. Along these lines, ZnCr-Layered double hydroxide (LDH) nanosheets were produced by a simple coprecipitation method combined with an alkali etching strategy (Fig. 3(d)).[125] The etched nanosheets displayed a higher performance for the photofixation of N_2 to NH_3 compared to the pristine nanosheets. The etched ZnCr-LDH nanosheets achieved an NH_3 yield rate of 33.19 μmol g^{-1} h^{-1}, which was 10 times higher than that of the pristine ZnCr-LDH nanosheets. The alkali method created a high concentration of oxygen vacancies and low-coordination metal centers, in which the unsaturated active sites promoted the adsorption and activation of N_2, thus lowering the reaction energy barrier to NH_3 and significantly increasing photocatalytic activity. In addition to introducing defect sites, heteroatom doping has similar effects. For example, Fe-doped $W_{18}O_{49}$ nanowires (Fe/$W_{18}O_{49}$) were obtained by an agent-modified solvothermal method and then mixed with black phosphorus quantum dots in an aqueous solution under vigorous stirring to form the final product, P–Fe/$W_{18}O_{49}$. The as-prepared P–Fe/$W_{18}O_{49}$ significantly promoted photocatalytic activity for fixing N_2 into NH_3. Specifically, an NH_3 yield rate of up to 187.6 μmol g^{-1} h^{-1} was achieved, nearly an order of magnitude higher than that of the pristine $W_{18}O_{49}$ (18.9 μmol g^{-1} h^{-1}).[126] The increased photocatalytic N_2 fixation activities were mainly attributed to the bulk Fe-doping, which elevated the conduction band position and the d-band center, thereby increasing the N_2 reduction ability and suppressing charge recombination (Fig. 3(e) and (f)). Moreover, the anchored black phosphorus quantum dots could remarkably increase surface N_2 adsorption and the cleavage of the N$\equiv$N bond through the W–P dimer adsorption mode.

Following the innovative ideas above, it was found that immobilizing or doping with precious metals can also address the high activation energy barrier and difficult adsorption of

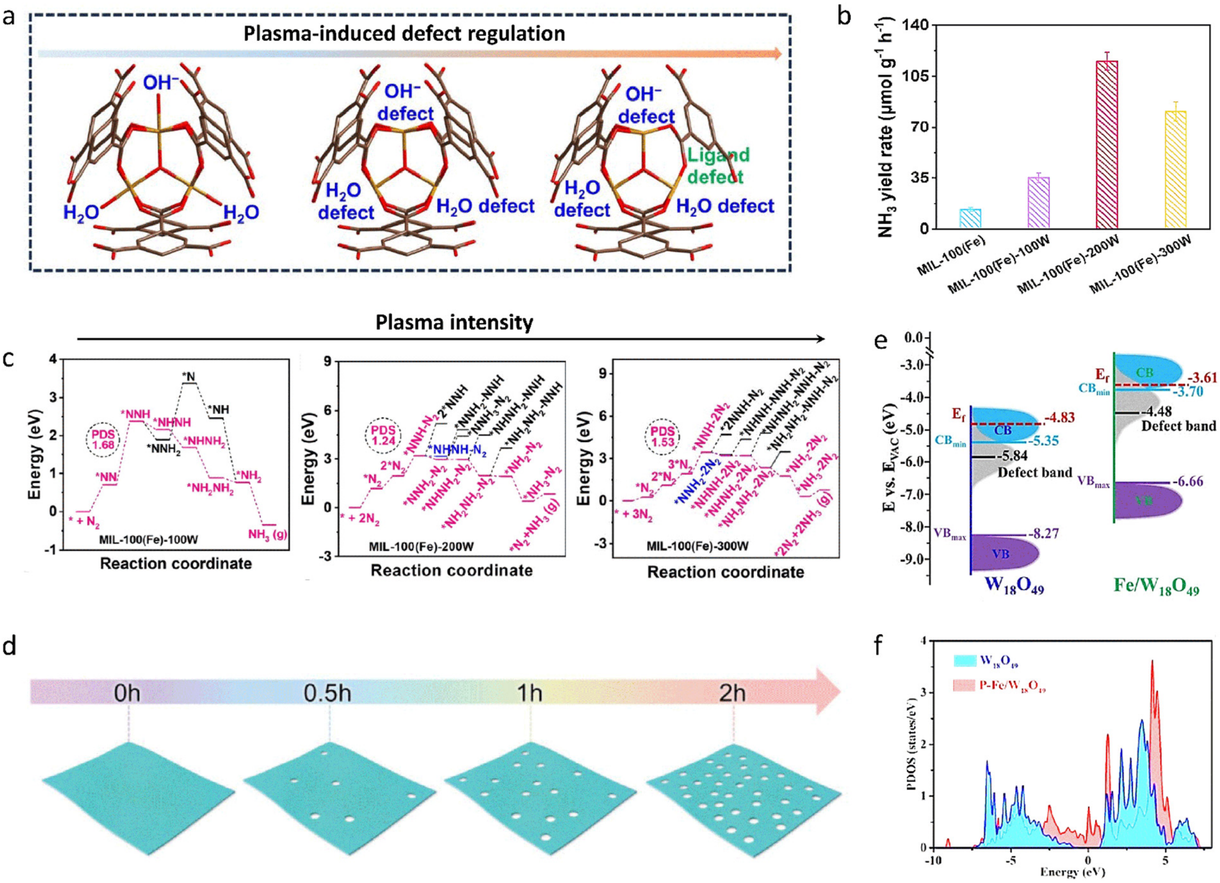

Fig. 3 (a) Scheme of the plasma-assisted synthesis of MIL-100(Fe) with defects. (b) Photocatalytic NH_3 yield rate for different catalysts. (c) Free energy diagrams of MIL-100(Fe) synthesized at different plasma intensities. (d) Scheme of the etching synthesis of ZnCr-LDH nanosheets at different alkali-treatment times. (e) The band structures of $W_{18}O_{49}$ and Fe/$W_{18}O_{49}$ samples. (f) The projected density of state diagram of $W_{18}O_{49}$ and P–Fe/$W_{18}O_{49}$ samples. Reproduced with permission from ref. 124 Copyright 2024, Wiley-VCH. Ref. 125 Copyright 2020, Wiley-VCH. Ref. 126 Copyright 2022, Wiley-VCH.

the N_2 reactant. C-doped anatase titanium oxide (C-TiO_x) nanosheets with a high concentration of Ti^{3+} species were fabricated using an H_2O_2-assisted thermal-oxidation etching (H_2O_2-TOE) strategy. The prepared C-TiO_x nanosheets were further combined with Ru/RuO_2 (Ru/RuO_2/C-TiO_x) and subsequently used as a photocatalyst for NH_3 synthesis. A remarkable NH_3 yield rate of 109.3 μmol g^{-1} h^{-1} was achieved.[127] Benefiting from the high concentration of Ti^{3+} and the large surface area of the synthesized C-TiO_x, the material could significantly chemisorb and activate N_2 molecules and provide plenty of multi-electron transfer channels (Fig. 4(a)). Moreover, coupling this with a strong synergistic effect that simultaneously enhanced charge separation and transfer after introducing Ru species further boosted the photocatalytic performance of NH_3 synthesis. Following this line of research, a variety of perovskite- and pyrochlore-structured tantalates with immobilized Ru species were prepared (Ru–$K_2Ta_2O_{6-x}$) (Fig. 4(b)), followed by processing with a high-temperature solid-state reduction to introduce abundant oxygen vacancies and low-valent Ta. The resulting pyrochlore tantalates exhibited a higher conduction band energy level with a stronger reducing ability of excited electrons (Fig. 4(c)).[128] The constructed catalyst, with its interface Schottky barrier, enhanced the adsorption of N_2 molecules and the efficiency of photo-induced electron transfer from the photocatalyst to the N_2 molecules (Fig. 4(d)). Compared with perovskite-type $KTaO_{3-x}$, the NH_3 yield rate of Ru–$K_2Ta_2O_{6-x}$ showed a 3.7-fold increase (335 μg $g^{-1}h^{-1}$). The Schottky barrier and spontaneous electron transfer between $K_2Ta_2O_{6-x}$ and Ru species improved photoexcited charge separation and accumulated energetic electrons to facilitate N_2 activation (Fig. 4(e)), ultimately boosting the photocatalytic activity of NH_3 synthesis. From the study above, the interaction between the active sites and the carrier materials is crucial for enhancing the activity of NH_3 synthesis. Therefore, the development of novel carrier materials is expected to further modify the behavior of reactants. MOFs can serve as multifunctional substrates, not only to anchor active species with high dispersion but also to provide interconnected nanoreactors with ultrahigh surface areas for the diffusion and collision of N_2 molecules towards the active sites. In this context, Au nanoparticles (AuNPs) were immobilized within UiO-66 particles by impregnation and reduction to create a gas-membrane-solution reaction interface (Fig. 4(f) and (g)). Gaseous N_2 molecules could directly enter the porous Au@UiO-66 membrane, effectively increasing the availability of N_2 near the AuNPs, resulting in an NH_3 yield rate of 18.9 mmol g_{Au}^{-1} h^{-1} under visible light.[129]

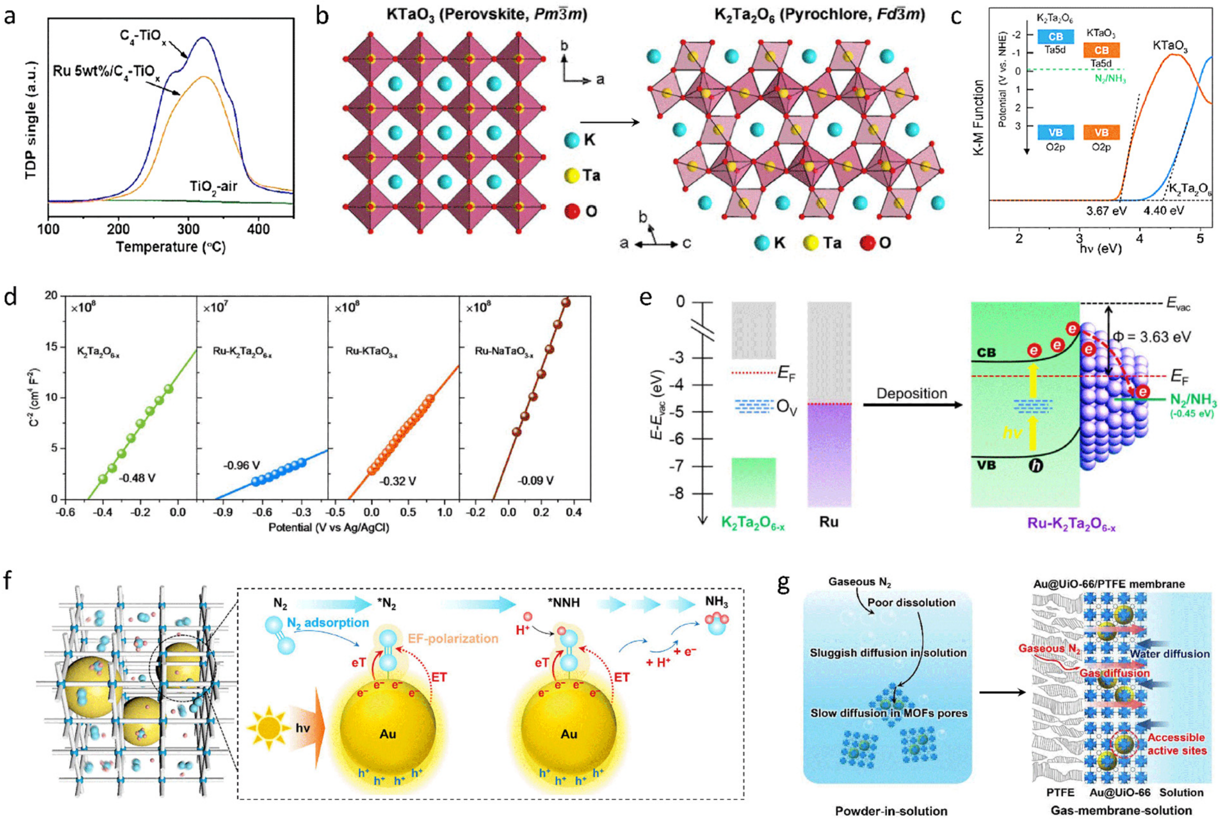

Fig. 4 (a) Temperature-programmed desorption of N_2 for different catalysts. (b) Crystal structure images of perovskite $KTaO_3$ and pyrochlore $K_2Ta_2O_6$. (c) Band gap of $KTaO_3$ and $K_2Ta_2O_6$ calculated from the Kubelka–Munk function *versus* photon energy. (d) Mott–Schottky plots of different catalysts. (e) The mechanism diagram of photocatalytic performance improvement for $Ru-K_2Ta_2O_{6-x}$. (f) The nanostructure and photocatalytic N_2 reduction step diagram of Au@UiO-66. (g) The diagram of a traditional homogeneous powder-in-solution system and a gas–membrane–solution reaction system. Reproduced with permission from ref. 127 Copyright 2021, Wiley-VCH. Ref. 128 Copyright 2023, Wiley-VCH. Ref. 129 Copyright 2021, American Chemical Society.

The multifunctional AuNPs functioned as a photosensitizer, cocatalyst, and plasma accelerator to generate hot electrons, accelerating the conversion process from N_2 to NH_3 and reducing the activation energy barrier, ultimately enhancing the photocatalytic activity.

Inspired by the uneven surface charge distribution, large network plane, and large cavity structure of graphdiyne (GDY), a highly active GDY heterojunction photocatalyst (GDY@Fe–B) was produced through a modified Glaser–Hay coupling reaction combined with co-precipitation.[130] The prepared GDY@Fe–B catalyst showed remarkable performance for photocatalytic NH_3 synthesis, with a very high NH_3 yield of 1762.35 ± 153.71 μmol h^{-1} $g_{cat.}^{-1}$ and 100% selectivity. Adding GDY effectively changed the coordination environment and valence state of the Fe atoms. This atomic-level change in the metal atoms' immediate environment adjusted the reaction mode and improved the photocatalytic activity. This strategy took full advantage of the structure and properties of GDY and showed that the new aggregate structure could control the form, coordination environment, and valence state of the Fe oxide, opening a new direction for the atomic-scale modification of photocatalysts. To further promote the chemisorption and activation of N_2 at normal temperature and pressure, an $M^{II}M^{III}$-LDH (M^{II} = Mg, Zn, Ni, Cu; M^{III} = Al, Cr) nanosheet photocatalyst was produced by a simple coprecipitation method (Fig. 5(a)).[131] Among these, the CuCr-LDH photocatalyst had a significant NH_3 yield rate of 184.8 μmol L^{-1} under UV-vis illumination. The introduction of oxygen-rich defects and Cu(II) ions resulted in a clear structural distortion, which increased the adsorption and activation of N_2 molecules and accelerated the transport of electrons generated by visible light from the photoelectrode to N_2 (Fig. 5(b) and (c)), thus promoting the NH_3 synthesis.

Additionally, it is well known that the low thermodynamic energy barrier of the competing HER and the very low solubility of N_2 gas also led to inefficient NH_3 synthesis in a solvent-heavy environment. Therefore, optimizing the conventional gas-in-solvent system is also expected to solve this fundamental reaction problem. For this reason, constructing a solvent-in-gas system, combined with porous organic framework materials, offers a great opportunity for NH_3 production (Fig. 5(d) and (e)). Based on this, MPc-POF (M = Fe, Co, Zn) photocatalysts were prepared by the Schiff base reaction of tetraamino-metal-phthalocyanine with terephthalaldehyde under solvothermal conditions.[132] The prepared catalyst, combined with a solvent-in-gas system, showed a continuous, ultra-high NH_3 generation rate of 1820.7 μmol g^{-1} h^{-1}, which is more than eight times higher than the conventional gas-in-solvent system (226.2 μmol g^{-1} h^{-1}) (Fig. 5(f)). In the solvent-in-gas system, the MPc-POF operated directly in an N_2 environment. This not only accumulated a high concentration of N_2 in the framework (Fig. 5(g)) but also limited the contact between the solvent and the photocatalyst, efficiently inhibiting the competitive HER process and increasing the efficiency of photocatalytic NH_3 synthesis.

In addition to optimizing the behavior of N_2 molecules, the problem of photogenerated charge recombination, which leads to low NH_3 synthesis efficiency, has also recently been addressed. TiO_2 has been widely used in the photocatalytic synthesis of NH_3.[133–135] Until now, TiO_2-based photocatalysts have been limited by their wide bandgap (3.2 eV for anatase and 3.0 eV for rutile) and high electron–hole recombination rate.[136] Therefore, defects and nonmetal doping have been widely used to narrow the bandgap and shift its optical response to the visible light region.[137,138] Following this idea, an anatase TiO_2 (101) catalyst modified by boron doping was synthesized through a calcination method.[139] The prepared B-doped TiO_2 nanosheet achieved an NH_3 yield rate of 3.35 mg h^{-1} g^{-1} under simulated sunlight irradiation, which was 1.74 times higher than that of pure TiO_2. B-doping remarkably improved the photocurrent response, generating more electrons and accelerating the separation and transfer of photogenerated electron–hole pairs, which increased the photocatalytic NH_3 synthesis performance. In addition, creating photocatalytic materials with heterogeneous interfaces is also expected to optimize the behavior of photogenerated charges and carriers. For instance, reduced CdS nanoparticles were grown in place on an oxidized WO_3 surface through a hydrothermal method to produce a redox heterojunction catalyst. In this heterojunction, interfacial charge redistribution can effectively promote the selective accumulation of photogenerated electrons and holes in the CdS and WO_3 components.[140] Thus, N_2 molecules could be activated and reduced to NH_3 through a multi-electron process

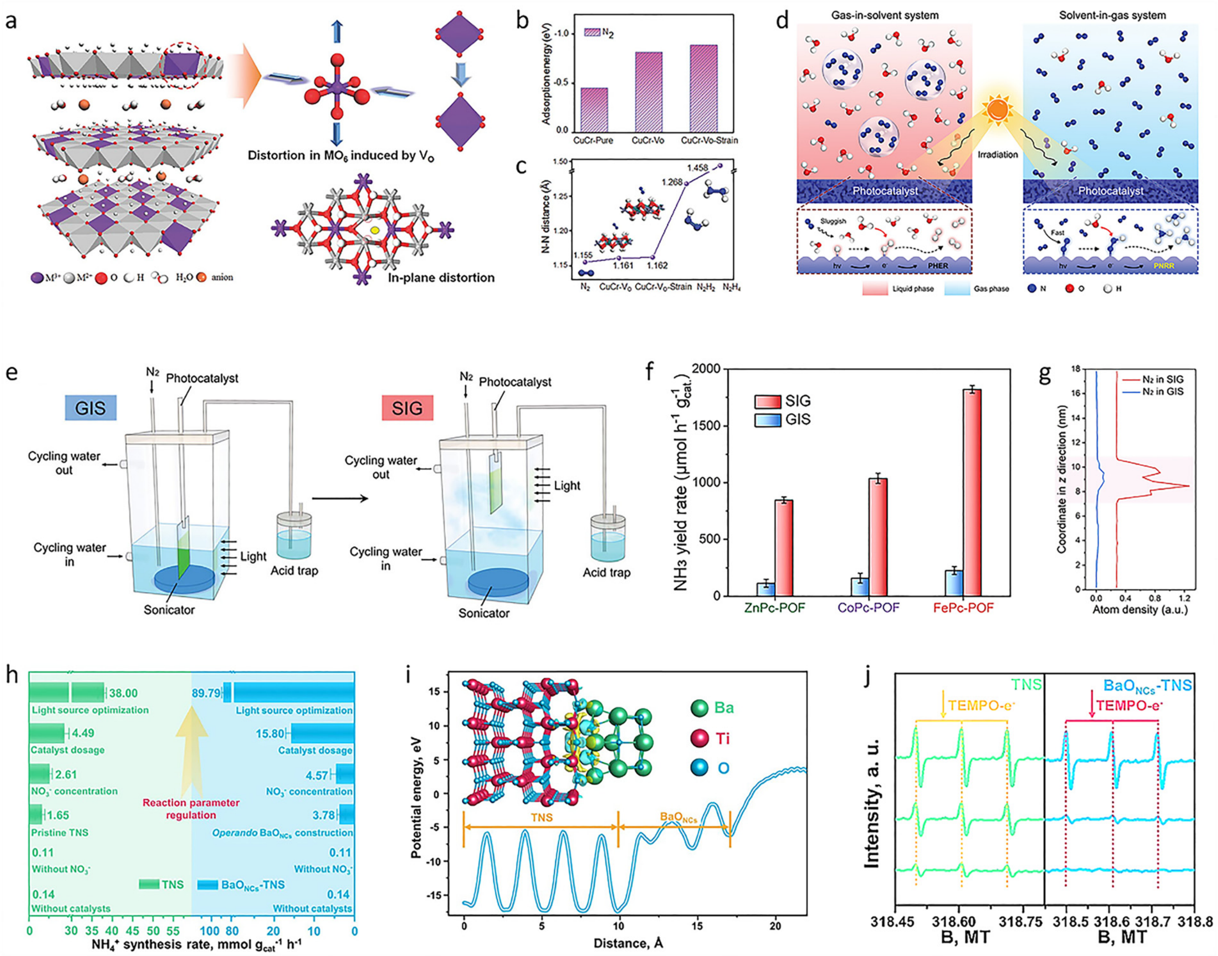

Fig. 5 (a) Structure scheme of $M^{II}M^{III}$-LDH nanosheets. (b) Adsorption energies of N_2 on different samples. (c) N–N distance of different samples and N_2, N_2H_2, and N_2H_4 molecules. (d) Schematic illustration of a gas-in-solvent system and a solvent-in-gas system mechanism. (e) Reaction devices of a gas-in-solvent system and a solvent-in-gas system. (f) NH_3 yield rate of different catalysts in a gas-in-solvent system and a solvent-in-gas system. (g) Distribution of N_2 in a gas-in-solvent system and a solvent-in-gas system along the change of the z direction. (h) Photosynthesis NH_4^+ performance of TNS and BaO_{NCs}–TNS. (i) Charge difference distribution at the BaO_{NCs}–TNS interface for illustrating the charge transfer. (j) Electron paramagnetic resonance spectra of TNS and BaO_{NCs}–TNS. Reproduced with permission from ref. 131 Copyright 2017, Wiley-VCH. Ref. 132 Copyright 2023, Wiley-VCH. Ref. 143 Copyright 2022, Springer Nature.

with a yield of 35.8 μmol h^{-1} g^{-1}. Due to the tight interface and the built-in electric field created between the heterojunction components, the resulting internal electric field and Coulomb force could provide the driving force to induce the separation and migration of photogenerated carriers. Therefore, strongly reducing photoelectrons and strongly oxidizing photogenerated holes accumulated in the CdS and WO_3 components, respectively, which overcame the thermodynamic barrier for converting N_2 into NH_3. To minimize the recombination of photogenerated carriers, a B-atom-doped g-C_3N_4 nanosheet (BCN) was prepared by a simple heat treatment method.[141] The NH_3 yield rate of the prepared BCN reached 313.9 μmol g^{-1} h^{-1}, which was about 10 times that of pure g-C_3N_4. The created B–N–C bonds could not only stably anchor the exposed active N atoms on the surface of g-C_3N_4 but also effectively inhibit photogenerated carrier recombination by forming p–n junctions at the nanoscale. Meanwhile, the B atom also served as an active site for the adsorption and activation of N_2 molecules. Photon-driven chemical processes are usually mediated by metal oxides, nitrides, and sulfides, but their light conversion efficiency is limited by carrier recombination. Therefore, early work has mainly focused on optimizing photogenerated carrier recombination.

Recently, a lithium hydride (LiH) catalyst has been developed for the photochemical synthesis of NH_3. The photolysis of LiH is fundamentally different from the behavior of common oxide and nitride semiconductors. The photolysis of LiH under ultraviolet irradiation can produce long-lived, photon-produced electrons that reside in hydrogen vacancies, called F-centers. The generation of light-driven F-centers can provide an alternative method for carrier separation to support chemical transformations that are kinetically or thermodynamically challenging.[142] Specifically, the LiH catalyst is easily photolyzed into H_2 under ultraviolet irradiation, and the photolysis of LiH can produce localized 'active' electrons, forming an electron-rich state on the surface, which provides a favorable environment for the reduction of N_2. Photoactivated LiH could split $N\equiv N$ bonds to form N–H bonds under mild conditions. The yield rate was 518 μmol g^{-1} h^{-1}. This work shows the development potential of hydride semiconductors in the photo-fixation N_2 reaction, expanding the understanding of 'hydride N_2 fixation chemistry' and providing ideas for developing a new generation of light-driven NH_3 synthesis technology.

As an alternative feedstock, NO_3^-, with its high solubility and proton affinity, can be easily dissociated for sustainable NH_3 production. Therefore, a general strategy was developed to construct subnanometric alkaline-earth oxide clusters (MO_{NCs}, where M = Mg, Ca, Sr, or Ba) anchored on TiO_2 nanosheets (TNS) during the reaction. After the construction of BaO_{NCs}-TNS, a high NH_4^+ photosynthesis rate of 89.79 mmol $g_{cat.}^{-1}$ h^{-1} was reached with nearly 100% selectivity (Fig. 5(h)). A total NH_4^+ yield of 0.78 mmol was achieved within 72 hours.[143] The local interfacial structure was precisely tailored to strengthen charge transfer at the BaONCs/TNS interface (Fig. 5(i)). It was then revealed that the eight-electron transfer reaction for NO_3^- reduction was notably accelerated, achieving a high rate for sustainable NH_4^+ photosynthesis (Fig. 5(j)). To further achieve high-selectivity NO_3^- reduction for NH_3 synthesis, it is necessary to improve the overall photocatalytic efficiency, because both oxidation and reduction reactions together determine the redox efficiency. Under light irradiation, the catalyst produces an equal number of electrons (e^-) and holes (h^+) at the same time and carries out a reduction half-reaction and an oxidation half-reaction, respectively. However, most studies only focus on one half of the reactions. The precise regulation of the oxidation reaction can be used as an effective strategy to directly adjust the efficiency and selectivity of the reduction reaction for NH_3 synthesis. In this regard, a redox system was formed by combining NO_3^- reduction with ethylene glycol oxidation. Specifically, Cu–O–Ti clusters anchored on TiO_2 nanosheets (CuO_x@TNS) were designed to regulate the selective reduction of NO_3^-. The NH_3 photosynthesis rate of CuO_x@TNS was 16.04 ± 0.40 mmol $g_{cat.}^{-1}$ h^{-1}, and the selectivity for NH_3 was close to 100%.[144] The molecular mechanism of the synergistic reaction between NO_3^- reduction and ethylene glycol oxidation showed that introducing ethylene glycol oxidation could effectively promote the consumption of h+ and generate alkoxy radicals ($^{\bullet}R$). At the active site of the Cu–O–Ti clusters, photogenerated h^+ preferentially oxidized ethylene glycol to produce $^{\bullet}R$, which efficiently inhibited the formation of strongly oxidizing hydroxyl radicals. Meanwhile, the construction of Cu–O–Ti clusters increased the production of e^-, thus promoting NH_3 synthesis efficiency. The overall photocatalytic redox efficiency was improved by matching the oxidation half-reactions and constructing high-performance catalytic sites, and the directed regulation of the reduction half-reactions at the active sites was realized, leading to efficient and highly selective photocatalytic NO_3^- reduction.

4. Electrochemical synthesis of ammonia

4.1 Nitrogen source with a zero oxidation state, N_2

The traditional H–B approach for NH_3 synthesis involves reacting high-purity N_2 and H_2 under harsh, high-temperature and high-pressure conditions,[145] resulting in low efficiency, significant energy consumption, and large greenhouse gas emissions. The chemical inertness of N_2 makes the reduction of N_2 at room temperature and atmospheric pressure a great challenge.[28] Fortunately, the electrochemical reduction of N_2 offers a sustainable method to overcome this bottleneck.[146–148] In this section, the types of catalytic materials and the performance of electrocatalytic NH_3 synthesis are summarized in Table 2. Specifically, a single-atom dispersed Fe_{SA}–N–C catalyst was prepared by carbonizing a polypyrrole–Fe coordination compound at 600 °C. The single-atom Fe catalyst enabled the electroreduction of N_2 to NH_3 with a superior FE of 56.55% and a large yield rate of 7.48 μg h^{-1} mg^{-1} at 0 V *vs.* RHE, far surpassing the metal-free N–C catalyst (a FE of 9.34% and a yield rate of 4.75 μg h^{-1} mg^{-1}). The Fe active sites could lower the free energy barrier for $^*N_2$ adsorption and suppress H_2 production. The central Fe sites also decreased the energy barrier of the rate-determining step, $^*H_2O–N_2 + H^+ + e^- \rightarrow {}^*H_2O–NNH$, in which protons and electrons tend to attack the $^*N_2$ to facilitate hydrogenation, thus boosting the

Table 2 Summary of the previously reported state-of-the-art catalysts for the efficient electrocatalytic NH_3 synthesis

Catalysts	Nitrogen sources	Faraday efficiency (%)	Yield rate	Ref.
Fe_{SA}–N–C	N_2	56.55	7.48 μg h^{-1} mg^{-1}	149
Cu/PI-300	N_2	6.56	3.44 μg h^{-1} mg^{-1}	150
1T″ MoS_2	N_2	13.6	9.09 μg h^{-1} mg^{-1}	151
B_4C	N_2	15.95	26.57 μg h^{-1} mg^{-1}	152
Ru-LCN	NO	65.96	765.34 μg h^{-1} mg^{-1}	172
RuGa	NO	72.3	5450.2 μg h^{-1} mg^{-1}	178
*Cu foam	NO	93.5	8790.7 μg h^{-1} cm^{-2}	78
*Cu electrode	NO	90	30 702 μg h^{-1} cm^{-2}	167
CoS_{1-x}	NO	53.62	1492.41 μg h^{-1} mg^{-1}	180
MoS_2/GF	NO	76.6	411.8 μg h^{-1} mg^{-1}	55
Co_1/MoS_2	NO	87.7	7398.4 μg h^{-1} mg^{-1}	168
NiFe LDH	NO	29.6	634.67 μg h^{-1} mg^{-1}	184
Bi NDs	NO	89.2	1194 μg h^{-1} mg^{-1}	52
*a-$B_{2.6}C@TiO_2$/Ti	NO	87.6	3678.6 μg h^{-1} cm^{-2}	187
*Ru–Cu NW/CF	NO_2^-	94.1	211 730 μg h^{-1} cm^{-2}	189
Pd/CuO	NO_2^-	91.8	906.4 μg h^{-1} mg^{-1}	192
*Cu_2O/CF	NO_2^-	94.21	7510.73 μg h^{-1} cm^{-2}	207
$Ni_3B@NiB_{2.74}$	NO_2^-	59.0	8427.75 μg h^{-1} mg^{-1}	210
Ni@JBC-800	NO_2^-	83.4	4117.3 μg h^{-1} mg^{-1}	211
C/Co_3O_4	NO_2^-	100	8198 μg h^{-1} mg^{-1}	196
Ru-ST-12	NO_3^-	—	94 520 μg h^{-1} mg^{-1}	64
Ru-CuNW	NO_3^-	96	19 1250 μg h^{-1} mg^{-1}	228
Rh@Cu-0.6%	NO_3^-	93	43 220 μg h^{-1} mg^{-1}	229
Pd (111)	NO_3^-	35	306.8 μg h^{-1} mg^{-1}	199
*a-RuO_2/CF	NO_3^-	97.46	1968.6 μg h^{-1} cm^{-2}	231
*CoP NAs/CF	NO_3^-	~100	16 252 μg h^{-1} cm^{-2}	214
Fe/Ni_2P	NO_3^-	94.3	2085 μg h^{-1} mg^{-1}	239
*Cu^0/GDYNA	NO_3^-	81.25	262 650 μg h^{-1} cm^{-2}	243
Cu MNC-x	NO_3^-	94.8	92 922 μg h^{-1} mg^{-1}	244
Fe SAC	NO_3^-	75	20 000 μg h^{-1} mg^{-1}	242
FeMo–N–C SAC	NO_3^-	94	612 μg h^{-1} mg^{-1}	225

NRR performance.[149] Besides metal single-atom catalysts that can efficiently separate the NRR from the HER, modulating the electron density near the catalyst's active sites is also an effective strategy. For instance, a catalyst of Cu NPs anchored on a polyimide (PI) surface with different conjugating degrees was prepared by a wet impregnation method. A standard NRR test over the Cu/PI-300 electrode with a Cu content of 5% resulted in the best NH_3 FE of 6.56% at −0.3 V *vs.* RHE, with an NH_3 yield rate of 12.4 μg h^{-1} cm^{-2}, outperforming the catalyst of Cu NPs fixed on a carbon substrate, which had an FE of only 0.17% and a very low yield rate of 0.7 μg h^{-1} cm^{-2}. The electron redistribution at the interface of PI and Cu NPs efficiently modulated the electron density of the Cu NPs, increasing the adsorption capacity for N_2 and activating the N_2 molecules. At the same time, the dissociation step from $*NNH_4$ to $*NH_2$ was also tailored by the electron-deficient Cu surface, thus boosting the NH_3 generation yield and selectivity.[150] The present result provides guidance in the search for catalysts to optimize this difficult reaction, from impossible to high yield. In addition to optimizing the electronic structure of catalysts by using the interaction between the supports and the active metals, changing the structural configurations of the catalyst itself also has a similar effect on improving NRR activity. For example, MoS_2 catalysts with different structural configurations, including 2H, 1T′, and 1T″ crystal structures, were synthesized by the deintercalation of potassium from a $KMoS_2$ crystal.[151] Among them, the 1T″ MoS_2 catalyst exhibited the best NRR performance, with the highest NH_3 yield rate of 9.09 μg h^{-1} mg^{-1} at −0.3 V *vs.* RHE, which was roughly 2 times that of 1T′ MoS_2 and 9 times that of 2H MoS_2. The NH_3 FE of 13.6% for 1T″ MoS_2 also surpassed that of the 2H and 1T′ MoS_2 counterparts. The formation of zigzag and diamond-like Mo–Mo chains in the 1T″ phases can efficiently change the local electron density and enhance N_2 adsorption, thereby improving the NRR kinetics. Compared with only boosting catalytic performance, metal-free materials offer the clear advantage of avoiding metal ion release, thereby reducing the environmental impact. Recently, a type of B_4C nanosheet was synthesized by the liquid-phase exfoliation method, which showed competitive NRR activity while being environmentally friendly.[152] This metal-free B_4C was capable of achieving an NH_3 yield rate and an FE as high as 26.57 μg h^{-1} $mg_{cat.}^{-1}$ and 15.95% at −0.75 V *vs.* RHE, respectively, outperforming most reported aqueous-based NRR catalysts, such as Au nanorods (an NH_3 yield rate of 1.65 μg h^{-1} cm^{-2} and a FE of 3.88%)[15] and Pd/C (an NH_3 yield rate of 4.5 μg h^{-1} mg^{-1} and a FE of 8.2%).[153] This study opens an exciting new avenue for the rational design of metal-free electrocatalysts for NH_3 synthesis with robust performance.

4.2 Nitrogen source with a plus two oxidation state, NO

Despite its natural abundance, N_2 is kinetically inert,[19,154] and at the same time, the competitive HER has faster kinetics. Therefore, scaling up this transformation technology to an industrial level is challenging. Currently, NO is a major environmentally harmful compound produced by the burning of fossil fuels in industrial processes.[55] Its increased concentrations can cause serious environmental problems, such as ozone depletion, smog, acid rain, and eutrophication, and eventually contribute to global warming,[52,56,155–157] which poses a potential risk to human health.[75,158] Currently, the selective catalytic reduction of NO is used to convert it into harmless N_2.[159] However, this method usually suffers from secondary pollution and high costs,[55,160] and many selective catalysts only show good activity at high temperatures.[159] Through this process, it can be seen that NO, with its low bond dissociation energy, is more reactive than N_2 molecules.[7,161] Meanwhile, the end products of NO reduction are often high-value products, such as NH_3, hydroxylamine (NH_2OH), and nitrous oxide (N_2O), which can be used in the production of caprolactam for the nylon industry.[162,163] A mild reaction environment and simplified reaction facilities contribute to the practical appeal of electrochemical techniques driven by renewable electricity. Taken together, the electrochemical NORR is an encouraging concept that shows great potential for both high-value NH_3 synthesis and NO elimination.[164] However, the reduction potential of the NORR process, which involves a five-electron transfer, is approximately 0.77 V *vs.* RHE,[165] and it also exhibits slow reaction kinetics and multiple intermediates, leading to an unsatisfactory NH_3 yield rate and FE.[78,166–168] Therefore, an in-depth investigation into the NORR mechanism and effective design strategies for highly active electrocatalysts will be discussed in this section.

A large number of previous studies have shown that two-dimensional materials have an ultra-high specific surface area with abundant defect sites and a controllable electronic structure, which can promote the adsorption of reactive small molecules and provide a large number of active sites, while also offering an atomic-layer-thick platform that makes it easy to study the structure–activity relationship.[169] Therefore, they are considered to be powerful catalysts for the electrosynthesis of NH_3.[31] Meanwhile, according to relevant reports, a series of precious metals have been shown to have excellent NORR activity.[170,171] Therefore, the excellent properties of dimensional engineering coupled with precious metals are expected to promote the research and development of the NORR. For example, low-coordination-number Ru nanosheets synthesized by a hydrothermal method were treated with Ar/H_2 plasma.[172] The prepared electrocatalyst exhibited excellent NORR performance; at a low NO concentration of 1%, it showed a high FE of 65.96% and a high production rate of 45.02 μmol h^{-1} mg^{-1}, clearly outperforming its counterpart of high-coordination-number Ru nanosheets, which had a low FE of 37.25% and a yield rate of 25.57 μmol h^{-1} mg^{-1}. The excellent NORR activity came from the decrease in the coordination number of Ru, which led to an upward shift of the d-band center and a decrease in the potential-determining step from *HNO to *HNOH; the adsorption of NO and the activation of the N═O bond were also promoted. Unlike dimensional engineering, an electron-rich environment also helps to improve the intrinsic NORR activity of Ru-based catalysts. Examples include anchoring Ru atoms on an electron-rich substrate or metallizing Ru species using metal substrates with lower electronegativity.[173–177] Specifically, the body-centered cubic RuGa intermetallic compound, in which Ga atoms occupy the vertices of the unit cell with Ru atoms fixed at the body center, was synthesized by a substrate-anchored thermal annealing method.[178] The RuGa intermetallic compound exhibited an excellent NH_3 FE of 72.3% and production rate of 320.6 μmol h^{-1} mg^{-1} for NH_3 synthesis at −0.2 V *vs.* RHE, which was higher than that of hexagonal close-packed Ru NPs, with a lower FE of 59.8% and a yield rate of 235.4 μmol h^{-1} mg^{-1}. After the introduction of Ga species, the RuGa intermetallic compound showed metallic characteristics with a band gap of 0. At the same time, the bimetallic compound displayed a lower energy barrier for the RDS step (adsorbing and activating the *HNO intermediate), which decreased from the original 0.88 eV to 0.49 eV. These factors together accelerated the transformation of NO by speeding up the activation of N–O bonds *via* electron supply from the Ru atoms.

Considering that the low abundance and high price of noble metals and their alloys hinder their industrial applications,[52] the electrocatalysts made from earth-abundant elements are inevitable. Recent DFT calculations show that Cu exhibits excellent activity for the NORR as well as superior selectivity for NH_3 over H_2. Therefore, a commercial Cu foam was directly used as an independent, self-supporting catalyst for NORR reactions, which can even reach the level of the H–B process, displaying a record-high yield rate of 517.1 μmol h^{-1} cm^{-2} and an NH_3 FE of 93.5% in 0.25 M Li_2SO_4 at −0.9 V *vs.* RHE.[78] Thus, numerous Cu-based catalysts have been explored for facilitating the NORR process. For example, the working electrode of an NORR cell was produced by depositing a commercial Cu ink (Cu particle size <100 nm) on a gas diffusion layer with a loading of 0.25 mg cm^{-2}. This prepared Cu electrode exhibited a high NH_3 FE of roughly 90% and a yield rate of 1806 μmol cm^{-2} h^{-1}, which was superior to electrodes formed by deposition of other metals, including Fe, Co, Ni, Pd, Ag, and Pt. Furthermore, the relationship between NO concentration and N–N coupling was discovered through the NORR process using this Cu electrode at different NO concentrations. N–N coupling and single N products were preferred at high and low NO coverage rates, respectively. In addition, by exploring the local pH of the reaction environment, it was found that the Cu-based catalyst could reach a nearly 100% NH_3 FE of 100% under acidic conditions, while the FE of NH_3 dropped to about 80% under alkaline conditions, which provided guidance for optimizing the selectivity of NORR products.[167] Aiming to reduce NO in gaseous pollutants at a low cost, transition-metal dichalcogenide materials also exhibit admirable electrocatalytic ability for facilitating the NORR process.[55,179,180] For example, CoS containing S defects (CoS_{1-x}) was prepared *via* plasma treatment for 2 minutes at 300 W in an Ar atmosphere. The as-synthesized CoS_{1-x} showed excellent NORR activity in 0.2 M Na_2SO_4, with a high NH_3 FE of 53.62% and a large NH_3 yield rate of 44.67 μmol cm^{-2} h^{-1}, significantly outperforming natural CoS, which had a lower FE of 36.68% and a small NH_3 yield rate of 27.02 μmol cm^{-2} h^{-1}. Due to the localization of electrons near the S defects, the activation process of NO was promoted. Meanwhile, the *NO + H → *NOH step was also accelerated, thus showing remarkable NORR performance.[180]

Compared with defect engineering to accelerate the NORR process, doping engineering for transition-metal dichalcogenide materials also shows excellent activity. Recently, MoS_2 has been reported as an effective NORR catalyst. Benefiting from a large number of positively charged Mo sites, which could facilitate NO adsorption and activation *via* an 'acceptance–donation' mechanism and disfavor the binding of protons as well as the coupling of N–N bonds, the MoS_2 electrocatalyst attained a high FE of 76.6% and an NH_3 yield rate of 99.6 μmol cm^{-2} h^{-1} in an acidic electrolyte.[55] The results above indicate that the single MoS_2 catalyst is expected to improve its catalytic activity through further modification. For instance, a Co_1/MoS_2 catalyst with $Co_1–S_3$ active sites was successfully constructed by an impregnation strategy in a $Co(Ac)_2·4H_2O$ solution, in which a Co atom was introduced onto the MoS_2 surface supported on carbon cloth. The as-synthesized Co_1/MoS_2 catalyst exhibited an extremely high FE of 87.7% and an outstanding NH_3 yield of 217.60 μmol cm^{-2} h^{-1}, substantially outperforming pristine MoS_2. In the $Co_1–S_3$ active sites formed by the doping of foreign metal atoms, Co and S species jointly activated NO and improved its coverage, while the adsorption of *H was thermodynamically prohibited, clearly indicating the advantage of doping engineering.[168]

In addition, it should also be clear that the formation of N_2 and N_2O by-products in the NORR process is very thermodynamically favorable.[181,182] Therefore, to further achieve high selectivity of the NORR to NH_3, it is necessary to construct a suitable catalyst that can effectively prevent both N–N bond coupling and *N diffusion.[164] At the same time, based on the discussion above, we believe that the results of combining dimensional engineering and doping engineering to regulate the catalyst will be very interesting and fascinating. Along these lines, based on high-throughput first-principles calculations, by confining 27 transition metal atoms (including all 3d, 4d, and 5d transition metal elements, except Zn, Cd, and Hg) on an MoS_2 platform with an S defect, it was found that Ti, Fe, Co, Ni, Cu, and La@MoS_{2-x} showed excellent NORR performance in theory.[183] By anchoring these transition metal atoms through the S defects, the confined space of the S defect sites effectively prevents the approach of two NO molecules by strongly binding the N atoms, thus hindering N–N bond coupling to form N_2O_2. The under-coordinated Mo edges as active sites would thus guarantee the high selectivity of NO-to-NH_3.[183]

In addition to optimizing the NORR by regulating the adsorption and activation of NO and reducing the occurrence of by-products, decreasing the hydrogen evolution kinetics of the catalysts is also a powerful means. For instance, NiFe LDH was synthesized on Ni foam by a one-step hydrothermal strategy at 120 °C with the assistance of ethylene glycol. The produced NiFe LDH displayed an excellent FE of 82% and a large NH_3 yield rate of 112 μmol cm^{-2} h^{-1}, beyond the reported Ru-based catalysts with an NH_3 FE of 29.6%. The Ni foam with its porous structure could prevent the accumulation of catalysts, exposing numerous active sites to adsorb or transport reactants, and the NiFe-LDH nanosheets effectively inhibited the HER, thus showing excellent NORR activity.[184] Furthermore, due to the potential environmental contamination caused by the extensive use of metal-based catalysts, a non-toxic and environmentally friendly metal, Bi, has been reported as a promising alternative for high-efficiency electrochemical applications.[185,186] Therefore, highly active Bi nanodendrites were prepared by electrochemical deposition on the surface of a Ti film for 1200 s in a 1.0 mM $BiCl_3$ solution at −0.5 to −0.8 V *vs.* Ag/AgCl. They attained a high FE of 89.2% at −0.5 V *vs.* RHE and a remarkable NH_3 yield rate of 1194 μg h^{-1} $mg_{cat.}^{-1}$, which clearly outperformed Bi powder. The excellent catalytic activity of the NORR came from the spiky structure of the Bi nanodendrites, which could amplify the local electric field near the tip and promote the adsorption and activation of NO molecules through an effective charge redistribution mechanism.[52]

In the past, various precious metal- and non-precious metal-based catalysts have been used to accelerate the NORR process. The development of non-metallic materials with high electrical conductivity, excellent electrochemical stability, and good corrosion resistance is inevitable for environmental sustainability and large-scale industrial applications.

Recently, for instance, a kind of amorphous boron carbide ($B_{2.6}C$), as a free-standing electrode, was successfully synthesized through the magnetron sputtering technique onto a TiO_2/Ti substrate.[187] It showed sustained and superb NORR activity for synthesizing NH_3, with a high FE of 87.6% and an amazing yield rate of 3678.6 μg cm^{-2} h^{-1}, superior to the pristine TiO_2/Ti plate, which had an FE of 42.6% and an NH_3 yield rate of 563.5 μg cm^{-2} h^{-1}. Benefiting from the enlarged electrochemical active area and the B–C bonds over the $B_{2.6}C$ layer, external electrons were effectively injected into the NO molecules, and the bond length of N–O was adjusted from 1.15 Å to 1.41 Å, jointly activating the NO molecules and thus exhibiting excellent NORR performance.

4.3 Nitrogen source with a plus three oxidation state, NO_2^-

Currently, the high dissociation energy of the N≡N triple bond (941 kJ mol^{-1}), the extremely low solubility of N_2 in aqueous media, and the overwhelming competition from the HER are the main reasons preventing the widespread application of the NRR.[21,188,189] Therefore, it is urgent to find a suitable N source for efficient electrosynthesis. Currently, large quantities of nitrite (NO_2^-) flow into surface water and seep into groundwater as a result of agricultural production and industrial discharges, which not only damages ecosystems but also poses a serious threat to human health.[92,190–192] Specifically, the ingestion of NO_2^- can lead to the production of *N*-nitrosoamine byproducts, which have been shown to be carcinogens. It also damages hemoglobin, leading to cell degradation and even brain damage in infants.[193] Therefore, the recovery and transformation of NO_2^- are of great significance to human health and the nitrogen cycle.

The conversion of environmentally harmful NO_2^- to high-value NH_3 through electrochemical reduction is a promising green and sustainable solution.[194,195] In fact, NO_2^- is an attractive source of nitrogen because of its lower dissociation energy and better solubility compared to N_2.[192] Meanwhile, compared with the nitrogen resource NO, NO_2^- exhibits a higher reduction potential of 0.897 V *vs.* RHE. However, the electrocatalytic conversion process from NO_2^- to NH_3 (NO_2RR) usually faces slow kinetics and a complex distribution of products, which greatly hinders the progress of NH_3 synthesis.[197] Therefore, this section mainly summarizes the research on high-efficiency NO_2RR electrocatalysts and provides guidelines for future research and design methods in this field.

At present, among various transition metal-based catalysts, Cu-based materials have become the most attractive catalysts for the electrochemical conversion of NO_x to value-added NH_3.[189,198] For example, a Cu nanowire anchoring Ru atom (Ru–Cu NW/CF) electrocatalyst was synthesized by a cation exchange strategy, in which Cu foam covered with $Cu(OH)_2$ nanowires was immersed in a 5.0 mmol L^{-1} $RuCl_3$ solution for 2 hours, followed by annealing at 180 °C to complete the Ru loading. The synthesized Ru–Cu NW/CF displayed an outstanding FE of 94.1% and a large NH_3 yield rate of up to 211.73 mg h^{-1} cm^{-2} at −0.6 V *vs.* RHE, which was approximately 5.0 times higher than that of the Cu NW/CF. By introducing single-atomic Ru into the Cu lattice, the adsorption capacity of the catalyst for NO_2^- was improved. Meanwhile, the Ru–Cu NW/CF had a faster RDS from *NO to *NOH compared with the Cu NW/CF, thus displaying excellent NO_2RR performance.[189] Besides, the modulation of morphology and structure and the introduction of 4d-block atoms like Pd are attractive strategies to improve the activity of Cu-based catalysts.[192,199,200] For example, $CuCl_2$ was reacted with a Na_2PdCl_4 solution in a water bath at 60 °C to prepare two-dimensional Pd/CuO catalysts with heterogeneous interfaces and porosity. The obtained Pd/CuO catalyst exhibited an excellent NH_3 yield rate of 906.4 μg mg^{-1} h^{-1} and a high FE of 91.8%, which was significantly better than Pd NPs (an FE of 29% and an NH_3 yield rate of 298.4 μg mg^{-1} h^{-1}) and CuO (an FE of 86% and an NH_3 yield rate of 920.4 μg mg^{-1} h^{-1}). A built-in electric field was spontaneously constructed at the Pd/CuO heterointerface, which optimized the electronic structure of Pd and Cu, thereby enhancing the electrical conductivity. Meanwhile, Pd NPs could also increase the selectivity for NH_3 by forming adsorbed H, which jointly boosted the NO_2RR performance.[192]

In addition to transition metals in the 4d region, 5d region transition metals have the potential to further improve the selectivity of the NO_2RR. For instance, based on DFT calculations, it was found that compared to precious metals in the 4d region (*e.g.*, Ru, Pd), precious metals in the 5d region could have higher theoretical H surface coverages.[193,201] Considering the economic problems in the catalyst preparation process and that alloying engineering could optimize NO_2RR activity,[202–204] a 5d region noble metal alloy is expected to further improve the selectivity and formation rate of NH_3. Recently, a Cu_xIr_{1-x} (x = 10, 25, and 100) nano-alloy was successfully prepared in a microwave reactor at 125 °C. The developed Cu_xIr_{1-x} exhibited 100% selectivity for NH_3 in a near-neutral environment, with performance similar to that of commercial Pd NPs for the NO_2RR in industry.[193] The H-coverage of the Ir atom was higher than that of the Pd atom, indicating that Ir could thermodynamically accommodate more adsorbed H on its surface, thus showing higher NH_3 selectivity. Although noble metal-based catalysts with excellent activity have been constructed using single-atom and alloying engineering, non-noble catalysts are still the most promising candidates for the industrialized production of NH_3.[205,206] For example, a simple electrode of Cu_2O particles supported by Cu foam (CF@Cu_2O) was synthesized by an anodic oxidation process at 5.0 V for 5.0 minutes, combined with an annealing treatment at 550 °C. The CF@Cu_2O catalyst displayed a remarkable FE of 94.21% combined with a high production rate of 7510.73 μg h^{-1} cm^{-2}, superior to the Cu foam electrode (an FE of 55.1% and an NH_3 yield rate of 1450.12 μg h^{-1} cm^{-2}). Compared with Cu (111), Cu_2O (111) had a lower energy barrier for the RDS from *NO to *NOH, and it could inhibit the HER process, thereby facilitating the NO_2RR.[207] Besides, considering that an acceptable FE and NH_3 yield rate were usually obtained at high overpotentials, another 3d metal, Ni, with a strong adsorption capacity for NO_2^-, is expected to solve these difficulties.[208] However, it should be noted that Ni atoms have very high activity for the HER.[209] Recently, a type of Ni-based catalyst of surface B-rich core–shell nickel boride NPs (Ni_3B@$NiB_{2.74}$) was prepared by a wet chemistry method, in which $Ni(CH_3CO_2)_2{\cdot}4H_2O$ was stirred with $NaBH_4$ and annealed at 300 °C (Fig. 6(a) and (b)). The prepared Ni_3B@$NiB_{2.74}$ NPs exhibited about 100% conversion efficiency of NO_2^- to NH_3, with a significant NH_3 yield rate of 198.3 μmol cm^{-2} h^{-1} at −0.3 V *vs.* RHE. The NH_3 FE of the control Ni NPs, 59.0%, was about 1.6 times lower than that of Ni_3B@$NiB_{2.74}$ (Fig. 6(c)). The surface-enriched, electron-deficient B sites promoted the adsorption of liquid NO_2^-, which also transferred electrons to the Ni sites to prevent their oxidation and diluted the Ni sites available to participate in the HER (Fig. 6(d) and (e)), thus improving the catalytic activity of the NO_2RR (Fig. 6(f) and (g)).[210] In addition to modification methods involving non-metallic element doping, the selection of a suitable catalyst support is also an effective strategy. For example, juncus soaked in a Ni salt solution was annealed at a high temperature for about 2.0 hours to successfully produce a kind of Ni NP-based catalyst on juncus-derived biomass carbon (Ni@JBC-800).[211] When tested for the NO_2RR, the Ni@JBC-800 catalyst was capable of exhibiting a remarkable NH_3 yield rate of 4117.3 μg h^{-1} mg^{-1} and a high FE of 83.4% at −0.5 V *vs.* RHE, surpassing most reported Ni-based catalysts, such as Ni_2P nanosheets (an FE of 90.2% and an NH_3 yield rate of 2692.2 μg h^{-1} cm^{-2})[212] and Ni–NSA–V_{Ni} (an FE of 88.9% and an NH_3 yield rate of 4011.6 μg h^{-1} cm^{-2}).[213] Benefiting from biomass-derived carbon as a carrier, it could not only prevent the agglomeration of catalysts but also improve conductivity. Meanwhile, the empty tubular structure of juncus in the 3D interconnect also facilitated gas and electrolyte diffusion, increasing NO_2RR activity. In addition, promoting the transport of ions or electrons by inducing the redistribution of charges near the doping sites is also a powerful means to improve catalytic activity.[214–216] Recently, carbon-doped hollow nanotubes were prepared *via* the *in situ* topotactic conversion of $C_2O_4^{2-}$-doped CoC_2O_4 to C^{4+}-doped Co_3O_4 at 400 °C (C/Co_3O_4). Such C/Co_3O_4 exhibited an ultrahigh FE of about 100% from −0.1 V to −0.6 V *vs.* RHE and a large NH_3 yield rate of 4.10 mg h^{-1} cm^{-2} at −0.6 V *vs.* RHE, significantly outperforming the Co_3O_4 catalyst, which had a poor NH_3 yield rate of 1.78 mg h^{-1} cm^{-2}. C-doping enhanced the adsorption and activation ability for NO_2^- ions and also led to a fast charge transfer process. At the same time, this, coupled with the lower energy barrier required for the potential-determining step ($*N + e^- + H_2O \rightarrow *NH + OH^-$) jointly promoted the NO_2RR process.[196] In addition to optimizing the morphology and electronic structure of catalysts, optimizing the reaction conditions can also be used as a strategy to enhance the activity of the NO_2RR. For example, a continuous and scalable plasma–electrochemical hybrid technology was developed for NH_3 production (Fig. 6(h)), which coupled a plasma reactor with an electrochemical H-cell to activate air and improve the reaction rate and energy efficiency (Fig. 6(i)–(m)). The working electrode was Cu foam covered with Cu nanowires, which exhibited an excellent FE of 100% and a yield rate of 45 nmol s^{-1} cm^{-2}.[217] Compared with the traditional NH_3 electrosynthesis process, it was worth noting that the plasma-assisted conversion system was characterized by lower energy consumption (253 kW h kg^{-1} NH_3) (Fig. 6(n)). Therefore, this hybrid technology facilitates on-site, decentralized production of NH_3 that can be powered by cheap, surplus renewable resources.

4.4 Nitrogen source with a plus five oxidation state, NO_3^-

To further overcome the challenges of slow NRR dynamics, discovering and using new nitrogen sources is key. NO_3^- is the second most abundant form of nitrogen and is present at high concentrations as an environmental pollutant in industrial waste streams and water runoff.[218,219] The electrochemical NO_3RR is attractive due to the large solubility of NO_3^- in

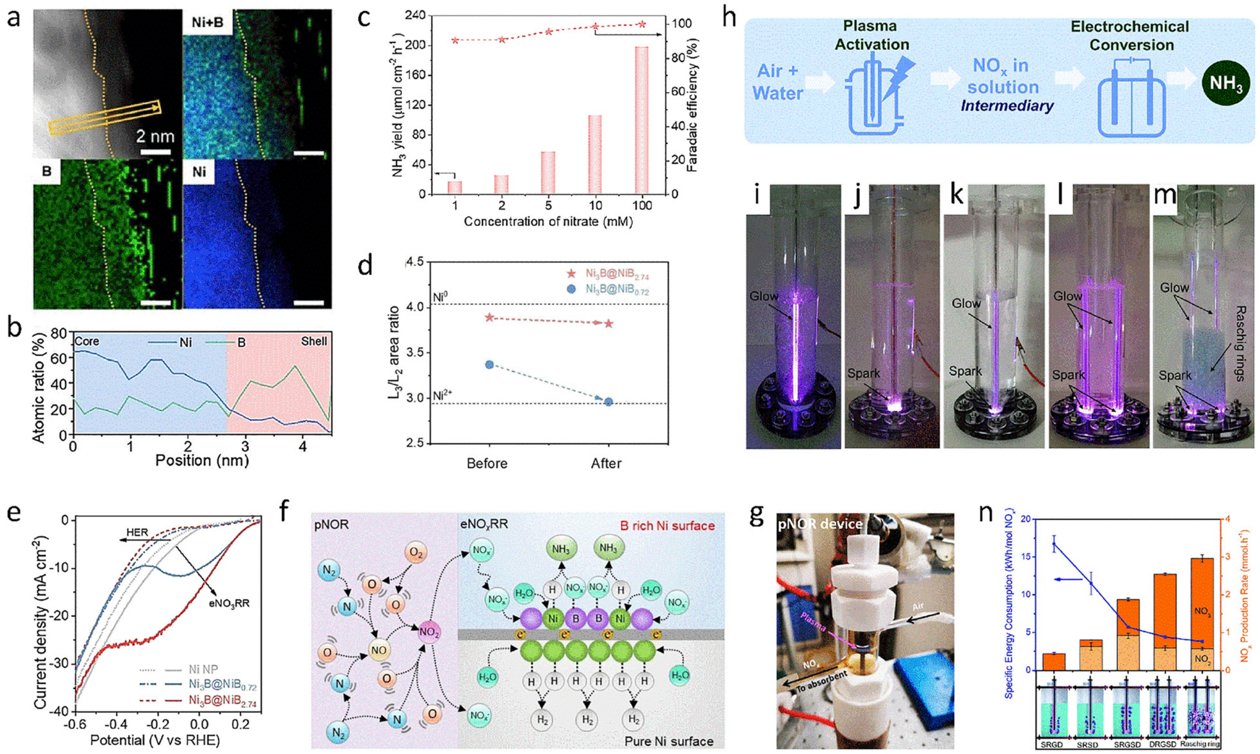

Fig. 6 (a) EDX elemental mapping of $Ni_3B@NiB_{2.74}$. (b) Linear scan of $Ni_3B@NiB_{2.74}$. (c) NH_3 yield rate and FE of $Ni_3B@NiB_{2.74}$. (d) L_3/L_2 area ratio in the EELS spectrum of different samples for illustrating the Ni species effectively protected, thus preventing Ni sites from participating in the HER process. (e) LSV curves of different samples with and without NO_3^- for illustrating dominance of the HER and the NO_3RR. (f)–(g) Diagram of the mechanism about boosted NH_3 synthesis performance and related device. (h) Schematic illustration of plasma combined with electrocatalytic technology for NH_3 synthesis. (i)–(m) Digital photos of different plasma reactors. (n) Energy consumption and NO_x yield rate of different plasma reactors. Reproduced with permission from ref. 210 Copyright 2021, Wiley-VCH. Ref. 217 Copyright 2021, The Royal Society of Chemistry.

aqueous electrolytes and its relatively low bond dissociation energy (204 kJ mol^{-1}). Meanwhile, the NO_3RR avoids the activation of the N$\equiv$N bond and the complex gas–liquid–solid interfacial reactions, providing a more practical route.[67,220,221] In previous studies, the NO_3RR has been extensively studied for denitrification and water purification.[222,223]

Recently, significant attention has shifted to the selective reduction of NO_3^- to NH_3 *via* the eight electron transfer pathway (E_0 = 0.82 V *vs.* RHE).[221] The eight-electron transfer pathway is very complex, involving many potential reaction intermediates (NO_2, NO_2^-, NO, N_2O, N_2, NH_3, NH_2OH, and N_2H_4), in which the initial reduction from NO_3^- to NO_2^- is considered the RDS.[224] Further, depending on the electrolyte conditions and the adsorption strength of the intermediates on the catalyst surface, the reduced *NO is selectively shunted to either NH_3 or N_2.[225] It is worth noting that, according to thermodynamic theory, the most stable product of the NO_3RR is N_2, which has the highest equilibrium potential of all possible products in the NO_3RR process (E_0 = 1.246 V *vs.* SHE).[67] Therefore, challenges still exist in the NO_3RR, such as slow reaction kinetics and low product selectivity, which greatly restrict its further application.

Specifically, it is well known that the NO_3RR process involves the transfer of eight electrons coupled with nine protons, during which nitrogen oxyanions and dinitrogen are unavoidably generated as undesired byproducts.[64] For traditional electrocatalysts, high selectivity for NH_3 could be obtained only under low overpotential conditions, as the HER dominated under high current conditions.[62,226,227] Therefore, catalysts that inhibit the HER process are expected to achieve the efficient synthesis of NH_3. For instance, an Ru/O-doped-Ru core/shell nanocluster with tensile strain was successfully constructed by a modified sol–gel route (Fig. 7(a)–(c)), in which the strained Ru-ST-12 nanocluster was synthesized by an electrochemical redox process of amorphous ruthenium oxychloride nanoclusters. The synthesized electrocatalyst displayed an excellent NH_3 yield rate of 5.56 mol $g_{cat.}^{-1}$ h^{-1} (Fig. 7(d)), in contrast to the NH_3 yield rate of Ru nanoclusters with a close-to-zero strain (0.10 mol $g_{cat.}^{-1}$ h^{-1}), which was much lower than that of Ru-ST-12. The main contributor to this excellent NO_3RR performance came from the stretched lattice strain inhibiting the HER, while the lattice strain favored the formation of *H for promoting the hydrogenation of key intermediates to form NH_3.[64] To inhibit the competitive HER, constructing the catalyst with a suitable substrate is also a favorable strategy. Recently, a Cu nanowire catalyst with highly dispersed Ru atoms (Ru–CuNW) was obtained by a cation exchange process for Cu foam containing $Cu(OH)_2$ nanowires in a $RuCl_3$ solution for 12 hours.[228] The Ru–CuNW reached a maximum NH_3 FE of 96% at 0.04 V *vs.* RHE and showed a large NH_3 generation rate of 76 500 μg h^{-1} cm^{-2} (Fig. 7(e)), which significantly outperformed the CuNW (31% FE) and Ru NPs (52% FE). The introduction of highly dispersed Ru

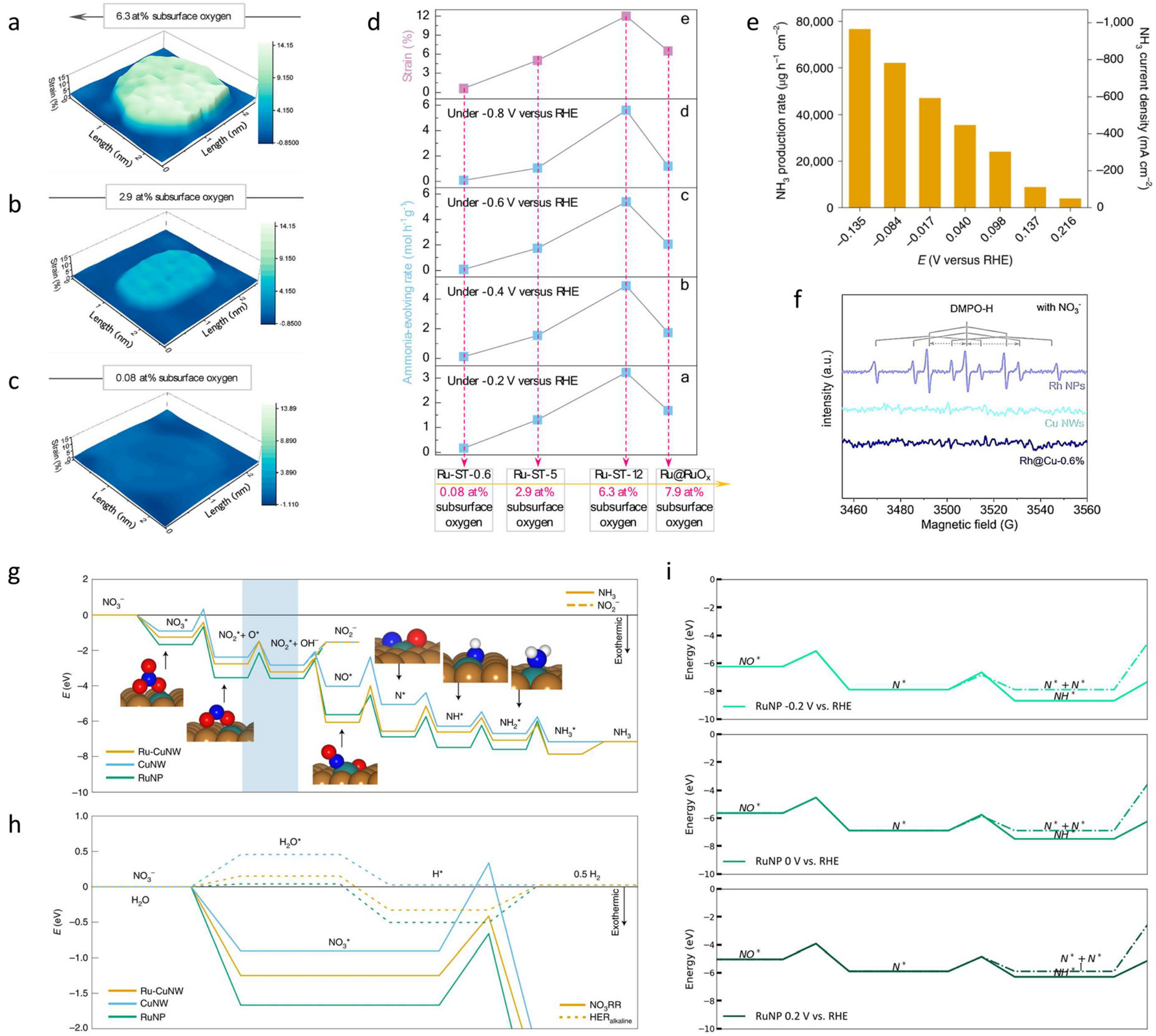

Fig. 7 (a)–(c) Diagram of an Ru/oxygen-doped-Ru core/shell nanocluster with different degrees of tensile strains. (d) NH_3 yield rate of an Ru/oxygen-doped-Ru core/shell nanocluster with different degrees of tensile strains. (e) NH_3 yield rate of the Ru–CuNW sample. (f) Electron paramagnetic resonance spectra of different catalysts. (g) Free energy diagram for different catalysts during the NO_3RR process. (h) Free energy diagram for NO_3^- adsorption and the HER process of different catalysts. (i) Free energy diagram for adsorbed N behaviour. Reproduced with permission from ref. 64 Copyright 2020, American Chemical Society. Ref. 228 Copyright 2022, Springer Nature.

atoms provided additional adsorption sites for NO_3^- and inhibited the desorption of the $*NO_2^-$ intermediate (Fig. 7(f) and (g)). The N–N coupling process was concurrently prevented by limiting the movement of N* species on the catalyst surface (Fig. 7(h)). Meanwhile, the surrounding Cu sites inhibited the progression of the HER (Fig. 7(i)), thus increasing the activity of the NO_3RR. Recently, it has been reported that improving the surface hydrogenation capabilities of the catalyst also contributes to the generation of NH_3. For example, Rh single atoms and clusters were loaded on Cu substrates by using the difference in reduction potentials of the Cu and Rh elements (Rh@Cu-0.6%), in which a 1.0 cm^{-2} Cu foil supporting Cu nanowires was soaked in $RhCl_3$.[229] This Rh@Cu-0.6% catalyst showed an NH_3 FE of 93% at −0.2 V *vs.* RHE and reached a record yield rate of 21.61 mg h^{-1} cm^{-2} at −0.4 V *vs.* RHE. The performance of Rh@Cu-0.6% was obviously improved compared with Cu NWs (an FE of 72% at −0.2 V *vs.* RHE) and Rh NPs (an FE of 12% at −0.2 V *vs.* RHE). The synergistic effect between the Cu and Rh species enhanced the activity of the NO_3RR, in which the adsorbed hydrogen on the Rh sites transferred to the *NO intermediate, which facilitated hydrogenation and the formation of NH_3. In addition to inhibiting the competitive HER during the NO_3RR, finding suitable strategies to preferentially form *NO and $*N_2O$ intermediates is also critical to the synthesis of NH_3.[199,230] Recently, nanocubes, cuboctahedra, octahedra, and concave nanocubes of Pd catalysts with controlled lattice planes were synthesized to explore the relationship between shape-controlled catalysts and NO_3RR activity. According to the electrochemical NO_3RR test, the order of NO_3RR activity was Pd (111) > Pd (100). The cuboctahedron sample with both Pd (111) and Pd (100) planes demonstrated the highest NH_3 yield rate of 306.8 μg h^{-1} mg_{Pd}^{-1} with an FE of 35%. Benefiting from the eight (111) facets and six (100) facets constructing the cuboctahedron

Pd, the (111) facets had fast dynamics for activating and reducing NO_3^- to NO_2^- and the (100) facets were good at reducing NO_2^- to NH_3. Thus, controlling the nanostructures and facets of Pd could boost the NO_3RR performance.[199] In addition to doping engineering and the regulation of structures with specific lattice planes, the degree of structural disorder of catalysts is also one of the strategies to improve the activity of the NO_3RR. For example, amorphous (a-RuO_2), low crystallinity (lc-RuO_2), and high crystallinity RuO_2 nanosheets (hc-RuO_2) covered on carbon paper were synthesized by a molten salt method by tailoring the calcination temperature and time. Among them, compared with lc/hc-RuO_2, a-RuO_2 exhibited the highest NH_3 FE of 97.46%, far outperforming the counterparts of lc/hc-samples, which had FEs of 55.27% and 7.03%, respectively. The results above revealed that amorphous structures with numerous vacancies could regulate the d-band center of Ru and suppress the HER process, thus resulting in a low energy barrier for the RDS ($*NH_2 \rightarrow *NH_3$) and promoting catalytic performance.[231] Considering the rarity of precious metals and the economics of the catalyst preparation process, the use of non-precious-metal-based electrocatalysts is inevitable. Inspired by a related report that showed that Co-based materials can selectively produce NH_3 through the NO_3RR like Rh-based materials,[232] a CoP nanosheet array fixed on carbon fiber (CoP NAs/CF) was produced by an annealing treatment of $Co(OH)_2$ NAs/CF in NaH_2PO_2 at 300 °C, in which an electrodeposition method was used to synthesize $Co(OH)_2$ NAs/CF. The NO_3RR performance was recorded at -0.3 V *vs.* RHE, and the CoP NAs/CF exhibited an NH_3 generation rate of 9.56 mol h^{-1} m^{-2} with a high FE of $\sim$100%, which significantly outperformed the H–B method. The introduction of P species accelerated the RDS from $*HNO_3$ to $*NO_2$, and the surface self-reconstruction of CoP to form $Co(OH)_2$ could promote water splitting to release active hydrogen to hydrogenate the adsorbed NO_3^-, improving the production efficiency of NH_3.[214] Apart from this, other first-row transition metal phosphides (*e.g.*, Mn, Fe, Ni, and Cu) have also been proven not only to be excellent alternatives for the HER,[233,234] but also to exhibit some hydrogenation-treating abilities, such as hydrodesulfurization, hydrodeoxygenation, and hydrodenitrogenation.[235–238] For example, an Fe-doped Ni_2P (Fe/Ni_2P) catalyst was constructed by an annealing treatment of the compounds of NiFe LDH and NaH_2PO_2 at 300 °C. The as-prepared electrocatalyst exhibited prominent NO_3RR performance, with an FE of 94.3% and an excellent NH_3 yield rate of 4.17 mg h^{-1} cm^{-2} at -0.4 V *vs.* RHE. Owing to the Fe doping, the d-band center and electronic structure of the Ni species were altered, and the RDS was also changed from $*NO + 2H^+ + 2e^- \rightarrow *N + H_2O$ to $*NO_2 + H_2O + 2e^- \rightarrow *NO + 2OH^-$, indicating more favorable kinetics for the NO_3RR on Fe/Ni_2P. This work highlighted the prospect of bimetallic phosphides for the NO_3RR.[239] As the NO_3RR involves many possible intermediates and products,[221,240–242] the rational design and construction of catalysts at the atomic level could further optimize this complex reduction process. For instance, a zero-valent atomic Cu catalyst immobilized on graphdiyne (Cu^0/GDY) was produced by electrochemical deposition at 10 mA cm^{-2} for 200 s.[243] The highly monodispersed Cu^0 catalyst achieved a high FE of 81.25% and a large NH_3 yield rate of 15.45 mmol h^{-1} cm^{-2}, which was better than the pristine GDY, with a negligible NH_3 yield rate and FE. Due to the incomplete charge transfer between GDY and the zero-valent Cu atoms, the Cu^0/GDY catalyst was endowed with extremely high activity, which showed that zero-valent atomic-based electrocatalysts could be used as a goodplatform to convert NO_3^- to NH_3. In addition, adjusting the coordination environment of a single metal site can also result in a favorable thermodynamic process for the electrosynthesis of NH_3. For instance, an atomic-Cu anchored N-doped carbon (NC) catalyst with Cu(I)–N_3C_1 sites was prepared by the pyrolysis of a Cu ZIF-8 precursor at 950 °C. NO_3RR experiments demonstrated that this catalyst displayed a large NH_3 yield rate of 5466 mmol g_{Cu}^{-1} h^{-1} and a conversion efficiency of 94.8% for NO_3^- at -0.64 V *vs.* RHE, which was obviously superior to the traditional Cu NC, with a 72.2% conversion efficiency. The coordination environment of Cu(I)–N_3C_1 localized the charge around the Cu sites and adsorbed the intermediates $*NO_3$ and *H onto neighboring Cu/C sites, stabilizing the adsorbed *H for hydrogenation and suppressing the HER. It could also boost the RDS from $*HNO_3$ to $*NO_2$, thus leading to a thermodynamically favorable process for the NO_3RR.[244] In addition to the development of single-atomic Cu-based materials, Fe-based compounds have been used in the Haber–Bosch process for highly efficient NH_3 synthesis at an industrial grade.[28,49,92] Therefore, the reasonable design of single-atomic Fe-based catalysts is expected to achieve a breakthrough in the performance of the NO_3RR. Recently, an Fe single-atom catalyst (Fe SAC) was synthesized by a transition-metal-assisted carbonization strategy using silicon dioxide as a template; specifically, pyrolysis of a mixture including a metal salt, o-phenylenediamine, and silicon dioxide. The catalyst delivered a high FE of 75% at -0.66 V *vs.* RHE and an impressive NH_3 production rate of about 20 000 μg h^{-1} $mg_{cat.}^{-1}$, whereas the NH_3 yield rate of Fe NPs was only half that of the Fe SAC, at about 11 500 μg h^{-1} $mg_{cat.}^{-1}$. More importantly, the lack of neighboring metal sites in the Fe SAC could effectively prevent the N–N coupling step, combined with a favorable RDS including *NO to *HNO and *HNO to *N, thereby boosting the selectivity and yield rate of NH_3. In addition, based on this high performance, to further optimize the NO_3RR process for obtaining a controllable reaction path and high selectivity for the ideal target products, bi-single-atomic electrocatalysts with multiple active sites can be used as a general design strategy for heterogeneous catalysis.[242] For example, an FeMo–N–C SAC catalyst was synthesized *via* the sacrificial support method. The activity of the bimetallic catalyst FeMo–N–C SAC for the NO_3RR was obviously improved compared with its monometallic counterparts of Fe or Mo SAC. Specifically, the FeMo–N–C SAC showed an increased FE of up to 94% at -0.45 V *vs.* RHE, with the NH_3 yield rate improved to 18.0 μmol cm^{-2} h^{-1}, which was 1.8 times greater than Fe–N–C and 3.5 times greater than Mo–N–C. By integrating individual Fe and Mo sites on a single catalyst, unique reaction pathways were synergized, in which Mo sites could promote the dissociative–adsorption process of $*NO_3^-$, and then the Fe sites exhibited fast kinetics for reducing $*NO_2^-$ to NH_3, thus achieving high performance for the NO_3RR. This cascade design provided guidelines for future sustainable NH_3 synthesis.[225]

5. Photoelectrochemical synthesis of ammonia

Various strategies have been explored to promote NH_3 synthesis, including biochemical, photocatalytic, electrochemical, and photoelectrochemical (PEC) methods.[245–247] The PEC approach is a promising technology for NH_3 production because it combines the advantages of both photocatalysis and electrocatalysis to facilitate N_2 conversion.[248,249] This approach not only allows for the possibility of NH_3 production under mild conditions, such as ambient temperature and atmospheric pressure, but can also be powered by sunlight.[250] The PEC process includes the following specific steps: (i) the absorption of light and the excitation of charge carriers; (ii) the separation and transport of photoexcited carriers to the surface of the photoelectrode; and (iii) reactions involving oxidation or reduction on the catalyst's surface.[251] Hence, designing and constructing photoelectrode materials with broad solar spectral absorption, fast charge carrier generation and separation, and a large and effective catalytically active surface, while also adsorbing enough N_2 molecules, is crucial for achieving a high-efficiency PEC process, especially at low overpotentials.[252,253] The relevant prepared photoelectrode materials and their PEC activities are summarized in Table 3.

A few studies have recently been reported on the PEC conversion of N_2 to NH_3. For example, a Cu_2O photocathode was constructed by an electrochemical deposition strategy to study PEC N_2 reduction. Using isotopically labeled $^{15}N_2$ in a 0.1 M KOH solution under simulated solar illumination, the FE of the Cu_2O photocathode to produce $^{15}NH_3$ was 20% at 0.4 V *vs.* RHE. This potential was significantly more positive than the thermodynamic reduction potential of N_2, suggesting that using photoexcited electrons in the Cu_2O photocathode could reduce the energy required for NH_3 production (Fig. 8(a)).[254] This work strongly showed the effectiveness of PEC technology for NH_3 synthesis. However, it is worth noting that the photoelectrodes used for PEC NH_3 production usually face problems such as low light absorption ability, limited carrier transport, low selectivity, and a low yield rate. As a potential material, antimony selenide (Sb_2Se_3) has the advantages of a narrow band gap of ~1.2 eV, strong light absorption, and fast charge transfer capacity. Recently, a photocathode was synthesized by a spin-coating method, followed by annealing at 350 °C. Furthermore, a TiO_2 layer was deposited on the as-prepared Sb_2Se_3 photocathode and then coated with a CoCu co-catalyst by electrodeposition (Fig. 8(b)), resulting in a final photocathode named $CoCu/TiO_2/Sb_2Se_3$.[37] The $CoCu/TiO_2/Sb_2Se_3$ photocathode exhibited a high FE of 88.01% and a yield rate of 15.91 μmol h^{-1} cm^{-2} (Fig. 8(c)), which was 20 times higher than that of TiO_2/Sb_2Se_3. Due to its excellent light absorption capacity, carrier transfer capability, and charge separation efficiency (Fig. 8(d)), the $CoCu/TiO_2/Sb_2Se_3$ photocathode effectively adsorbed the NO_3^- reactant and intermediates, while the CoCu co-catalyst optimized the thermodynamic energy barrier of the NO_3RR and HER processes, thus jointly resulting in a high PEC activity. In addition to the design of heterostructures, the modification of the photoelectrode's own nanostructure is also expected to solve the problems of low PEC performance. A kesterite (Cu_2ZnSnS_4 (CZTS)) photocathode was synthesized by

Table 3 Summary of the previously reported state-of-the-art catalysts for the efficient PEC NH_3 synthesis

Catalysts	Nitrogen source	Experimental conditions	Faraday efficiency (%)	Yield rate	Reactor	Ref.
Cu_2O	N_2	100 mW cm^{-2}, 0.1 M KOH	20	7.2 μg cm^{-2} h^{-1}	An undivided three-electrode system equipped with a 300 W Xe lamp, an IR (water) filter	254
$CoCu/TiO_2/Sb_2Se_3$	NO_3^-	100 mW cm^{-2}, 0.1 M KNO_3 and 10 mM H_2SO_4	88.01	15.91 μmol h^{-1} cm^{-2}	A standard three-electrode configuration in an air-tight H-cell	37
TiO_x-250/CdS/CZTS	NO_3^-	100 mW cm^{-2}, 0.1 M KNO_3 and 10 mM H_2SO_4	89.1	8.21 μmol h^{-1} cm^{-2}	A standard three-electrode configuration in an air-tight H-cell.	255
O_SiNW/Au	NO_3^-	100 mW cm^{-2}, 0.5 M K_2SO_4 with 10 mM KNO_3	95.6	7.8 μg cm^{-2} h^{-1}	A potentiostat in a gas-sealed, undivided, three-electrode cell	256
BP	N_2	100 mW cm^{-2}, 0.1 M HCl which was purged with high purity N_2 (99.999%)	23.3	102.4 μg h^{-1} $mg_{cat.}^{-1}$	A sealed H-type two-compartment silica glass cell separated by a 25.4 μm thick Nafion 211 membrane	257
Au-PTFE/TS	N_2	100 mW cm^{-2}, 0.05 M aqueous H_2SO_4 with 0.05 M Na_2SO_3	37.8	18.9 μg cm^{-2} h^{-1}	A three-electrode sealed cell	250
Si photocathode with Li ions	N_2	400 mW cm^{-2}, 0.2 M $LiBF_4$ in 99 vol% THF and 1 vol% EtOH	95	52.4 μg cm^{-2} h^{-1}	A customized 3-electrode single compartment polyether ether ketone cell	258
$PdCu/TiO_2$/Si with Li ions	N_2	100 mW·cm^{-2}, 1 M $LiClO_4$ of propylene carbonate mixed with proton sources	46.15	43.09 μg cm^{-2} h^{-1}	A conventional three-electrode configuration	36
$Cs_{0.05}(FA_{0.83}MA_{0.17})_{0.95}$-$Pb(Br_{0.17}I_{0.83})_3$ coupled with glycerol oxidation	NO_3^-	100 mW cm^{-2}, 1.0 M KOH with various KNO_3 concentrations	99.5 ± 0.8	1744.9 ± 20.6 μg cm^{-2} h^{-1}	A half-cell reactor with a conventional three-electrode system	259
n^+np^+-Si photocathode with Au/PCN	N_2	100 mW cm^{-2}, N_2-saturated 0.05 M H_2SO_4	61.8	13.8 μg h^{-1} cm^{-2}	A standard air-tight H-shaped quartz reactor	253

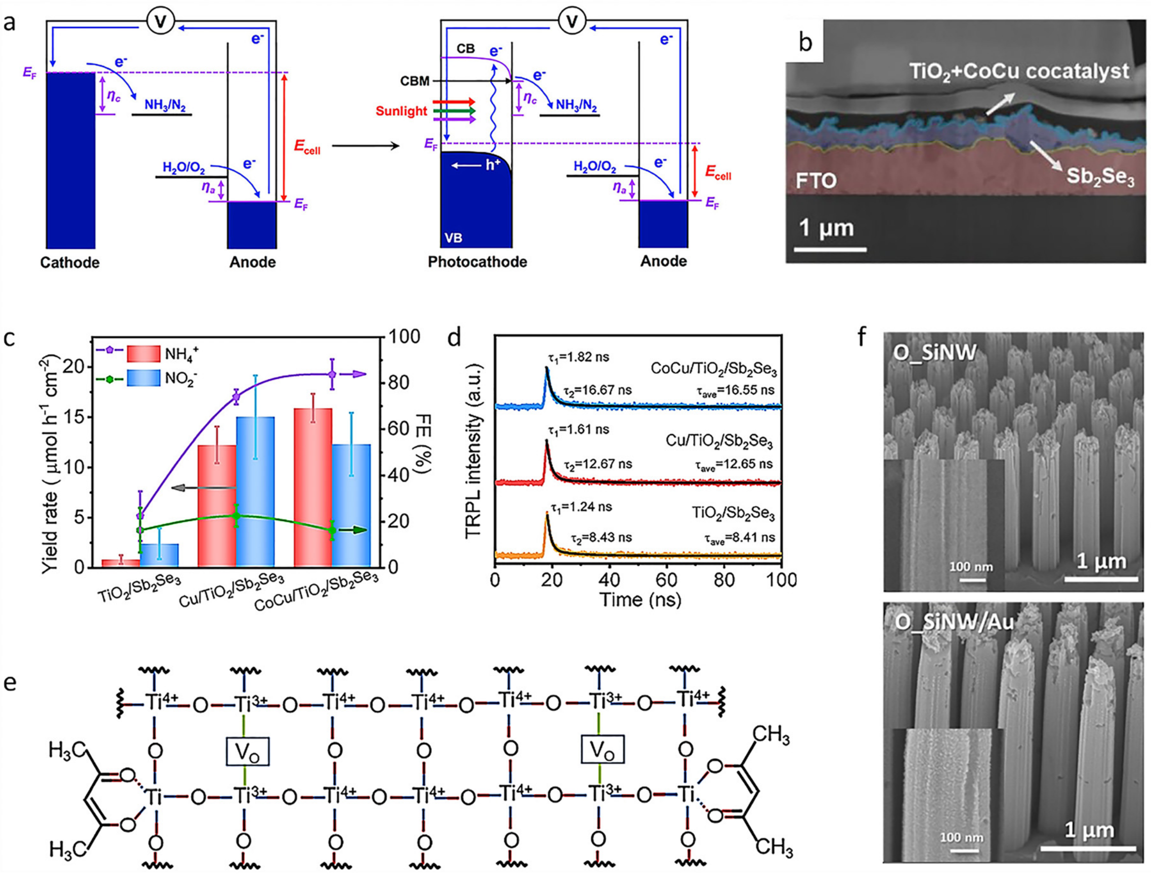

Fig. 8 (a) Schematic illustration of electrochemical and PEC NRR. (b) SEM image of CoCu/TiO_2/Sb_2Se_3. (c) PEC NH_3 performance of different catalysts. (d) Time-resolved photoluminescence decay spectroscopy of different samples. (e) Schematic illustration of TiO_x with different vacancies. (f) SEM images of O_SiNW and O_SiNW/Au. Reproduced with permission from ref. 254 Copyright 2020, American Chemical Society. Ref. 37 Copyright 2024, Wiley-VCH. Ref. 255 Copyright 2022, Wiley-VCH. Ref. 256 Copyright 2022, Wiley-VCH.

loading a defect-engineered TiO_x cocatalyst on a CdS/CZTS photocathode *via* spray-coating. The TiO_x-250/CdS/CZTS achieved an 89.1% NH_3 FE at 0.1 V *vs.* RHE and the highest yield rate of 8.21 μmol h^{-1} cm^{-2} at −0.2 V *vs.* RHE.[255] This work implemented a defect engineering strategy on a kesterite-based photocathode that effectively enhanced the adsorption of the reactant NO_3^- and $*NO_2$ intermediate, while a full surface coverage of TiO_x strongly suppressed the generation of the by-product NO_2^-, thus boosting PEC NH_3 production efficiency (Fig. 8(e)). In addition, photoelectrodes with efficient mass transfer are also expected to break the performance bottleneck. For instance, an ordered silicon nanowire array photocathode (O_SiNW) modified with Au NPs (O_SiNW/Au) was fabricated by a modified metal-assisted chemical etching method (Fig. 8(f)). The O_SiNW/Au array photocathode demonstrated a remarkable FE of 95.6% and a high production rate of 7.8 μg cm^{-2} h^{-1}.[256] Among them, the optical and electrochemical properties of the Si electrode were modified by constructing the O_SiNW array. The O_SiNW allowed for smoother mass transport and reduced charge recombination compared to planar or randomly grown Si electrodes, which exhibited an improved onset potential for the NO_3RR. Meanwhile, enabling the uniform distribution of Au NPs and facilitating mass transport during the reaction greatly improved the PEC performance for the NO_3RR. It is worth noting that compared with metal-based catalysts for NH_3 production, metal-free catalysts have great advantages in terms of environment and construction cost. For example, a black phosphorus (BP) photoelectrode was fabricated by the layer-by-layer assembly of BP nanosheets on an indium tin oxide (ITO) substrate, in which the BP nanosheets were synthesized by electrochemical exfoliation (Fig. 9(a)).[257] Without a sacrificial agent added, the PEC NRR activity in the N_2 saturated aqueous electrolyte was outstanding, with a high yield rate of 102.4 μg h^{-1} $mg_{cat.}^{-1}$, which displayed the highest performance among non-metal catalysts applied in photo- or electrocatalysis. Benefiting from the hydrogen-desorption-favorable surface of the BP photoelectrode as well as the synergistic effect from the coupling of a light-excitation-enhanced electrocatalytic process and an external-voltage-promoted photocatalytic process, the system above showed excellent PEC NH_3 activity (Fig. 9(b)).

The NH_3 synthesis processes mentioned above all occurred in aqueous solvents. As we all know, an aqueous reaction system is unfavorable under mild conditions, with a conversion efficiency of ∼10% or lower, mainly due to the poor selectivity for NH_3 and the strong competitive HER. Therefore, it is urgent to simultaneously satisfy the stringent requirements for gas N_2

diffusion, electron transport, and proton production. In this context, a unique aerophilic–hydrophilic Si-based heterostructure photocathode was designed for the conversion of N_2 to NH_3 in an acid electrolyte under mild conditions. The system containing a photo-absorber of Si, a gas-diffusion layer of poly(tetrafluoroethylene) (PTFE), and active sites of Au NPs displayed an excellent yield rate of $\sim$18.9 μg cm^{-2} h^{-1} and an FE of 37.8.[250] A functional aerophilic-hydrophilic heterostructure was constructed *via* the porous PTFE frameworks with highly dispersed Au NPs, which created a layer with enriched N_2 and controlled proton activity in an aqueous solvent, thus boosting NH_3 synthesis activity. Apart from aqueous electrolytes, lithium (Li)-containing non-aqueous electrolytes have also been used for enhancing the NH_3 yield. For example, a PEC Li-mediated NRR (Li-NRR) system composed of a p-type Si photocathode as the photoabsorber and Li ions as the reduction mediator reduced N_2 into NH_3 in non-aqueous tetrahydrofuran (THF) solvents with ethanol as the proton donor (Fig. 9(c)).[258] Thus, the as-synthesized photocathode resulted in a high NH_3 yield rate of 52.4 μg cm^{-2} h^{-1} and an excellent FE of 95% (Fig. 9(d)). The light illumination on the Si photocathodes improved the NH_3 yield dramatically because more photogenerated electrons from the light-excited Si photocathode induced the reduction of Li^+ ions into metallic Li. Based on this research idea, a Si-based photocathode with a hierarchical structure ($PdCu/TiO_2/Si$) was produced, achieving a record yield of 43.09 μg cm^{-2} h^{-1} and a remarkable FE of 46.15% under mixed gas conditions (0.12 MPa O_2 and 3.88 MPa N_2).[36] The $PdCu/TiO_2/Si$ photocathode facilitated the conversion process from the formation of Li_3N and hydrogenation to produce NH_3, to the release of Li^+ to restart a new PEC Li-NRR. At the same time, the PEC Li-NRR process was further enhanced by introducing a small amount of O_2 or CO_2 under pressure, which accelerated the decomposition of Li_3N. In addition to the development of non-aqueous reaction systems, the current NH_3 production process also faces a large additional bias due to the high thermodynamic potential for water oxidation (1.23 V). Moreover, inorganic-based photoelectrodes also have difficulties such as poor utilization of solar flux (wide bandgaps of 2.1–3.0 eV) and slow charge transport. Therefore, developing a new redox system for PEC NH_3 synthesis is particularly important. For example, a high-performance PEC system included NH_3 production and a glycerol oxidation reaction (Fig. 9(e) and (f)).[259] Among them, the perovskite-based material $Cs_{0.05}(FA_{0.83}MA_{0.17})_{0.95}Pb(Br_{0.17}I_{0.83})_3$ was used as the photocathode, and a Pt-loaded TiNS electrocatalyst (Pt@TiNS) was used for the

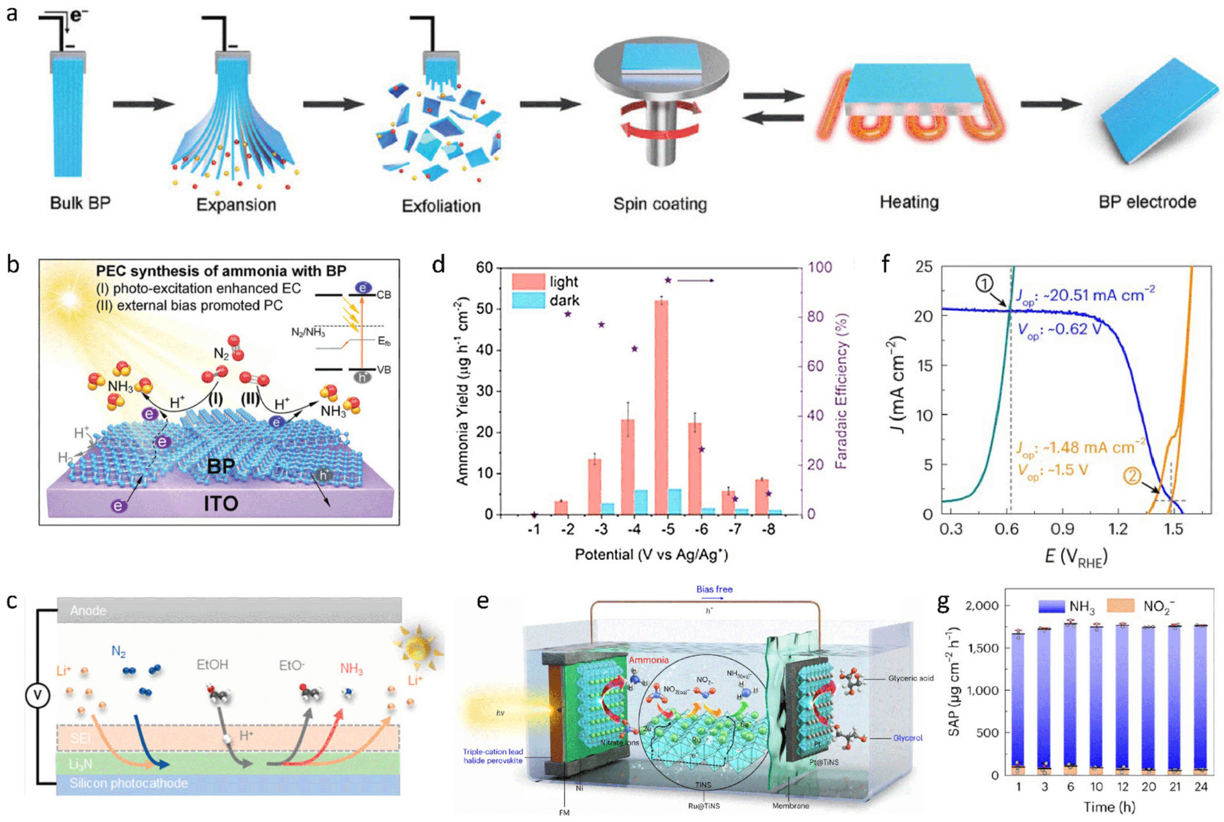

Fig. 9 (a) Schematic illustration of the exfoliation process of BP nanosheets and production of electrodes. (b) PEC performance enhancement mechanisms of the BP electrode. (c) Schematic illustration of an Li-mediated PEC NH_3 synthesis process. (d) PEC NH_3 yield rate under light and dark conditions. (e) Schematic illustration of cathodic NH_3 production combined an anodic glycerol oxidation system. (f) Polarization curves of cathodic NH_3 production combined an anodic glycerol oxidation system or a water oxidation system. (g) NH_3 yield rate along with the change of time. Reproduced with permission from ref. 257 Copyright 2020, Wiley-VCH. Ref. 258 Copyright 2023, American Chemical Society. Ref. 259 Copyright 2024, Springer Nature.

anode reaction. The perovskite-based photocathode combined with the glycerol oxidation anode showed a photocurrent density of 21.2 ± 0.7 mA cm^{-2} with an FE of 99.5 ± 0.8% for NH_3 production. Moreover, bias-free solar NH_3 production with a solar-to-NH_3 productivity of 1744.9 ± 20.6 μg cm^{-2} h^{-1} was achieved (Fig. 9(g)). Benefiting from a lower voltage for glycerol oxidation compared with water oxidation (Fig. 9(f)), while t he as-prepared catalysts had a relatively narrow bandgap and good charge transport properties, a high system efficiency and productivity were obtained.

After optimizing the catalysts, reaction environment, and system, the next step in developing green transformation technology is to focus on the reactor. Currently, PEC devices face challenges in synergistically managing optical, electrical, and catalytic properties. By using a cascade n^+np^+-Si photocathode that decouples light-harvesting and electrocatalysis, it was possible to improve light-harvesting, carrier separation and transport, and catalytic reactions. Impressively, at −0.10 V *vs.* RHE, an n^+np^+-Si photocathode integrated with Au/porous carbon nitride (Au/PCN) displayed remarkable PEC performance for NH_3 synthesis, with a high FE of 61.8% and a yield rate of 13.8 μg h^{-1} cm^{-2}. This was the best performance ever reported for the PEC NRR at such a low applied potential.[253] Specifically, the low-coupling photoelectronic system based on the Au/PCN with its porous structure improved light absorption, carrier transport, charge transfer, and catalytic activity. Meanwhile, the structural design of the integrated catalyst was favorable for adsorbing a high concentration of N_2, significantly promoting NH_3 synthesis.

6. Alkali metal mediated synthesis of ammonia

In the past few years, various catalysts and catalytic conversion technologies have been used to study green NH_3 synthesis. However, due to the competitive HER process in aqueous systems, only 1% of electrons are used to produce NH_3, leading to low catalytic performance.[188,260] Besides, even with benchmarking protocols to eliminate interference from contamination and reliably quantify the NH_3 produced, NH_3 synthesis in aqueous solutions faces various problems, such as low current density for synthesizing NH_3, FE, yield rate, and EE, and environmental pollution.[14,91,93,261–263] Based on these concerns, a series of research articles on aqueous electrocatalytic NH_3 synthesis found that NH_3 production was too low to determine if it came from N_2 reduction. Therefore, the feasibility of the electroreduction path for NH_3 synthesis in aqueous systems remains uncertain.[14] Furthermore, quantitative isotope and rigorous gas purification experiments have proven that the Li-NRR method is a reliable way to synthesize NH_3 at room temperature.[91]

The history of the Li-NRR began in the 1930s with the electrochemical deposition of lithium, followed by nitridation and protolysis in alcohol-based electrolytes.[264] Within an autoclave-type electrolysis cell, an initial current of 0.5 A was applied to deposit lithium metal for 5.0 h. The Li was electrodeposited in an electrolyte of lithium chloride in ethanol. Although negligible NH_3 was measured at atmospheric pressure, the FE increased by up to 10% at a high-pressure of 1000 bar. The low NH_3 selectivity was thought to be due to the formation of a surface coating on the electrode.[265] The Li-NRR was then revisited in the 1990s. Researchers first reported using THF as the electrolyte solvent in the Li-NRR.[266,267] The experiments took place in a single-compartment autoclave cell where lithium metal was plated onto a copper electrode in a 0.2 M lithium perchlorate, 1% ethanol in THF electrolyte. The process used 50 bar of N_2 gas to produce NH_3 with an FE of 48.7%. Further screening of working-electrode metals, lithium salts, and proton-donor additives led to an NH_3 FE of 59.8% under optimized experimental conditions. To further optimize the Li-NRR technology, researchers developed a three-step strategy of separate electrolysis, nitridation, and protonation, which achieved an NH_3 FE of 88.5%.[268] In this process, LiOH was first electrolyzed at 450 °C, and then the molten salt was exposed to N_2 gas at temperatures up to 100 °C. The lithium nitride then reacted exothermically with water to produce NH_3. Unlike a continuous process, batch processes require extra separation and purification steps and a large Li source, which can increase system cost and complexity. Therefore, compared to NH_3 synthesis in aqueous systems and under traditional reaction conditions, the single-process electrochemical Li-NRR under ambient conditions has been shown to be commercially promising.[269] Specifically, Li metal can dissociate N_2 under ambient conditions, and its high enthalpy of hydration and small nucleus make it the strongest reducing agent of all metals (−3.04 V *vs.* SHE).[270] Electrodeposition of Li metal occurs in non-aqueous and aprotic electrolytes, which are thermodynamically unstable with Li metal but kinetically stable because of a surface passivation layer.[271] This surface film called the solid–electrolyte interphase (SEI) reduces further reactions between the metallic Li and the electrolyte. The Li-NRR is a unique technique because N_2 reduction and protonation depend on and occur within the SEI layer, which is essential for mediating the catalysis process. In this system, the electrochemical deposition of metallic Li with N_2 gas forms lithium nitride, which then reacts with available protons to produce NH_3.[269] Thus, Li is capable of producing NH_3 at ambient pressure because it has a low work function and high reactivity.

Therefore, Li can break the strong $N\equiv N$ bonds and fix N_2 as Li_3N, which is then converted into NH_3. Furthermore, the disruption of water molecules by Li^+ ions slows water splitting.[272] The Li-NRR reaction process involves the reduction of Li^+ ions to metallic Li at the working electrode,[273] where the Li metal reacts with N_2 to produce Li_3N. This Li_3N is then protonated with a source like alcohol to form NH_3.[263] In this process, freshly plated Li, produced by electroreducing Li^+ ions in the electrolyte, is believed to dissociate N_2; the surface N is then reduced through a series of electron and proton transfers to form NH_3. In the Li-NRR system, the decomposition of organic electrolytes during Li deposition on the cathode forms a significant part of the SEI layer, which is an ionically conductive, porous passivation layer on the electrode surface. However, its exact composition and mechanistic role in the Li-NRR remain unclear, since it is sensitive to air. Even so, this technology typically achieves an FE between 5% and 20%,[91,274] with a recent breakthrough reaching 69% (20 bar N_2).[275] To optimize the three-phase interface reaction rate, the Li-NRR process recently used a gas diffusion electrode (GDE) configuration, which showed an excellent FE of 35%. However, the updated system only operated stably for a few minutes and had a high potential.[98] A potential cycling method recently reduced this instability.[276] As a result, the FE increased from 20% to 37% with cycling at an EE of 7% over several days. Nevertheless, the Renewable Energy to Fuels Through Utilization of Energy-Dense Liquids (REFUEL) program of the US Department of Energy set the following performance targets for the commercialization of NH_3 synthesis: a NH_3 yield rate of 10^{-6} mol s^{-1} cm^{-2}, an FE of 90% at a current density of 300 mA cm^{-2}, and durable catalyst stability, with catalytic efficiency decreasing by no more than 0.3% after 1000 hours of electrolysis.[277] The Li-NRR is far from this goal. A major problem in Li-NRR technology is currently the EE, since Li plating generally requires a negative potential (−3.04 V *vs.* SHE). Assuming an FE of 80% and minimizing all overpotentials at the anode by using another anode reaction like the hydrogen oxidation reaction (HOR), the EE would increase to 26%. To address this, small amounts of O_2 were added to the feed gas to improve the FE and stability of the Li-NRR process (Fig. 10(a)).[274] A high FE of 78.0 ± 1.3% can be achieved by mixing in a certain amount of O_2, which results in an EE of 11.7 ± 0.5%. The addition of O_2 can modify Li^+ diffusion through the SEI layer while maintaining the optimal concentration of protons and N_2 at the surface, thereby influencing the deposition behavior and the stability of the deposited layers. More importantly, this research offers substantial advantages for the scale-up of synthetic NH_3 processes, as the Li-NRR does not require ultra-pure N_2.

To further optimize the activity of the Li-NRR, exploring its fundamental mechanism has become key. Recently, relevant studies were performed for the first time to analyze the entire process of the Li-NRR reaction using cryo-electron microscopy (Fig. 10(b)). The proton donor, ethanol, is the main driving force of the Li-NRR. In the absence of a proton donor, the decomposition products of the fluoroborate ion and tetrahydrofuran form a passivated SEI. N_2 and the electrolyte cannot react with Li because they cannot penetrate and pass through the SEI. At the same time, Li ions can diffuse into the SEI, resulting in the continuous formation of metallic Li dendrites, which is not conducive to the subsequent reaction. With the addition of ethanol, the amorphous SEI becomes dominated by ethanol decomposition products, and N_2 and the electrolyte can penetrate the interface, thereby continuously consuming the deposited Li metal to form NH_3 gas and driving the reaction forward. Therefore, for the Li-NRR, an SEI with poor passivation effectively enhances NH_3 synthesis, so it is necessary to

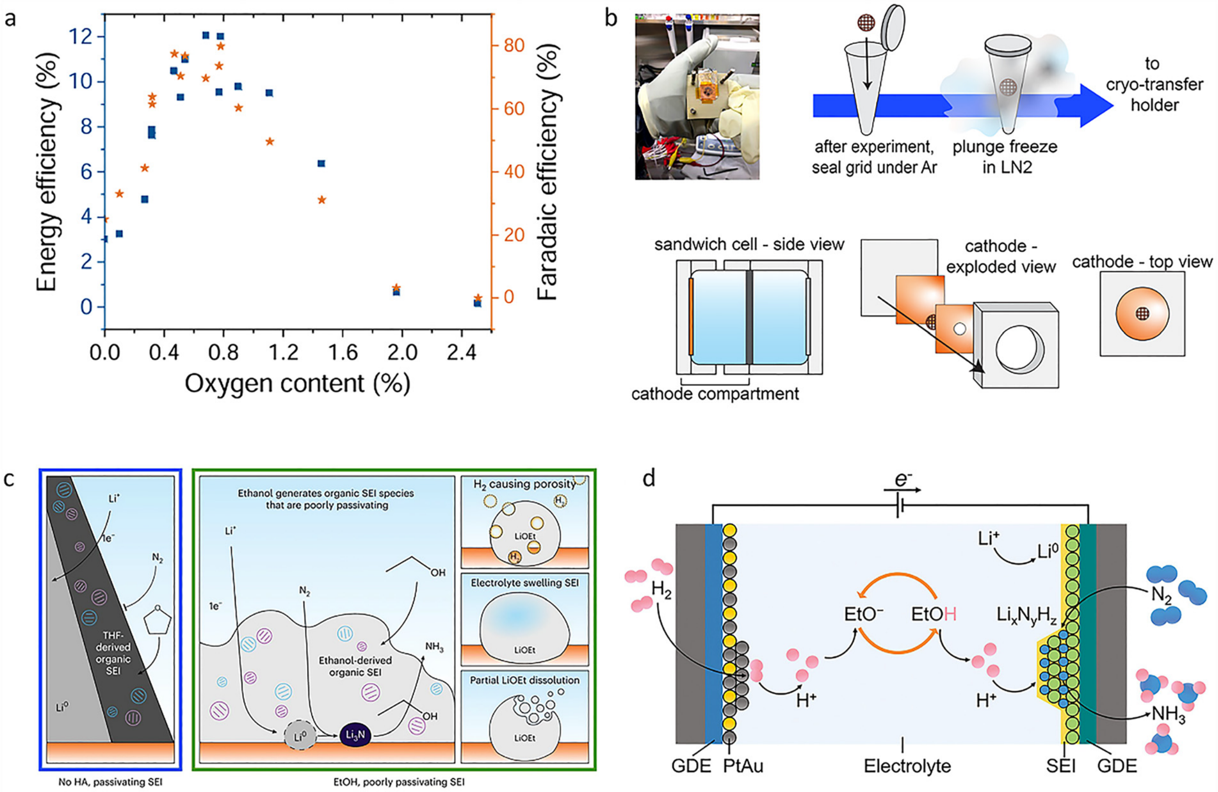

Fig. 10 (a) Diagram of the change of FE and EE with oxygen content. (b) The picture and diagram of cryo-electron microscopy. (c) Schematic illustration of the Li-NRR mechanism. (d) Schematic process of the Li-NRR combined with the HOR process. Reproduced with permission from ref. 274 Copyright 2021, American Association for the Advancement of Science. Ref. 278 Copyright 2023, Springer Nature. Ref. 280 Copyright 2023, American Association for the Advancement of Science.

introduce proton donors to promote the reaction (Fig. 10(c)). However, if there is an excessive reaction between the Li metal and the proton donor, a large amount of hydrogen gas will be generated, resulting in an irreversible loss of Li metal. Therefore, in the subsequent design and improvement of the reaction, it is necessary not only to select a suitable combination of lithium salt and solvent but also a highly stable proton donor to achieve SEI activation while avoiding the loss of Li metal and improving reaction safety and production efficiency.[278]

Further understanding of the Li-NRR mechanism is also expected through innovations in the components of the reaction system. In this regard, a reference electrode ($LiFePO_4$) was prepared for measuring potentials and estimating sources of EE loss. Specifically, it contained $LiFePO_4$ discs and a negative electrode of Li metal separated by 1.0 M lithium bis(trifluoromethylsulfonyl)imide wetted glass fiber. After an eight-millimeter hole was punched in the center of the $LiFePO_4$ disc, a sandwich cell was assembled. A phase of fast (de)intercalation of Li ions characterizes $LiFePO_4$ after partial lithiation. It also possessed low polarizability, and its redox equilibrium potential tended to remain stable relative to Li metal for a long time, which could reveal the relationship between partial current density and potential. The $LiFePO_4/Li^+$ equilibrium was also used as a tool to detect changes in Li ion activity *in situ*. This study is expected to move the field toward a more definitive system to fully understand the Li-NRR process.[279]

Typically, most Li-NRR reports have used sacrificial solvents as proton sources. However, to be feasible in real production, protons must come from hydrogen (or water). Recently, the hydrogen oxidation reaction (HOR) was proposed as an anode reaction for Li-NRR systems to provide a sustainable hydrogen source (Fig. 10(d)).[280] The PtAu alloy catalyst greatly reduced the anode potential and avoided the oxidation of the solvent. Under normal temperature and pressure conditions, an FE of 61% and an EE of 13% were achieved for NH_3 production, and an NH_3 FE of nearly 100% was achieved in intermittent reactors with 15 bar or 20 bar pressures, at a high current density of 1.0 A cm^{-2}. Specifically, Li^+ ions diffused from the bulk electrolyte through the SEI to the cathode electrode surface for electroreduction to Li metal, which then reacted with N_2 to form Li_3N species. The Li_3N species were further protonated by a proton shuttle agent to continuously produce NH_3. The Li-NRR combined with anode hydrogen oxidation could effectively avoid using a sacrificial organic solvent as a proton source *via* the recyclability of the ethanol proton shuttle, while further decreasing the cell voltage.

The proton shuttle has a decisive effect on the performance of Li-NRR systems because it changes the properties of the SEI. Therefore, based on the studies above, screening proton shuttles in the Li-NRR coupled with the HOR system is expected to further improve the performance of the Li-NRR (Fig. 11(a)). To address this challenge, proton shuttle screening experiments were performed in a continuous-flow reactor in the presence of the HOR at the anode. After passing a charge of 700 C, phenol (PhOH) achieved the highest NH_3 FE of 72 ± 3% and an EE of 15 ± 1% at ambient pressure and temperature, which exceeds the state-of-the-art ethanol (Fig. 11(b)).[281] Specifically, the deprotonated form (PhO^-) of the PhOH was proven to be the primary species responsible for transferring protons during the Li-NRR process (Fig. 11(c)). Moreover, theoretical mass transport modeling clarified the dependence of the Li-NRR performance on the acid dissociation constant and diffusion coefficient of the proton shuttles.[281] This discovery provides a comprehensive framework for rational design principles for efficient proton shuttles in the Li-mediated electrosynthesis of NH_3. Following this pioneering work, the performance of different Li salts was compared in a specific reactor (Fig. 11(d)–(g)). $LiBF_4$ achieved the highest FE of 95% and an NH_3 yield rate of 2.5 μmol s^{-1} cm^{-2} (Fig. 11(h)–(i)). The excellent performance can be ascribed to the formation of a uniform SEI on the electrode.[282] At the same time, related work reported a Li-NRR system with almost 100% current-to-NH_3 efficiency, enabled by a compact ionic layering generated by $LiNTf_2$ at the interface, although at an elevated pressure of 15 bar.[283] Besides the proton donor, Li salts have also received massive attention from the community due to their great impact on the performance of the Li-NRR.[284]

As we all know, the electrolyte solution for NH_3 synthesis *via* the Li-NRR mainly includes the main electrolyte, such as THF, the proton shuttle, and a Li salt. Numerous experimental results show that all these factors will affect the performance of the reaction system.[284] Therefore, in addition to the development of proton shuttles and Li salts, improving the other components of the electrolyte is also important. Recently, a series of solvents, including 2-methyltetrahydrofuran (2-MeTHF), tetrahydropyran (THP), dimethoxyethane (DME), diglyme (DG), and tetraethylene glycol dimethyl ether (TEGDME), were studied systematically in the Li-NRR process (Fig. 12(a)). The assessments of solvent candidates are based on their conductivity, parasitic reactions, product distribution, and FE. Meanwhile, promising candidates should have the following characteristics such as good solubility for lithium salts, the ability to provide sufficient conductivity, reliable stability to endure reactive metallic Li at the cathode and the oxidation potential at the anode, and the capability to induce a favorable SEI layer for N_2 reduction. These characteristics directly dictate the performance of the Li-NRR, such as the NH_3 yield rate, FE, EE, and stability. Specifically, compared with cyclic ether-based electrolytes, the SEI in linear ether-based electrolytes has a higher proportion of inorganics and heavier organics, giving it a better ability to resist ethanol corrosion and thus trapping more NH_3 in deposits. Notably, an impressive NH_3 FE of 58.5 ± 6.1% was obtained in the THF-based electrolyte (0.11 M ethanol), while a decent FE of 30.0 ± 4.2% was achieved in the DME-based electrolyte (0.11 M ethanol), but at a significantly lower overpotential compared with THF, verifying its potential in the Li-NRR.[284]

Based on the explorations above, including the introduction of the HOR on the anode, screening proton shuttles and suitable solvents can make the Li-NRR more sustainable. However, it is worth noting that the problems of solvent polymerization and the volatility of THF in the Li-NRR process make it difficult to achieve long-term operation and mass production. At the same time, to ensure excellent ionic conductivity and smooth plating of Li, the solvent must allow for noticeable

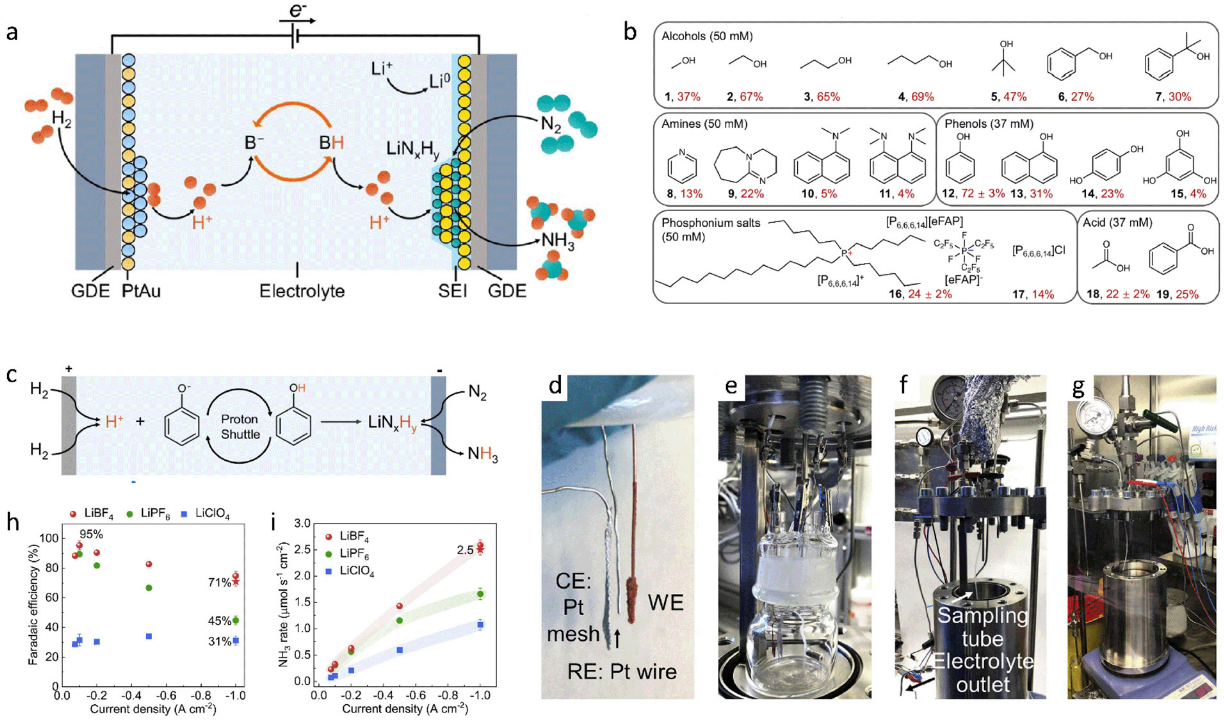

Fig. 11 (a) Schematic illustration of the proton-shuttling process for the Li-NRR. (b) NH_3 FE for different proton shuttles. (c) Schematic illustration of the phenol shuttling process for the Li-NRR. (d)–(g) Digital photos of the Li-NRR pressure reactor. (h) NH_3 FE of different Li salts. (i) NH_3 yield rate of different Li salts. Reproduced with permission from ref. 281 Copyright 2024, Springer Nature. Ref. 282 Copyright 2022, Cell Press.

solubility of the Li salts. In addition to being compatible with metallic Li to produce an SEI layer, it also needs to be matched with proton shuttles to facilitate the delivery of protons. Therefore, based on the research above on chain-ether-based solvents, recently, the ring-ether-based solvent THF was also replaced by the chain-ether-based solvent diethylene glycol dimethyl ether (DG) to achieve long-term continuous electrosynthesis of NH_3 (Fig. 12(b)).[285] The DG solvent did not polymerize easily under reaction conditions, has a high boiling point (162 °C *vs.* 66 °C for THF), and formed a dense and uniform SEI layer (Fig. 12(c) and (d)), thus boosting the release of NH_3 and ensuring electrolyte stability. Specifically, the Li-NRR system with the DG solvent achieved 300 hours of continuous operation in a flow electrolyzer with a 25 cm^2 electrode at 1.0 bar pressure and mild conditions, displaying an NH_3 FE of 64 ± 1% (Fig. 12(e)). These results strongly indicate that long-term, stable, continuous NH_3 electrosynthesis *via* the Li-NRR can be achieved by using more stable chain-ether-based solvents. To further solve the problems in the industrial application of the Li-NRR, for example, developing high-current-density processes requires the study of more suitable GDE configurations. Therefore, future research on the Li-NRR should focus on achieving remarkable FE and EE at industrial current densities while maintaining long-term stability.

As of now, Li-NRR systems face numerous challenges, such as high input voltage, the volatilization of toxic organic solvents, gas–liquid mass transfer limitations, and ambiguity in the fundamental mechanism.[263] The following perspectives are proposed based on these challenges: (1) metals with a lower deposition potential should be used to replace Li metal or be alloyed with Li metal to reduce the power consumption of the metal-mediated NH_3 synthesis system, and the ability of the deposited metal to activate N_2 should also be tested and verified. (2) Many liquid electrolytes from the field of Li-ion batteries are expected to be alternative solvents for Li-NRR systems, such as 1,2-dimethoxypropane, dimethoxymethane, propylene carbonate, ethylene carbonate, dimethyl carbonate, diethyl carbonate, and ethyl methyl carbonate. (3) To eliminate mass transfer limitations and the high internal resistance of the reactor, the Li-NRR system can be run in a flow cell, a slim flow cell, or a membrane electrode assembly (MEA) reactor. The GDE configuration will be able to directly transport the gaseous reactants to the catalytic interface, and the zero-gap characteristics can greatly eliminate the high internal resistance caused by the distance between the traditional working electrode and the reference electrode, finally helping the Li-NRR technology move toward practical applications. (4) The development and use of new *in situ*/*operando* technologies, such as electrochemical quartz crystal microbalance with dissipation monitoring, X-ray diffraction, X-ray absorption fine structure, Raman spectroscopy, and transmission electron microscopy, coupled with artificial intelligence and advanced *ab initio* molecular dynamics for real-time detection and simulation of the entire reaction process, will help determine the emergence and transformation of key reaction intermediates and monitor key components such as the SEI layer, ultimately leading to an understanding of the internal mechanism.

Based on the outlook above for the future of the Li-NRR, metals other than Li remain to be explored for potential advantages in terms of EE, reaction speed, stability, reactor design, and cost. Recently, a calcium salt, $Ca[B(hfip)_4]_2$, was synthesized by the reaction of $Ca(BH_4)_2$ with hexafluoroisopropanol. $Ca[B(hfip)_4]_2$ dissolved in THF functioned as an electrolyte, and ethanol was used as a proton shuttle agent (Fig. 12(f)). The Ca-NRR process was successfully performed in a continuous-flow electrolytic cell. At normal temperature and pressure, $Ca[B(hfip)_4]_2$ achieved an NH_3 FE of 40 ± 2% (Fig. 12(g)). The dissociation energy barrier of N_2 on the surface of metallic Ca was relatively low, which indicated that the dissociation rate of N_2 on the surface of Ca was very fast at normal temperature and pressure. Compared to Li metal, Ca is a promising alternative. This result opened the door to using metals with high abundance for the mediated synthesis of NH_3, such as Mg, Ba, Sr, and Na, which could be used, thus allowing for the selection of efficient, highly selective, stable, cost-effective, and scalable NH_3 synthesis technologies.[286]

In addition to optimizing various parameters and the mediating metals in Li-NRR technology, a significant increase in yield rates per geometric surface area is required to make the metal-mediated NH_3 production strategy competitive for large-scale applications. For example, a high-surface-area Cu electrode was synthesized using a hydrogen bubble templating method on a Ni foam substrate (HBTCu). At a high current density (100 mA cm_{geo}^{-2}) and 20 bar N_2, the developed HBTCu catalyst achieved an NH_3 yield rate of 46.0 ± 6.8 nmol s^{-1} cm_{geo}^{-2}, which was 50 times higher than that of a flat copper foil. The high current density was attributed to the use of a high-specific-surface-area substrate.[287]

7. Design criteria for green ammonia synthesis catalysts

7.1 Photocatalytic ammonia synthesis

The low efficiency of photocatalytic ammonia synthesis is caused by several factors: (1) it is difficult to balance light absorption and charge separation. For instance, narrow-bandgap semiconductors like CdS (2.4 eV) can absorb visible light, but their charge recombination rate is high (over 80%).

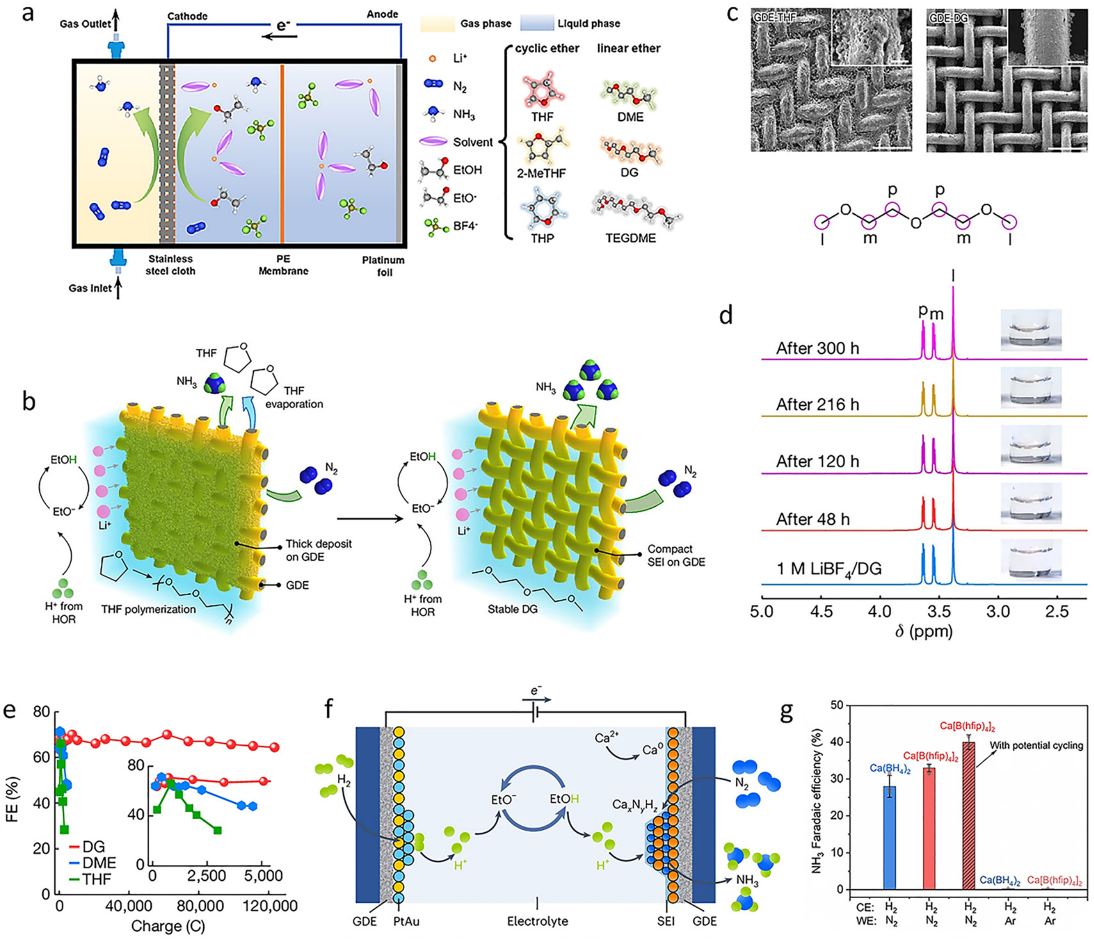

Fig. 12 (a) Schematic illustration of the gas diffusion cell with different solvents. (b) NH_3 synthesis system with ring-ether-based and chain-ether-based solvents. (c) SEM images of the GDE after long-time NH_3 production using THF and DG solvents. (d) NMR spectra of the DG-based Li-NRR system. (e) NH_3 FE of different solvent-based Li-NRR systems. (f) Schematic illustration of the Ca-mediated NH_3 synthesis process. (g) NH_3 FE of the Ca-mediated NH_3 synthesis system with different Ca salts. Reproduced with permission from ref. 284 Copyright 2023, American Chemical Society. Ref. 285 Copyright 2024, Springer Nature. Ref. 286 Copyright 2024, Springer Nature.

Wide-bandgap materials such as TiO_2 (3.2 eV) have good charge separation but only respond to ultraviolet light. These problems lead to the photogenerated electron–hole pair lifetime of the photocatalyst being much shorter than the time required for N_2 reduction. (2) N_2 activation and proton transfer kinetics are limited. High-energy electrons are needed to break the $N\equiv N$ bonds, while the reduction potential of photogenerated electrons is limited. The low solubility of N_2 in aqueous solutions leads to a low N_2 coverage rate on the catalyst surface. At the same time, the high proton concentration in acidic media easily triggers the hydrogen evolution reaction, which involves a $2e^-$ transfer with relatively fast reaction kinetics, while the proton transfer rate is low in neutral or alkaline media. (3) Photocatalysts can suffer from photocorrosion and chemical dissolution. The strong oxidizing property of photogenerated holes leads to the self-decomposition of the catalysts. For instance, metal sulfides like CdS and MoS_2 are oxidized to SO_4^{2-} by holes, and the active metal centers of single-atom catalysts can dissolve in acidic environments. Therefore, to achieve highly active photocatalytic ammonia synthesis, the design of photocatalysts should consider the following aspects: (i) select narrow-bandgap semiconductors to ensure a response to visible light (400–700 nm) and even near-infrared light (over 700 nm), such as metal oxides like $BiVO_4$ and nitrates like g-C_3N_4. On this basis, nanoparticles of precious metals like Au and Ag can be introduced to enhance light capture. Constructing heterostructured photocatalysts, such as Z-type and S-type, promotes efficient charge separation and transport while retaining strong reducing electrons and strong oxidizing holes. In addition, a co-catalyst can be introduced as an electron trap to accelerate the transfer of electrons to the N_2 molecules. (ii) Design catalysts with single atoms of transition metals to promote the breaking of $N\equiv N$ bonds. N_2 adsorption can also be enhanced by introducing oxygen or sulfur vacancies and nitrophilic groups. Introducing hydrophobic functional groups at the catalyst interface can inhibit the competitive hydrogen evolution reaction. (iii) Extending the stability of photocatalysts enhances their photocatalytic efficiency. Strategic stabilization approaches focus on the following modifications: depositing an epitaxial protective layer to physically isolate the active sites and precisely engineering the coordination environment of the metal centers to thermodynamically disfavor dissolution. The protective layers typically exhibit critical characteristics: chemical inertness against hole oxidation, high transparency to maintain light penetration, and controlled porosity to permit reactant diffusion while blocking oxidative species. Concurrently, modifying the primary coordination sphere of the active metal sites through nitrogen or phosphorus coordination or strain engineering alters the electronic structure.

7.2 Electrocatalytic ammonia synthesis

The design of high-performance electrocatalysts for ammonia synthesis requires a clear understanding of the key challenges in this process. First, N_2 has a low HOMO energy level and a high LUMO energy level, making electron injection difficult and resulting in the high stability of the $N\equiv N$ bond. Second, N_2 and protons (H^+) compete for adsorption sites on the catalyst surface; the overlapping potential windows required for electrocatalytic ammonia synthesis and the hydrogen evolution reaction (HER) result in the dominance of the kinetically easier HER. Taking N_2 as an example, its relatively low solubility in the aqueous phase, combined with mass transfer resistance at the gas–liquid–solid three-phase interface, results in an insufficient local reactant concentration. In summary, the design of electrocatalysts for ammonia synthesis should consider the following aspects: (1) nanostructure engineering: strategies such as constructing two-dimensional nanosheets, interface defect engineering, and designing porous structures can significantly increase the number of active sites in the catalyst while accelerating reactant mass transfer through three-dimensional porous active interfaces. Furthermore, introducing a second metal or a non-metal (*e.g.*, B, P, and S) can alter the charge distribution of the catalyst. By regulating the electronic structure of the catalyst or using synergistic effects between different sites, rapid adsorption and activation of reactants at active sites can be achieved, providing the necessary protons and electrons for the reaction and promoting ammonia synthesis. (2) Support engineering: introducing carbon-based supports, metal oxide/chalcogenide supports, and organic framework supports can enhance the catalyst's conductivity. Meanwhile, the d-band center of the metal sites can be modulated by regulating metal-support interactions to optimize N_2 adsorption strength. Besides, N, O, or S sites or vacancies on the support surface can anchor highly dispersed active metal atoms (*e.g.*, Fe, Mo, and Ru), improving active site utilization while preventing agglomeration and enabling rapid reactant conversion. (3) Interface engineering: hydrophobic modification of the catalyst surface can regulate proton adsorption strength and suppress the competing HER. Additionally, modifying the electrode surface with nitrophilic groups can increase the concentration of reactants for ammonia synthesis.

7.3 Photoelectrocatalytic ammonia synthesis

Photoelectrocatalytic ammonia synthesis includes the following specific steps: (i) the absorption of light and the excitation of charge carriers; (ii) the separation and transport of photoexcited carriers to the surface of the photoelectrode; and (iii) reduction reactions on the catalyst's surface. Hence, designing and constructing photoelectrode materials with broad solar spectral absorption, fast charge carrier generation and separation, and a large and effective catalytically active surface, while also adsorbing enough N_2 molecules, is crucial for achieving a high-efficiency photoelectrocatalytic ammonia synthesis process, especially at low overpotentials. Based on the discussion above, the design of catalysts typically proceeds from two key perspectives: (1) from a photochemical standpoint, catalysts must exhibit high efficiency in photogenerated charge carrier excitation and rapid electron–hole separation. To address the challenges of carrier generation and electron–hole recombination, band structure and electronic structure modulation have proven to be effective approaches. Specifically, band structure engineering involves combining semiconductor materials with different band structures (such as TiO_2/CdS and $BiVO_4$/Cu_2O systems) to form type-II heterojunctions, Schottky junctions, and other configurations. These heterostructures effectively promote the separation of photogenerated electrons and holes, thereby enhancing charge carrier utilization and photocatalytic efficiency. Among them, type-II heterojunctions drive the spatial separation of electrons and holes through built-in electric fields, while Schottky junctions optimize carrier migration and separation processes through band alignment between two semiconductor materials. Besides, electronic structure modulation can be divided into non-metal doping and metal doping. Non-metal doping (*e.g.*, N or S doping in TiO_2) enables directional charge transfer and adjusts the catalyst's Fermi level, while metal doping (*e.g.*, Bi doping in Cu_2O) introduces intermediate energy levels; both approaches enhance the visible light response. (2) From an electrochemical perspective, catalysts must possess appropriate adsorption and desorption kinetics for reactants and intermediates to improve electrocatalytic activity and selectivity. Therefore, active site design and surface structure engineering represent two effective strategies. Specifically, active site design generally includes defect engineering and atomic site optimization. Defect engineering involves creating oxygen vacancies and metal vacancies, where oxygen vacancies provide electron-rich regions to promote N_2 adsorption and activation, and exposed unsaturated metal sites enhance N_2 binding energy. Atomic site optimization strategies include both single-atom and dual-atom site designs. Well-defined single-atom coordination environments increase active site utilization and ammonia selectivity, while dual-atom sites can cooperatively adsorb and activate N_2, reducing the energy barrier of the rate-determining step. Furthermore, surface structure design includes morphology control and crystal lattice engineering. Morphology control exposes more active sites and increases the electrochemical active surface area to enhance the mass transport of reactants and intermediates, accelerating their conversion. Crystal lattice engineering effectively improves electron transport, and well-defined lattice structures can enhance selectivity for the target product.

7.4 Alkali metal mediated ammonia synthesis

In non-aqueous lithium-mediated ammonia synthesis systems, the reaction proceeds through three key steps: (1) the electrochemical reduction of Li^+ to metallic Li ($Li^+ + e^- \rightarrow Li^0$) at the working electrode, (2) the chemical reaction between Li^0 and N_2 to form lithium nitride ($6Li + N_2 \rightarrow 2Li_3N$), and (3) the protonation of Li_3N to generate ammonia ($Li_3N + 3H^+ \rightarrow 3Li^+ + NH_3$). A critical component of this process is the solid–electrolyte interphase (SEI) layer formed through electrolyte decomposition during Li deposition. This ionically conductive yet electronically insulating porous layer has selective permeability; excessive passivation can hinder N_2 and electrolyte penetration, preventing essential reactions with metallic Li. Based on this reaction mechanism, current research mainly focuses on key components in non-aqueous systems, such as organic electrolyte formulation, lithium salt selection, proton source design, proton shuttle agents, and metals with lower deposition potentials. Therefore, while most reported systems use cost-effective stainless-steel cloth electrodes, advanced electrode designs should include 3D nanostructured architectures to enhance the specific surface area, optimize Li^+ diffusion pathways, and provide confined spaces for homogeneous Li deposition. These designs should also incorporate nucleation modifiers, such as Ag nanoparticles, to reduce the Li nucleation overpotential, guide uniform Li plating and stripping, and maintain SEI layer stability during cycling.

These design strategies aim to simultaneously address three critical challenges: (i) improving N_2 accessibility to active Li sites, (ii) preventing dendrite formation, and (iii) maintaining stable SEI properties during prolonged operation, which are key requirements for scaling green ammonia synthesis technology.

7.5 N_2 for ammonia synthesis

The activation and conversion of N_2 molecules is the central challenge in this reaction. Catalyst design must focus on the efficient dissociation or protonation of the $N\equiv N$ triple bonds. Specifically, the catalyst should have: (i) high-efficiency N_2 activation by providing electrons to populate N_2's antibonding pi orbitals, typically achieved using transition metals like Fe, Ru, and Mo; (ii) three-dimensional porous nanostructures to increase N_2 adsorption sites and reactant concentration at the catalytic interface; (iii) the ability to suppress the competing hydrogen evolution reaction through the selection of catalysts with weak H* adsorption. Furthermore, metal-nonmetal or bimetallic site catalysts can be designed to modify the atomic coordination environment of the metal centers and increase electron localization. Introducing electron-deficient nonmetal sites can polarize N_2 molecules, which synergistically promotes N_2 activation and the following hydrogenation steps.

7.6 NO for ammonia synthesis

This reaction faces several challenges: (a) NO may be over-reduced to N_2O or N_2; (b) NO tends to strongly bind with metal centers, blocking active sites; (c) hydrogenation steps require precise control to avoid byproducts like NH_2OH. Therefore, catalyst design should focus on: (i) selecting appropriate metal sites and modulating supports to prevent excessive NO adsorption while weakening the $N{=}O$ bonds; (ii) designing dual metal sites (*e.g.*, metal–acid or metal–sulfur) to cooperatively promote reactant adsorption and hydrogenation and facilitate oxygen removal; (iii) using steric confinement effects (*e.g.*, metal organic framework micropores) to suppress N_2O formation; (iv) adding electronegative elements to regulate the d-orbital electrons of metal atoms, preventing excessive NO hydrogenation.

7.7 NO_2^- and NO_3^- for ammonia synthesis

The reduction of NO_2^-/NO_3^- to ammonia faces several challenges: (a) complex proton-coupled electron transfer processes with various intermediates and products (*e.g.*, NO_2, NO_2^-, NO, N_2O, N_2, NH_3, NH_2OH, and N_2H_4) can lead to side reactions through kinetic competition, reducing ammonia selectivity; (b) high overpotentials are needed for NO_2^-/NO_3^- reduction, particularly at proton-coupled electron transfer steps, which increases energy consumption; (c) the hydrogenation pathways for NO_2^- strongly depend on pH, where NO is favored under acidic conditions and NH_3 under alkaline conditions. Thus, developing catalysts with both high activity and selectivity is crucial. Design strategies include: (i) creating efficient nitrogen source adsorption and activation sites; (ii) adding secondary metal components to form heterointerfaces with built-in electric fields that improve the metal's electronic structure and promote proton adsorption for selective ammonia production; (iii) creating multicomponent catalysts (*e.g.*, 5d noble metals) to increase surface H* coverage and improve ammonia selectivity and formation rates; (iv) developing non-precious metal catalysts (*e.g.*, Cu and Ni) with electron-deficient nonmetal sites (*e.g.*, B) to suppress hydrogen evolution. Notably, engineering the interfacial microenvironment, for example, through oxide coatings, –OH group functionalization, or restructuring the interfacial water network, can also increase ammonia production efficiency.

8. Reactors for synthesis of ammonia

8.1 Electrocatalytic ammonia synthesis reactors

In previous studies, mainstream research on NH_3 synthesis has mainly focused on designing catalysts and catalytic technology routes, rather than on innovating the engineering of the catalytic conversion device. Therefore, the development of electrocatalytic reactors has been slow. It is well known that reactors are critical to catalytic performance. Their design and development involve integrated knowledge from other disciplines, such as material forming and processing, the fluid mechanics of gas–liquid transfer, chemical processes, and analog simulation. Although great strides have been made in the field, major breakthroughs in basic research and practical applications are still needed to bridge the gap between experimental platforms and industrial applications. In addition to the fundamental drivers that promote catalytic performance, engineering aspects such as device architecture and process coupling deserve to be studied and highlighted, as they could indeed facilitate the deployment of this fundamental research on an industrial scale. In this regard, more effort should be devoted to developing high-performance electrolytic devices to minimize the mass transfer limits of reactants, which can significantly improve energy efficiency. Among these, the rapid development of reactors can accelerate the transformation of green ammonia synthesis technology from a laboratory platform to industrial scale production.

Ideal electrolytic reactors should have a good function of promoting electron transfer, ion transfer, and controlled gas diffusion, while preventing the mixing of the electrolyte and products. The rational design of the reactor is very vital for achieving a high EE for NH_3 synthesis. In this section, the setup of each reactor and the associated experimental procedures will be briefly described. The advantages and disadvantages of each reactor will also be discussed.

It is well known that a reactor can use input energy to drive non-spontaneous reactions. At present, various reactors have been designed for the synthesis of NH_3, such as single-chamber cells, H-type cells, flow cells, and MEA reactors, which consist of an electrode, an electrolyte, a GDE, and a diaphragm. Taking the three-electrode electrolyzer of a single-chamber cell as an example, it is composed of a measuring circuit and a polarization circuit, forming a closed-loop circuit between the CE and the WE, with the potential of the WE determined by the RE. In an actual electrocatalytic reaction process, when an external voltage is applied to the reaction system, the ions in the electrolyte will be driven by an electrode with opposite charges, and a reduction or oxidation reaction will occur at the cathode or anode to produce the target products.

In addition, the H-type cell, consisting of two chambers (anode and cathode), is separated by ion exchange membranes. A reduction reaction occurs in the cathode chamber and an oxidation reaction happens on the other side. The ion exchange membranes can effectively block the crossing of different ions and avoid the loss of products. The flow cell device consists of a gaseous cathode chamber, a liquid cathode chamber, and an anode chamber (Fig. 13(a)). A hydrophobic GDE is used to separate the gas–liquid cathode chamber, and the target reaction occurs within the three-phase boundary of the GDE. The GDE as the cathode is completely immersed in the electrolyte, while the configuration exposes one side to the feed gas, allowing the liquid and gas phases to coexist within the catalyst layer. Recently, emerging GDEs combined with flow cell devices have efficiently boosted NH_3 synthesis performance and pushed the current density to practical levels by reducing the mass transport limitation of the gas phase. After iterative updating of the reactor, the latest high-performance MEA devices consist of catalysts pressed directly onto both sides of the ion exchange membrane. The MEA configuration takes advantage of the GDE configuration in the flow cell while minimizing the use of electrolyte through direct contact between the catalyst layer and the ion exchange membrane (Fig. 13(b)). This configuration can significantly reduce the full-cell resistance, greatly increasing the current density. Despite the suitability of H-cells and GDE configurations for basic research, such as catalyst development, MEA configurations are highly attractive for industrial applications, while further optimization of components is a promising direction. However, the development of MEAs and catalysts has been carried out separately so far. Therefore, new opportunities exist to translate the catalytic strategies developed in the H-type/flow cell regime into MEA devices to improve the energy efficiency of the whole cell. At the same time, when a catalyst is considered for commercial applications, its important performance indicators at high current densities should be carefully reported. It is also worth noting that catalytic stability tests are typically conducted over a few hours, rather than the hundreds to thousands of hours required for industrial applications. Moreover, many catalyst deactivation mechanisms, such as surface reconstruction, contamination, and mechanical failure, are likely to occur during long-term electrolysis; these phenomena must be carefully examined. In addition, the accurate quantification of reactor energy efficiency and related conversion products is

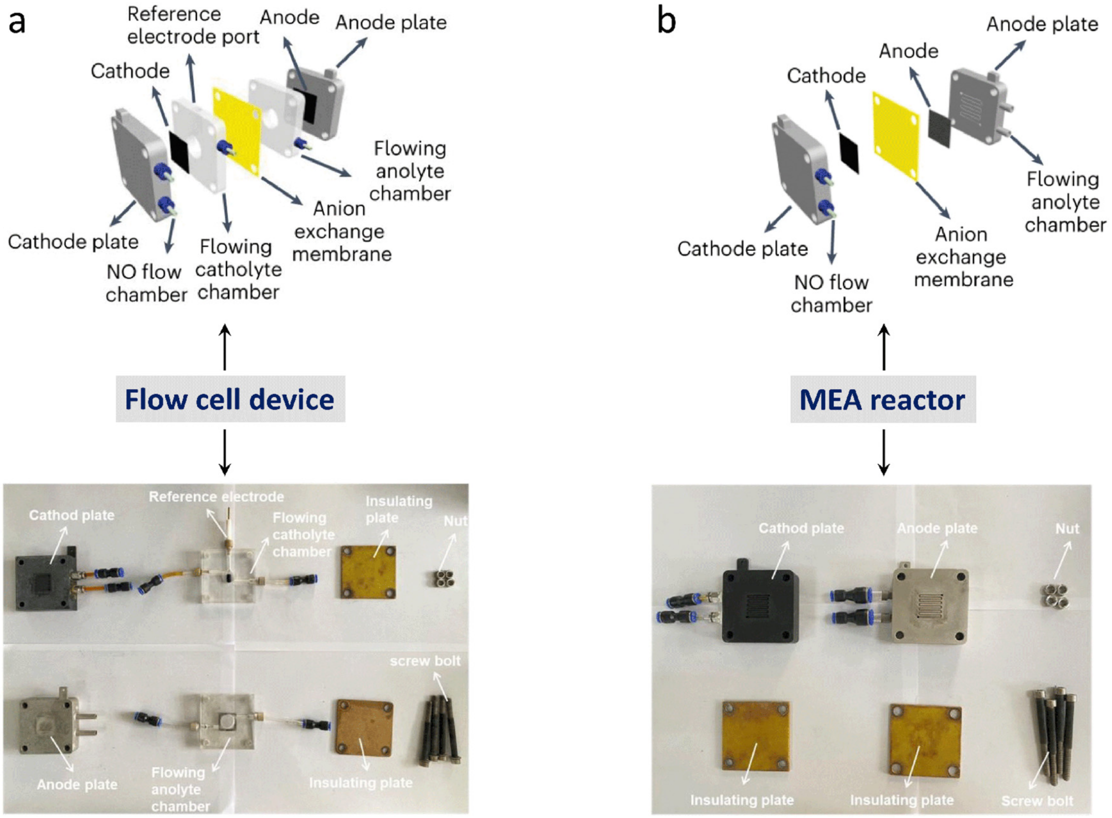

Fig. 13 Schematic illustration and digital photos of a (a) flow cell device and (b) MEA reactor. Reproduced with permission from ref. 292 Copyright 2023, Springer Nature.

particularly important. These parameters will help to evaluate and standardize the industrialization process of electrochemical NH_3 synthesis more strictly.[288]

Based on the various types of reaction devices, a corresponding summary is made. Specifically, the structure of the traditional three-electrode device is a single-chamber reactor, where reduction and oxidation reactions are carried out in the same electrolyte environment. For example, NH_3 products were produced using a three-electrode single cell, with a Pt mesh and an Ag/AgCl electrode as the counter and reference electrodes, respectively. 5.0 mg of the catalyst was dispersed into 1000 μL of a solvent consisting of 400 μL of distilled water, 500 μL of ethanol, and 100 μL of Nafion to achieve a homogeneous catalyst ink by ultrasonication. Then, 50 μL of an ink of sulfur-and-nitrogen-codoped carbon matrix loading single Fe atoms (Fe_{SA}-NSC) was loaded on carbon paper (1×1 cm^2) to prepare the working electrode. Before NRR tests, the electrolyte was purged with N_2 gas for 30 minutes. The three-electrode reaction system based on Fe_{SA}-NSC exhibited excellent performance, with a yield rate of 30.4 μg h^{-1} $mg_{cat.}{}^{-1}$ and an NH_3 FE of 21.9% at −0.4 V, surpassing those of most reported Fe-based electrocatalysts developed to date.[289] Besides, a single-reaction cell with a metal–nitrogen–carbon catalyst was also used to promote the electrosynthesis of NH_3 under mild conditions, illustrating the reliability of the single-chamber reactor, with a remarkable yield rate of 31.9 μg h^{-1} $mg_{cat.}{}^{-1}$ and NH_3 FE of 11.8% at −0.4 V.[5]

The H-type cell is currently widely used in reactions involving product upgrading, such as the carbon dioxide reduction reaction, the oxygen reduction reaction, and the NH_3 synthesis reaction. In the H-type cell, the redox reaction chambers are usually separated by ion exchange membranes of different types and models, making the reaction environment of the anode and cathode relatively independent so that the two chambers can be controlled more flexibly. Recently, a typical two-compartment H-type cell was adopted, separated by a Nafion 211 membrane and containing Ag/AgCl as the reference electrode and a Pt wire as the counter electrode, to conduct NH_3 electrosynthesis, achieving a high yield rate of 16.1 μg h^{-1} $mg_{cat.}{}^{-1}$ and an FE of 11.8% in alkaline media.[12] Currently, single-chamber and H-type cells are the two most widely used reactors in electrocatalysis technology. However, it is worth noting that although the single-chamber reactor has a simple structure and is convenient to operate, the NH_3 generated on the cathode can easily diffuse to the anode in a narrow and connected environment and be further oxidized, resulting in a low yield rate and wasted electrical energy. Therefore, to solve this problem, without increasing the complexity of the reactor structure, the H-type cell uses a membrane to separate the oxidation and reduction reaction chambers, which are relatively independent, making it difficult for the prepared products to cross over. As a result, the H-type device has a more obvious advantage in improving the production yield. This effectively shows that the electrolyzer configuration indirectly determines the performance advantage of the catalytic system to a certain extent. Therefore, to promote the activity of the NH_3 synthesis system to the industrial standard, it is necessary to conduct an in-depth analysis and rationally design and optimize the electrolyzer structure, according to the key scientific issues causing the low activity index. For example, the distance between the WE and the RE leads to a large internal resistance in the traditional three-electrode single-chamber and H-type cells, resulting in a big gap between the electrochemical test performance and the commercial performance requirements. Furthermore, due to the slow dissociation step of the highly stable $N{\equiv}N$ bond, the NH_3 formation rate or NH_3 partial current density of the N_2 reduction reaction is extremely low ($\sim$0.1 mA cm^{-2}). The low productivity is not only far from industrial requirements, but even the influence of trace impurities makes the experimental results unreliable.

At the same time, due to the limited catalyst activity and the fierce competition of the cathode HER, the NH_3 production rate and FE achieved are still very limited. According to the performance targets required for the commercialization of the electrosynthesis of NH_3 published by the REFUEL program, most currently reported performance is far from satisfactory, and the road to industrialization and commercialization is still long. Therefore, it is necessary to further optimize the reactor, decrease its internal resistance, and construct a high-current-density and high-selectivity NH_3 electrosynthesis device.

To build efficient catalytic reactors, we should start from the essence of the synthesis reaction. The extremely low solubility of N_2 gas in aqueous solutions has two effects on electrochemical NH_3 production in aqueous solution: (a) the lower N_2 concentration in the electrolyte is not conducive to increasing the N_2 reduction to NH_3, compared to proton donors like water molecules and protons; (b) the NH_3 production rate can be limited by the mass transfer of N_2 molecules. To solve these problems, a reactor with a fast and efficient contact interface of gas–liquid–solid may be a promising approach. The three-phase boundary is a particularly significant concept in the field of fuel cells; it, which is the complex contact region that includes the reactant gas, the solvent, and the catalyst. In this case, the gas–liquid ratio in a conventional reactor can be effectively modified from gas-in-solvent to solvent-in-gas, so that mass transfer will not be a vital factor. In addition, to solve the surge of internal resistance in the reactor caused by excessive electrode spacing, polymer-based ion exchange membranes were introduced to construct MEA devices. The membrane can be a proton exchange membrane (PEM) or an anion exchange membrane (AEM). By constructing a near-zero-gap MEA reactor,[20] the internal resistance of the reactor can be reduced by orders of magnitude.

Based on the reactor optimization strategies understood above, the N_2 reduction activity was evaluated using a continuous flow cell with a 25 cm^2 GDE that has recently been produced. A three-chamber continuous flow cell was first constructed, where the GDE (stainless-steel cloth (SSC)) was placed between the reactant gas flow plate and the electrolyte flow plate (Fig. 14(a)). The N_2 and the electrolyte could be supplied to different sides of the GDE, in which the injected N_2 can directly participate in the reaction, breaking the mass transfer limitation (Fig. 14(b) and (c)). The design of the continuous flow reactor effectively improved NH_3 synthesis, with an FE of 61 ± 1% and an EE of 13 ± 1% at a current density of 6 mA cm^{-2} (Fig. 14(d)), under 1.0 bar and an effective area of 25 cm^2. Meanwhile, benefiting from more than half of the gas phase product being NH_3, the separation of the gas and liquid phases would cause low reactor resistance, further improving performance (Fig. 14(e)). Although the three-

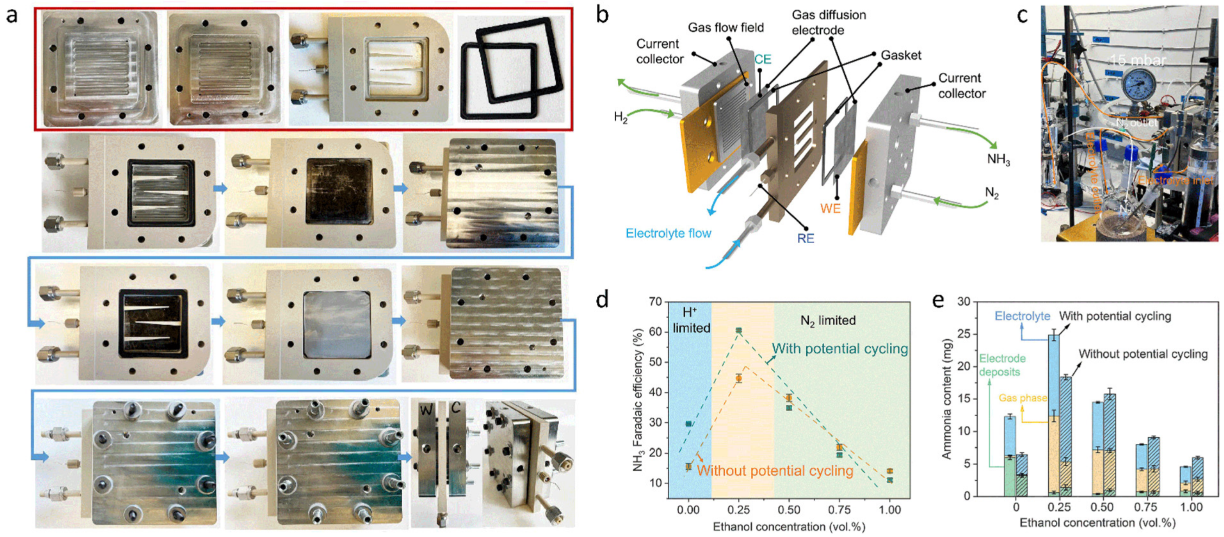

Fig. 14 (a) Digital photos of assembling a three-compartment continuous-flow reactor. (b) Schematic illustration of continuous-flow electrolyzer configurations. (c) Digital photo of the continuous-flow electrolyzer setup. (d) FE of NH_3 for a continuous-flow electrolyzer. (e) Produced NH_3 amounts for a continuous-flow electrolyzer. Reproduced with permission from ref. 280 Copyright 2023, American Association for the Advancement of Science.

compartment, continuous flow reactor achieved high FE and EE for NH_3 electrosynthesis, it does not solve all the problems at the industrial application level.[280] Future studies should focus on boosting the current density, facilitating the mass transfer process, and effectively regulating the pressure gradient between the gas and the electrolyte. The main goal is to achieve high FE and EE under industrial conditions. To solve the technical bottlenecks mentioned above, such as limited gas mass transfer and significant voltage loss, an MEA configuration based on a polymer electrolyte film was recently proposed. The cathode of Li-deposited stainless steel, the polymer electrolyte of a Li salt-doped polyethylene oxide film, and the anode of carbon paper containing Pt/C particles were pressed to form a 'three-in-one' MEA structure (Fig. 15(a)–(c)), which can be used in combination with a conventional gas diffusion electrolytic cell to significantly improve the efficiency of N_2 mass transfer. Due to the ultrathin membrane electrode, the ohmic impedance of the reactor was significantly reduced. Specifically, a yield rate of 2.41 ± 0.14 μmol h^{-1} cm_{geo}^{-2} and an FE of $8.9 \pm 1.7\%$ were obtained with a large catalytic area of 5.0 cm_{geo}^{-2}. With its advantages of efficient gas transfer, reduced solvent consumption, and compact design, the proposed MEA configuration will enable the most promising Li-NRR process to be applied in a practical manner (Fig. 15(d)). The advantages of an MEA device with a GDE have been clearly shown. In the following, the two types of reactors were also compared to inspire the optimal reaction configuration. An electrode with catalysts directly in contact with an ion exchange membrane was the first type of reactor, while in the second reactor, an additional GDE was inserted between the electrocatalyst layer and the Nafion membrane (Fig. 15(e) and (f)). The additional GDE serves two purposes: (i) it significantly reduces the amount of NH_3 that crosses the Nafion membrane; using an additional layer of GDE will eliminate the penetration of NH_3. (ii) The additional GDE hinders the proton transfer rate, thereby inhibiting the HER and ultimately improving the FE by reducing proton availability. Compared with the single GDE configuration based on an Fe_2O_3/CNTs catalyst, when the additional GDE configurations were used for NH_3 synthesis, the related NH_3 yield rate and FE increased by 158% and 571%, respectively, confirming the effectiveness of the strategy above.[291]

Based on previous technology development, optimizing the GDE and upgrading and scaling up the MEA reactor are expected to further advance NH_3 electrosynthesis technology to an industrial platform. Recently, a new type of GDE was developed that is different from commercial GDEs. In this new GDE, the microporous layer is first prepared by brushing a suspension of carbon black and polytetrafluoroethylene onto carbon paper. The mass ratio of PTFE in the microporous layer was 40 wt% and the carbon black loading was 1.0 mg cm^{-2}. Furthermore, the scaled-up MEA electrolyzer contained the prepared GDE loaded with a Cu_6Sn_5 catalyst with an active area of 100 cm^2 as the cathode and an iridium black-coated foam as the anode (Fig. 16(a)). A piece of quaternary ammonium poly(*N*-methylpiperidine-*co*-*p*-terphenyl) membrane served as the anion exchange membrane. The flow rate of the 0.5 M KOH electrolyte solution was maintained at 125 mL min^{-1}, and the flow rate of NO

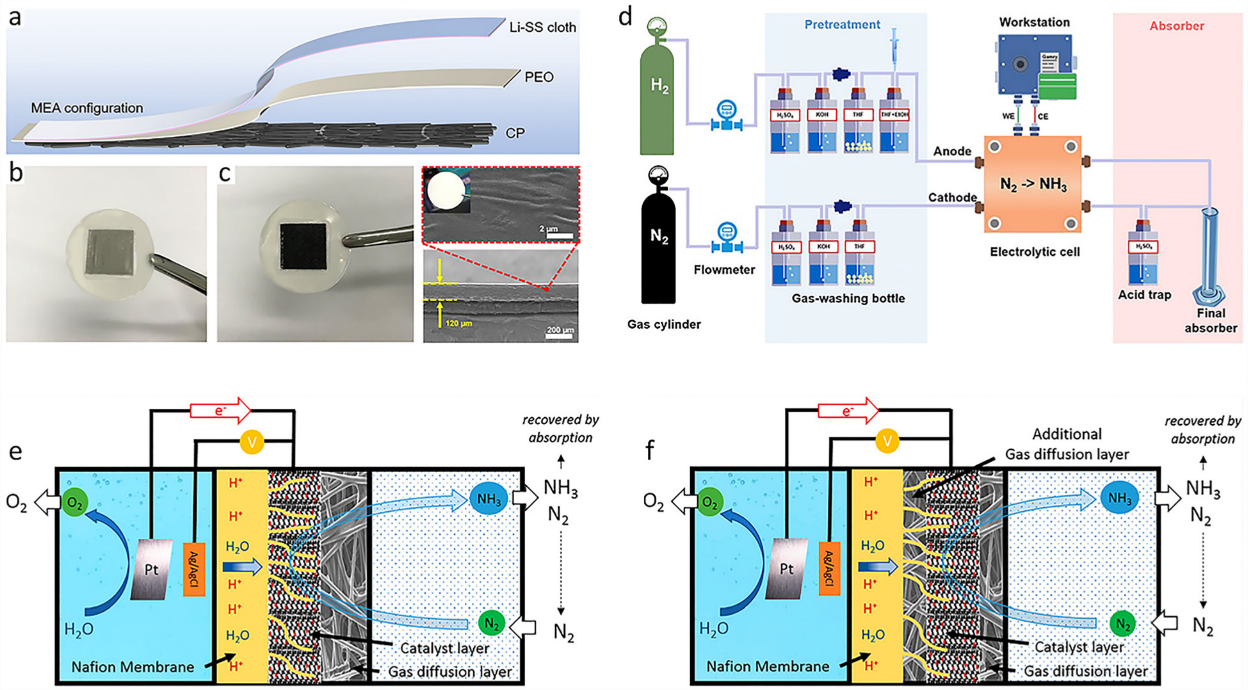

Fig. 15 (a) Schematic illustration of "three-in-one" MEA. Digital photos (b) and SEM images (c) of a "three-in-one" MEA loading catalyst. (d) Complete flow chart of a synthetic NH_3 device. Schematic illustration of (e) the three-phase reactor without additional GDE, and (f) the upgraded three-phase reactor with additional GDE. Reproduced with permission from ref. 290 Copyright 2023, The Royal Society of Chemistry. Ref. 291 Copyright 2017, American Chemical Society.

was controlled at 1.875 L min^{-1}. Benefiting from the upgrade of the MEA device, the NH_3 yield rate in a scaled-up electrolyzer based on the Cu_6Sn_5 material achieved ~2.5 mol h^{-1} with an NH_3 FE of about 80% at an ultra-high current of 400 A (Fig. 16(b) and (c)). The results presented here indicate that the sustainable production of NH_3 is feasible in a reverse nitrogen cycle driven by renewable electricity.[292]

In addition, it is well known that the most important function of the GDE is to bring the reaction gas, electrolyte, and catalyst into close contact, minimizing the diffusion distance of the reaction gas and thus greatly increasing the diffusion rate. Therefore, the GDE is usually subjected to a hydrophobic treatment to prevent the electrolyte from penetrating and wetting its fiber structure. Unfortunately, if the main component of the electrolyte is a non-aqueous solvent, the hydrophobic interaction between the GDE carrier and the electrolyte will be lost. In this case, the electrolyte will enter the fiber structure of the GDE and flood the catalyst, leading to a greatly increased diffusion distance and a reduced current density for the reaction. Therefore, for a non-aqueous NH_3 synthesis system, optimizing the internal components of the reactor is also important. Following this idea, GDE-like functionality is achieved by controlling material wetting and electrolyte penetration into the support in a non-aqueous system (Fig. 16(d)).[98] Specifically, a stainless steel cloth (SSC) was used as a substrate for catalyst deposition, and electrolyte penetration was controlled by maintaining a pressure gradient (Fig. 16(e)–(g)). This method was used for an efficient HOR on Pt-coated SSC at a current density of 25 mA cm^{-2} in THF and propylene carbonate-based electrolytes. In addition, Li metal loaded on an SSC substrate was able to produce NH_3 using the Li-NRR method. The partial current density of NH_3 was 8.8 ± 1.4 mA cm^{-2}, and the FE was 47.5 ± 4.0%. The two electrodes were coupled together to build an NH_3 synthesis reactor, which had a high FE of 30 ± 2%.[98]

Although these electrocatalysts have made progress in highly selective NH_3 production, their current density and NH_3 yield rate are far below practical application requirements. A large part of the problem stems from the fact that current reactors lack short-term ion balance and stability. For high-efficiency NH_3 synthesis, a suitable reactor remains to be developed. Based on this challenge, a reactor equipped with a bipolar membrane (BPM) and a Cu-activated Co electrode was used to synthesize NH_3.[293] Specifically, the catalyst in the BPM

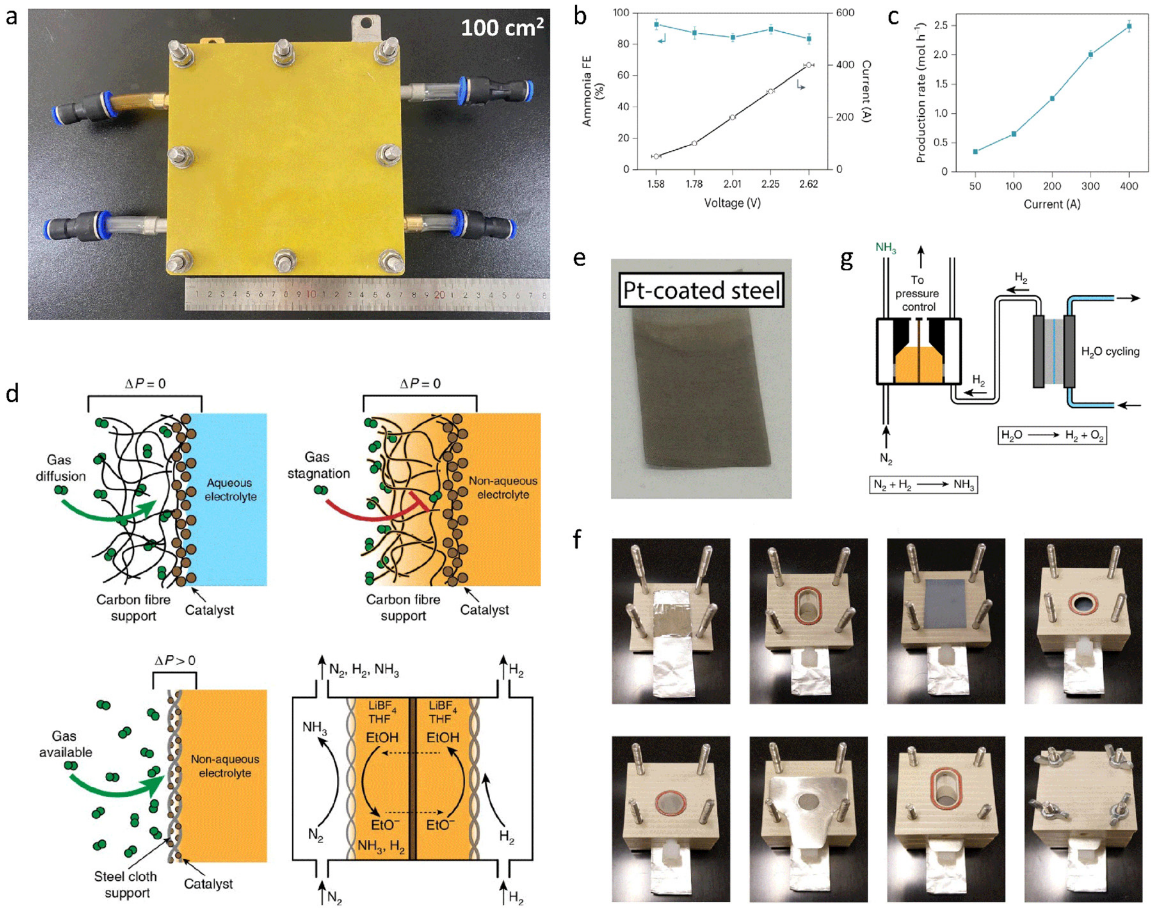

Fig. 16 (a) Digital photo of the large area MEA electrolyzer. (b) NH_3 FE, and (c) NH_3 yield rate at high current. (d) Carbon fiber supported GDE in aqueous and non-aqueous environments and upgraded steel cloth supported GDE applied in non-aqueous environments. (e) Photo of Pt-coated steel cloth. (f) Digital photos of assembling a three-compartment cell with a steel cloth supported GDE. (g) Pressure controlled NH_3 electrosynthesis reactor. Reproduced with permission from ref. 292 Copyright 2023, Springer Nature. Ref. 98 Copyright 2020, Springer Nature.

intermediate layer effectively dissociates H_2O molecules, and the resulting H^+/OH^- moves from the intermediate layer to the poles, ensuring ionic equilibrium.[208,294] The target optimized reactor based on the BPM membrane delivered an excellent FE of 96.45% and a high NH_3 yield rate of 279.44 mg h^{-1} cm^{-2}, as well as a high current density of 2.64 A cm^{-2}. To facilitate the practical application of scalable NH_3 synthesis, a BPM reactor with a large-area electrode (10 × 10 cm^2) was constructed for the gram-scale synthesis of NH_3. Under a constant current condition of $\sim$40 A, the yield rate and FE can reach 4.11 g·h^{-1} and 97.19%, respectively, thus showing great potential for industrial NH_3 production.[293]

Based on the important breakthrough in the field of BPM reactors for NH_3 electrosynthesis, optimizing the BPM interface is expected to further promote the electrosynthesis of NH_3 toward large-scale applications. The ionic selectivity of bipolar membranes is formed by the principle of electrostatic repulsion. Although H^+/OH^- ions produced *in situ* can adjust the acid–base microenvironment, the structure or performance of the ionic membranes will be degraded. Therefore, to solve this problem, physically interlocked bipolar membranes were prepared according to the traditional 'mortise-tenon joint' structure. The membranes with a 3D physically interlocked interface can efficiently dissociate water, and the imbalance of ion migration can be eliminated in the *in situ* acid–base environment, thus realizing the continuous, stable operation of the NH_3 electrosynthesis process (Fig. 17(a) and (b)). Among them, the innovative design of the bipolar membrane with an interlocking structure not only increases the sites for water splitting but also cleverly uses the 'self-swelling'' effect of the polymer in water to achieve a 'self-locking' effect, improving the stability of the bipolar membrane (Fig. 17(c)). The electrosynthesis of NH_3 was carried out using a reactor based on a BPM with a 'mortise-tenon joint' structure, which achieved an FE of 86.2% and an NH_3 production rate of 68.4 mg h^{-1} cm^{-2} using merely 2000 ppm NO_3^- in alkaline electrolytes at a high current density of 1000 mA cm^{-2}. Moreover, a >100-hour operation at 1000 mA cm^{-2} also endorsed the confidence of using the as-prepared BPM reactor at a high FE and yield rate (Fig. 17(d)).[295]

Through the development of high efficiency conversion technology, high activity catalysts, and high-performance reactors, NH_3

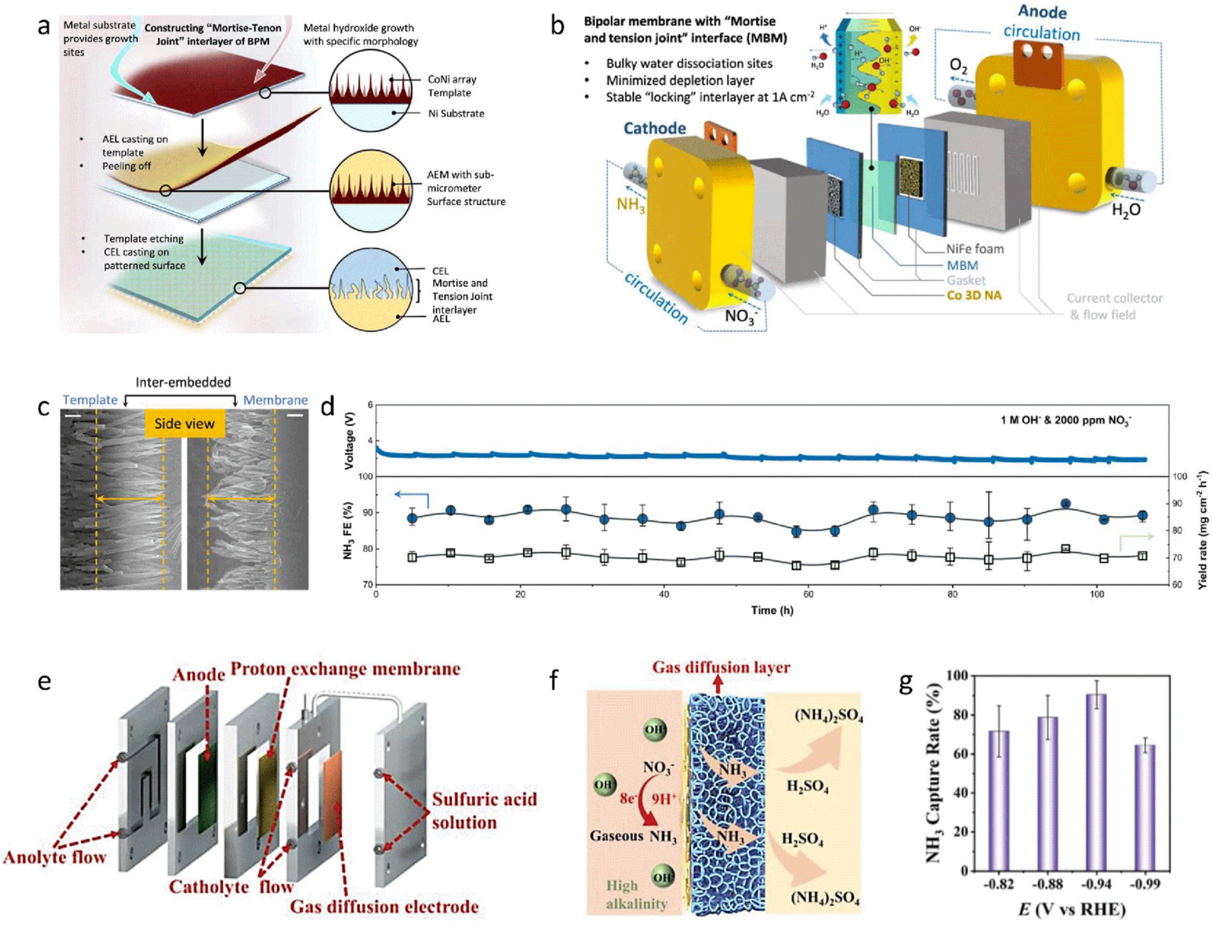

Fig. 17 (a) Schematic illustration of the "Mortise–Tenon Joint" structure of BPM. (b) Schematic illustration of the BPM reactor for NH_3 synthesis. (c) SEM images of the "Mortise–Tenon Joint" structure of BPM. (d) FE and yield rate of NH_3 for a long-term BPM synthesis system at a high current density of 1000 mA cm^{-2}. (e) Schematic illustration of a "two-in-one" reactor integrating the electrolytic and NH_3 capture chamber. (f) Schematic illustration of capturing NH_3 using a gas diffusion layer. (g) Diagram of the NH_3 capture rate. Reproduced with permission from ref. 295 Copyright 2023, Springer Nature. Ref. 296 Copyright 2022, Wiley-VCH.

synthesis technology has made great progress. However, in the advance of synthetic NH_3 technology, although NH_3 production and capture are equally critical for practical applications, not enough attention has been paid to capturing it from the electrolyte. Based on the fact that almost all NH_3 generated in the low-current NH_3 synthesis process is in a gaseous state on the electrode surface, a 'two-in-one' electrolytic cell was recently designed to integrate the electrolytic chamber and the NH_3 capture chamber through a commercial GDE, aiming to achieve simultaneous NH_3 production and capture (Fig. 17(e)).[296] The prepared electrolyzer promoted NH_3 synthesis by rapidly moving products away from the three-phase interface. Specifically, by using a sulfuric acid solution to capture the synthesized NH_3, the two liquid flow plates were separated by a commercial GDE (Fig. 17(f)). The gaseous NH_3 generated on the other side of the GDE loaded with catalyst spontaneously passed through the GDE and directly came into contact with the plate of flowing H_2SO_4 solution to achieve real-time preparation and capture of NH_3 products. Consequently, through a carefully designed synthesize-and-capture monolithic reactor, a yield rate of 2.1 mmol h^{-1} cm^{-2} was obtained at a high current density of 528.0 mA cm^{-2}, along with a high capture efficiency of 90.4% (Fig. 17(g)).[296]

8.2 Photocatalytic ammonia synthesis reactors

In photocatalytic systems, quartz glass reactors are commonly used (Fig. 18(a)),[297] equipped with magnetic stirring devices, a Xe lamp (with cut-off filters for spectral selection), a solar simulator, or actual sunlight illumination, along with gas bubbling apparatus. The photocatalyst powder is uniformly dispersed in the reactor containing the reactants and electrolyte solution. The reaction temperature is maintained at 25 °C (unless otherwise specified) through circulating cooling water. While such slurry-phase photocatalytic reactors offer operational simplicity and a large catalyst-reactant contact area, they present challenges including difficult catalyst recovery and low light utilization efficiency.

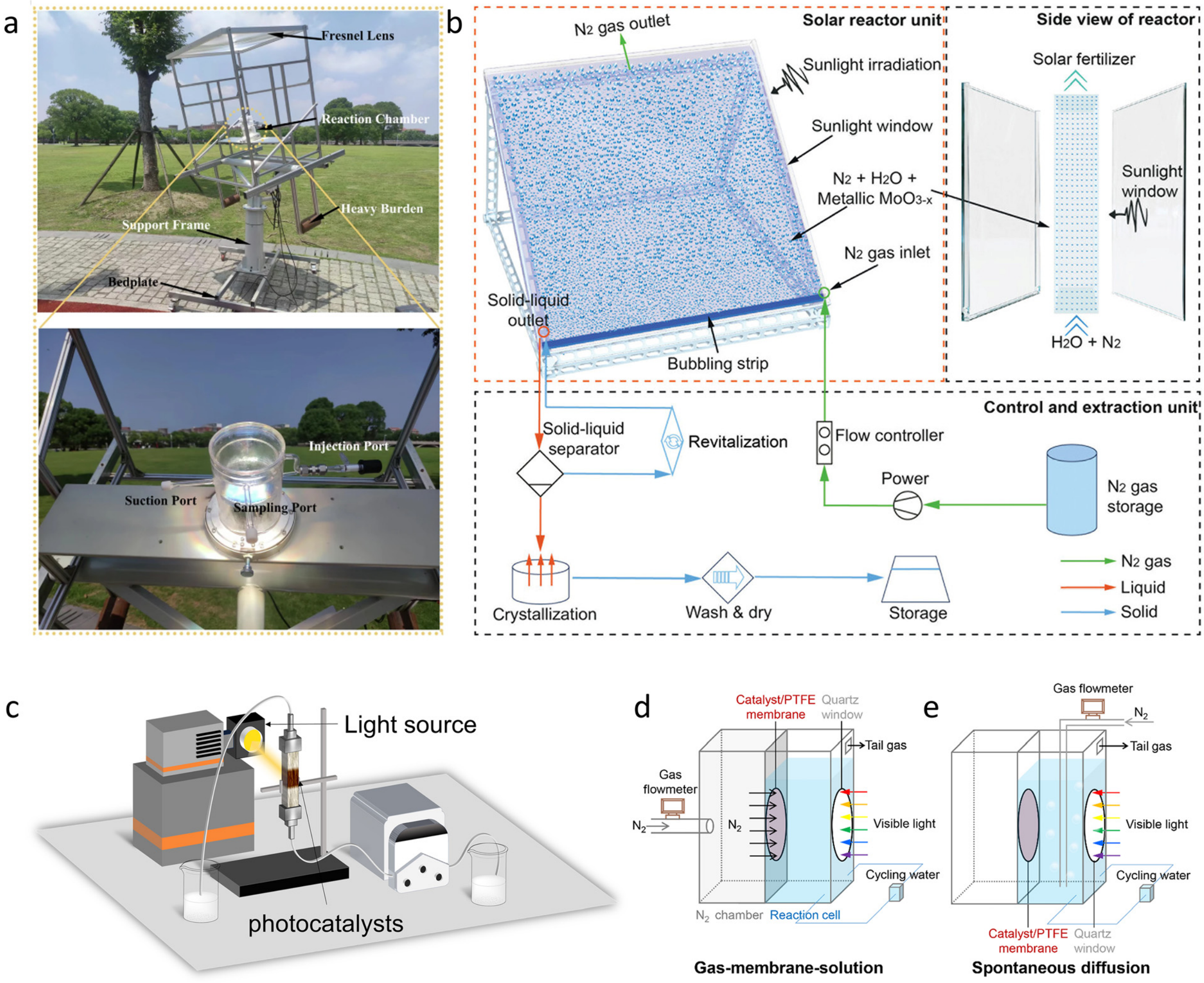

Fig. 18 (a) Digital photos of a quartz glass photocatalytic reactor. (b) Flat plate photocatalytic ammonia synthesis reactor. (c) Fixed-bed photocatalytic ammonia synthesis reactor. (d) Gas-membrane-solution photocatalytic ammonia synthesis reactor. (e) Spontaneous diffusion photocatalytic ammonia synthesis reactor. Reproduced with permission from ref. 297 Copyright 2024, Springer Nature. Ref. 298 Copyright 2025, Wiley-VCH. Ref. 129 Copyright 2021, American Chemical Society.

Recent advancements have led to the development of flat-plate and fixed-bed photocatalytic reactors (Fig. 18(b) and (c)).[298] In these systems, catalysts are immobilized on supports (*e.g.*, glass fibers, porous ceramics, and conductive substrates) as thin films or coatings. Illumination occurs either from one side or through the center of the catalyst-loaded support to drive photocatalytic ammonia synthesis. These reactors facilitate catalyst recovery and enable continuous-flow operation, although light penetration depth remains a limitation. Future designs could use three-dimensional porous supports to enhance both gas mass transfer and light harvesting. Additionally, a gas-membrane-solution reactor configuration has been developed (Fig. 18(d)).[129] In this design, fabricated catalyst/polytetrafluoroethylene (PTFE) membranes are sandwiched and sealed between gas chambers and reaction cells, with the catalyst side immersed in the reaction solution. Light irradiation through the reactor window illuminates the catalytic electrode while N_2 gas continuously diffuses through the PTFE side into the reaction cell for photocatalytic ammonia production. In another configuration, the spontaneous diffusion reactor immerses catalyst/PTFE membranes directly in the reaction solution (Fig. 18(e)).[129] During operation, high-purity N_2 gas is continuously bubbled through the solution while light irradiates the catalyst/PTFE membranes to drive the photocatalytic reaction.

The fundamental objective of photocatalytic ammonia synthesis reactors is to achieve efficient, stable, and scalable ammonia production. Based on the analysis above, future reactor optimizations should focus on: (1) enhancing light utilization efficiency through reflective internal surfaces to minimize light loss; (2) integrating low-temperature condensation and other separation technologies for timely product extraction; (3) improving reactor designs to maximize both photon capture and mass transport while maintaining practical scalability.

8.3 Photoelectrocatalytic ammonia synthesis reactors

Currently, photoelectrocatalytic ammonia synthesis systems primarily use three typical reactor configurations including the single-chamber cell, the H-type cell, and the flow cell, each with distinct structural characteristics and applications. Specifically, (1) the single-chamber cell reactor (Fig. 19(a))[299] consists of five key components: photoelectrocatalysts as the working electrode, a counter electrode, a reference electrode, an electrolyte, and a light source. The photoelectrode serves as the core functional unit, simultaneously performing light harvesting, charge separation, and catalytic reduction. The counter electrode maintains charge balance by completing the electrical circuit, while the reference electrode (*e.g.*, Ag/AgCl or Hg/HgO) enables precise control of the working electrode potential. The electrolyte system not only provides ionic conduction but also participates in proton-coupled electron transfer processes. In typical operation, light penetrates through a quartz window to

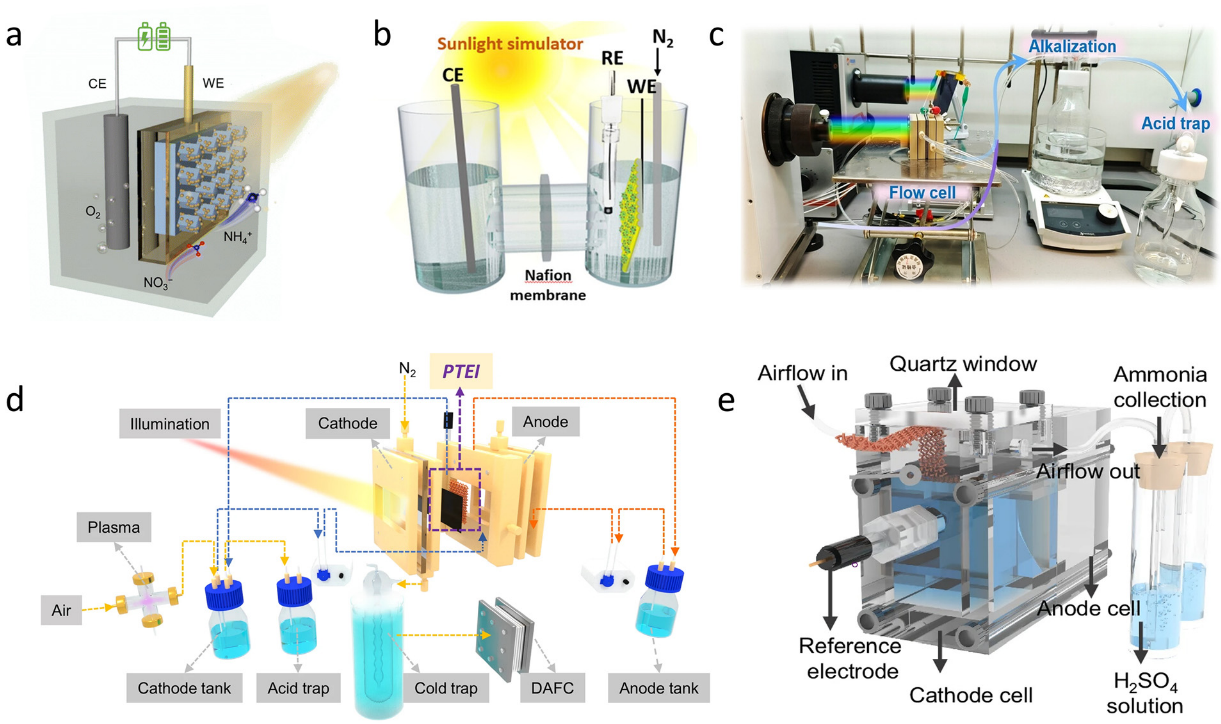

Fig. 19 (a) Schematic illustration of a single chamber photoelectrocatalytic ammonia synthesis reactor. (b) H-type photoelectrocatalytic ammonia synthesis reactor. (c) Digital photo of a flow-cell photoelectrocatalytic ammonia synthesis reactor. (d) Schematic illustration of a flow-cell photoelectrocatalytic ammonia synthesis reactor. (e) Schematic of harvesting ammonia products from the reactor. Spontaneous diffusion photocatalytic ammonia synthesis reactor. Reproduced with permission from ref. 299 Copyright 2024, The Royal Society of Chemistry. Ref. 300 Copyright 2023, American Chemical Society. Ref. 301 Copyright 2024, Wiley-VCH. Ref. 302 Copyright 2025, Springer Nature.

illuminate the photoelectrode, driving ammonia synthesis under an applied bias. However, this simple design has significant drawbacks: ammonia products generated at the cathode readily diffuse to the anode region, leading to product oxidation and consequently severe reduction in reaction selectivity and faradaic efficiency. (2) The H-type cell reactor (Fig. 19(b)):[300] to address the limitations above, the H-type cell uses a dual-chamber structure physically separated by an ion-exchange membrane, isolating the cathode chamber (containing the photoelectrode) from the anode chamber (containing the counter and reference electrodes). This separation effectively prevents ammonia from diffusing to the anode side, significantly increasing the ammonia production rate. Nevertheless, the H-type cell introduces new technical challenges: (i) the large electrode-membrane spacing substantially increases internal resistance; (ii) the static reactor design severely limits the mass transport of nitrogen sources; (iii) the batch operation mode cannot meet industrial-scale continuous production requirements. These inherent limitations ultimately constrain the maximum achievable current density and practical applicability. Therefore, the flow cell reactor successfully overcomes these constraints through a revolutionary structural design. (3) The flow-cell reactor (Fig. 19(c) and (d)):[301,302] distinct from conventional configurations, flow cells use highly integrated modular designs with core components including bipolar plates, photoelectrode pairs (photocathode/anode), peristaltic pump systems, gas diffusion layers (GDL), and ion-exchange membranes. The bipolar plates provide mechanical support and sealing while serving as efficient current collectors to construct compact electron conduction networks. Notably, the precisely engineered microfluidic channels (*e.g.*, serpentine or parallel patterns) on the bipolar plate surfaces enable the directional transport of reactants and products, effectively mitigating concentration polarization. Coupled with pump-driven forced convection and GDL-optimized gas transport, this design dramatically enhances reaction efficiency at triple-phase boundaries. Light irradiation through specialized transparent conductive windows (*e.g.*, FTO glass) activates the photocathode surface, enabling efficient ammonia synthesis under optimized potential control. Furthermore, integrating an acid solution absorption device enables real-time product collection, significantly improving overall production efficiency (Fig. 19(e)).[302]

Based on this analysis, the future development of photoelectrochemical ammonia synthesis reactors should focus on the advanced optimization of flow-cell systems, including: (1) multi-scale channel designs for enhanced mass transport; (2) the multifunctional integration of bipolar plates for electrical conduction, thermal management, and mechanical stability; and (3) synergistic regulation strategies for photo-electro-thermal field coupling. These innovations will accelerate the transition of photoelectrochemical ammonia synthesis toward industrial-scale applications.

8.4 Alkali metal mediated ammonia synthesis reactors

The reactor serves as the pivotal platform in lithium-mediated ammonia synthesis, enabling both nitrogen activation and lithium cycling. Its structural design and operational parameters fundamentally govern the reaction kinetics and ammonia selectivity. The technology has evolved through three progressive reactor configurations: primitive single-chamber reactors addressing the direct interaction of lithium and N_2, optimized continuous-flow reactors for precise control of the gas–liquid–solid interface, and advanced solid-state electrolyte reactors overcoming challenges in proton transport and lithium cycling stability. Specifically, (1) the single-chamber reactor is composed of an autoclave vessel, a single-chamber glass cell, a three-electrode system (a Pt wire as the reference electrode, a Pt net as the counter electrode, and stainless-steel cloth as the working electrode), a lithium salt, and an organic electrolyte. This reactor, with its simple structure, can effectively maintain direct contact between the lithium metal deposited on the working electrode and the nitrogen reactants under pressurized conditions and achieve the activation and reduction of the nitrogen reactants. However, this system is confronted with the challenges of lithium dendrite growth and the insufficient proton supply capacity of organic electrolytes, especially the severe electrolyte depletion that limits long-term stability and large-scale continuous ammonia synthesis. (2) Continuous-flow reactors effectively overcome the limitations of the single-chamber reactor. They adopt a three-chamber structure design, including a central flowing electrolyte chamber (promoting lithium-ion transport), a cathodic N_2 reduction chamber (achieving lithium-mediated nitrogen activation), and an anodic H_2 oxidation chamber (providing protons). This innovative configuration uses the physical isolation of reaction zones to achieve critical improvements: substantial suppression of lithium dendrite formation and parasitic side reactions, precise control over the gas–liquid–solid triple-phase boundary, and optimized synchronization between proton delivery and nitrogen reduction kinetics. The architectural design consequently enhances both system stability and faradaic efficiency, establishing a novel paradigm for selective ammonia synthesis. However, three persistent challenges remain: (i) limited proton mobility in organic media, (ii) the progressive decomposition of organic electrolytes under reductive potentials, and (iii) spatially heterogeneous lithium deposition and dissolution behavior leading to current density variations across the electrodes. (3) Solid-state electrolyte reactors mainly use solid-state lithium-ion conductors to replace liquid organic electrolytes. These solid electrolytes offer fundamental advantages: they integrate proton and lithium-ion dual conduction characteristics, construct directional transport channels, and significantly reduce mass transfer resistance. In addition, they eliminate the problem of liquid organic electrolyte loss, as they can withstand high voltage and strong reducing environments, thereby extending reactor stability. The rigid solid-state electrolytes can mechanically inhibit the penetration of lithium dendrites, and surface modifications (such as artificial SEI layers) can induce the uniform deposition and dissolution of lithium. This system further decouples and optimizes the three functional zones of nitrogen reduction, proton supply, and lithium cycling through a modular stacking design, providing a possible path for achieving the efficient and stable industrialization of ammonia synthesis.

8.5 Optimization strategies and directions for ammonia synthesis reactors

Recently, reactors for ammonia synthesis have been updated from single-chamber cells, H-type cells, and flow cells to MEA electrolyzers. Among these, the mass transfer limit of the reactants and the internal resistance of the reactors have been significantly reduced, achieving efficient ammonia synthesis. However, further optimization and improvement of the reactors will contribute to the industrialization of green ammonia synthesis technology. Therefore, considering the composition of advanced MEA electrolyzers (including cathode/anode electrodes, cathode/anode plates, GDEs, ion-exchange membranes, and flow channels) as well as the subsequent product separation and purification steps, we think that the following aspects should be carried out in the design of future reactors: (1) ion-exchange membranes are some of the core components, and their properties directly affect proton conduction efficiency, ammonia selectivity, system stability, and energy consumption. Therefore, new short-side-chain perfluorosulfonic acid membranes or non-fluoropolymers should be developed and designed to reduce membrane resistance. Alternatively, proton jumping sites should be introduced by doping heteropoly acids or ionic liquids to reduce the internal resistance and accelerate proton mobility, thereby improving reactor performance. In addition, by introducing basic groups and other means to enhance the corrosion resistance of the proton exchange membrane, coupled with strengthening its mechanical strength, the stability of the proton exchange membrane is improved, realizing the industrial application potential of green ammonia synthesis. The gradient structure of the ion-exchange membrane is equally important. It can use the asymmetric pore distribution and hydrophilic–hydrophobic gradient of the membrane itself to regulate gas permeation and drying phenomena, while also promoting the supply of protons to the cathode and preventing water flooding. Besides, we should integrate bipolar membranes into reactors, where water molecules dissociate within the bipolar membrane structure, rapidly providing protons for the cathode chamber. Meanwhile, asymmetric acid/base reactions are achieved at the anode and cathode, optimizing the thermodynamics of the system and ultimately enhancing the performance of the ammonia synthesis reactors. (2) The preparation methods for electrodes in MEA electrolyzers mainly include catalyst-coated membrane (CCM) and catalyst-coated substrate (CCS). Among them, the CCS strategy directly coats the catalyst ink on the gas diffusion layer (GDL) to form a GDE. Then, it is combined with the ion-exchange membrane through hot pressing and assembled into MEA electrolyzers. The CCS technology will lead to a relatively high interface resistance. The CCM technology directly coats the catalyst ink on both sides of the ion-exchange membrane to form anode and cathode catalyst layers, which are then combined with the GDL through hot pressing. This technology can achieve zero-gap MEA electrolyzers, significantly reducing the internal interface resistance of the reactor and realizing high-performance ammonia synthesis at the device level. It is also worth noting that renewable energy has intermittent characteristics. During the start-up and shutdown of MEA electrolyzers, the electrode potential can change, reducing the yield of the target products. Therefore, developing a cathode electrode that can operate stably at a wide current density is of great significance for enhancing the product yield. (3) Various flow channel configurations are constructed by multi-scale simulation technology, including serpentine, leaf-vein, interdigitated, and composite flow channels, to optimize the flow channels of MEA electrolyzers, reducing local concentration polarization and enhancing mass transfer within the reactors.

In addition, to promote the industrialization of green ammonia synthesis technology, megawatt-level MEA electrolyzers are achieved by connecting standardized reactor units in parallel or series, while avoiding uneven performance caused by overly large single tank sizes within MEA electrolyzers. It is also necessary to pay attention to the overheating problem of the reactor under high current density. Built-in cooling channels can extend the operating stability of the reactors and electrodes. At the same time, the hydrophobic/hydrophilic regulation of the GDE can control the mass transfer of the reaction gas and the water immersion of the electrodes. To enhance the economic efficiency of the overall system, ammonia separation, capture, and collection devices can be coupled with the reaction system. In conclusion, through multi-disciplinary collaborative innovation, such as in computational science, materials science, and artificial intelligence science, the development of reactors with high current density, high FE, and durable stability is expected to become the core technology for green ammonia production.

9. Summary and outlook

Recent advances in green ammonia synthesis have been systematically reviewed. First, we outline the reaction mechanisms and fundamental research aspects of using multiple nitrogen sources (N_2, NO, NO_2^-, and NO_3^-) for ammonia synthesis, covering detection methods, reactor design, measurement protocols, and catalytic activity descriptors. Next, we comprehensively analyze the critical factors governing different green synthesis approaches—including photocatalytic, electrocatalytic, photoelectrochemical, lithium-mediated, and calcium-mediated methods—with an emphasis on activity metrics such as faradaic efficiency and NH_3 yield rate, reaction mechanisms, and optimization strategies. Additionally, we explain the structure–activity relationships of various catalysts to establish design principles for enhanced ammonia performance. Finally, we discuss future research directions, such as the development of advanced catalysts and reactor systems, *operando* characterization techniques for mechanistic insights, and scalability challenges for industrial adoption.

Specifically, we first explain the reaction pathways and reduction mechanisms of various nitrogen sources, including dissociative, associative, Mars–van Krevelen, Tafel-dissociative, Tafel-associative, Heyrovsky-dissociative, Heyrovsky-associative, indirect autocatalytic, and direct catalytic reduction pathways.

We then detail ammonia detection methods, such as chemical detection using Nessler's reagent, indophenol blue, and salicylate, fluorometric detection, and titrimetric assays, as well as advanced techniques like isotope labeling, ^{1}H NMR, electrode-based sensing, UV-vis spectrophotometry, ion chromatography, and gas chromatography. Additionally, we outline key electrochemical experimental protocols, covering electrode preparation and functionalization, standard potential calibration, linear sweep voltammetry, chronoamperometry, cyclic voltammetry, electrochemical impedance spectroscopy, and multi-potential step measurements. Critical activity metrics, including faradaic efficiency, NH_3 yield rate, energy efficiency, and stability, are also systematically evaluated to provide readers with a foundational understanding of green catalytic ammonia synthesis. Subsequently, the discussion is organized into five sections, each focusing on advanced catalyst synthesis and performance optimization based on distinct catalytic technologies.

Among these, we provide an in-depth analysis of high-profile green catalytic ammonia synthesis technologies, including photocatalytic, electrocatalytic, photoelectrocatalytic, and alkali metal-mediated approaches. By addressing critical scientific challenges—such as photogenerated charge recombination, poor reactant solubility, weak N_2 adsorption, inefficient $N\equiv N$ bond dissociation, limited proton affinity, the large energy gap of N_2 molecules, dominant competitive reactions, and unfavorable rate-determining steps—we systematically evaluate catalyst modification strategies and reaction system optimizations to enhance performance and explain structure–activity relationships. Furthermore, we identify key approaches for improving faradaic efficiency, energy efficiency, and NH_3 yield rates, offering a foundational framework and future directions for advancing green ammonia synthesis research.

However, we note that despite significant advancements in innovative electrocatalysts driving progress in green ammonia synthesis, this emerging field remains hindered by critical challenges—including low current density, insufficient catalytic activity, and suboptimal faradaic efficiency and energy efficiency, which collectively impede commercialization. A key yet often overlooked factor is the electrolyzer, an essential component of the reaction system, whose synergistic role with the catalyst is pivotal for efficient ammonia production. In the final section, we comprehensively review the evolution of reactor designs over the past year, beginning with the basic configuration and components of single-chamber cells, progressing to H-type cells with diaphragms to prevent reactant–product crossover and further to the gas diffusion electrode, which optimizes gas–liquid–solid triple-phase contact. We culminate with advanced membrane electrode assembly devices, which minimize internal resistance and enable zero-gap operation to enhance current density. Additionally, we analyze critical reactor components, including gas diffusion layers, diaphragm materials and architectures, and integrated gas capture-conversion systems. We firmly believe these insights will accelerate the transition of green ammonia synthesis from laboratory-scale research to industrial-scale applications.

Beyond providing newcomers with a foundational understanding of this research field and its core scientific challenges, this comprehensive review offers experienced researchers critical insights into accelerating large-scale practical applications. Despite significant interdisciplinary advancements, significant breakthroughs in both fundamental research and practical applications are still essential to achieve industrial-scale economic viability. Key considerations must include:

(1) From the catalyst's point of view, universal and robust synthesis strategies are essential for translating lab-scale technologies to industrial application. (2) From the reactor design point of view, reaction systems require careful optimization of electrolytes, membranes, and reactor configurations to maximize catalyst performance by mitigating nitrogen diffusion limitations, thereby meeting the stringent requirements of high NH_3 yield rates and faradaic efficiency for future ammonia synthesis systems. (3) From the theoretical simulation point of view, cutting-edge computational techniques—including density functional theory, artificial intelligence, and *ab initio* molecular dynamics—should be employed to predict catalytic enhancement mechanisms and guide the rational design of catalysts and reaction systems. (4) Some advanced *operando* characterization methods, such as *in situ* XRD, FTIR, XPS, Raman, and XAS, should also be used to further explore the actual active sites, reaction intermediates, and basic mechanism. (5) Experimental details should also be paid attention to to ensure reliable, reproducible results and eliminate false positives. (6) As research scales from nanomaterials to industrial reactors, biosafe and physically safe systems must be developed. Additionally, the design of cost-effective, high-performance components like catalysts and membranes will be one of the keys to the technology.

From the discussion above, although the research into the extensive construction of catalysts and the efficient production of large-scale reactors is challenging, it is also encouraging to explore in-depth the fundamental reaction mechanism, theoretical investigations, and robust characterization techniques coupled with trustworthy detection strategies, and to create an illuminating pathway for the future development and deployment of a value-added, clean-energy economy. In summary, there are both challenges and opportunities for the synthesis of ammonia through green catalytic pathways. Therefore, with further research and development and the continued efforts around the world, this very important field will make great contributions to the progress of science, technology, and society.

Author contributions

Z. K. completed writing – original draft, review, and editing. Z. K. and Y. H. carried out investigation and summarized the methodology. Z. K., D. S., T. Z., Y. L., L. D., and Y. H. contributed to helpful discussion during the writing of the manuscript. L. D. and Y. H. performed supervision. Y. H., B. Y., Z. L., J. L., Q. Z., and L. L. provided resources. Y. H. performed funding acquisition and reviewing and editing of the manuscript. All authors discussed the results and commented on the manuscript.

Conflicts of interest

There are no conflicts to declare.

Data availability

No primary research results, software or code have been included, and no new data were generated or analyzed as part of this review.

Acknowledgements

We acknowledge the financial support from the National Key Research and Development Program of China (2022YFB 4002100), the National Natural Science Foundation of China (22425805, 22278364, U22A20432, 22211530045, 22178308, 22238008, and 22578393), the development project of Zhejiang Province's ''Jianbing'' and ''Lingyan'' (2023C01226), the Key Technology Breakthrough Program of Ningbo ''Science and Innovation Yongjiang 2035'' (2024H024), the Fundamental Research Funds for the Central Universities (226-2024-00060), and Zhejiang Provincial Natural Science Foundation of China under grant no. LD25B060001, the Fundamental Research Funds for the Zhejiang Provincial Universities (226-2025-00224). L. D. acknowledges partial financial support from the Australian Research Council (ARC, FL190100126 and CE230100032).

References

1 L. Hollevoet, M. D. Ras, M. Roeffaers, J. Hofkens and J. A. Martens, *ACS Energy Lett.*, 2020, **5**, 1124–1127.

2 S. Han, H. Li, T. Li, F. Chen, R. Yang, Y. Yu and B. Zhang, *Nat. Catal.*, 2023, **6**, 402–414.

3 P. H. V. Langevelde, I. Katsounaros and M. T. M. Koper, *Joule*, 2021, **5**, 290–294.

4 X. Yang, S. Mukherjee, T. O'Carroll, Y. Hou, M. R. Singh, J. A. Gauthier and G. Wu, *Angew. Chem., Int. Ed.*, 2023, **62**, e202215938.

5 Y. Li, J. Li, Dr. J. Huang, J. Chen, Y. Kong, B. Yang, Z. Li, L. Lei, G. Chai, Z. Wen, L. Dai and Y. Hou, *Angew. Chem., Int. Ed.*, 2021, **60**, 9078–9085.

6 X. Cui, C. Tang and Q. Zhang, *Adv. Energy Mater.*, 2018, **8**, 1800369.

7 V. Rosca, M. Duca, M. T. Groot and M. T. M. Koper, *Chem. Rev.*, 2009, **109**, 2209–2244.

8 R. Schlögl, *Angew. Chem., Int. Ed.*, 2003, **42**, 2004–2008.

9 X. Liang, H. Zhu, X. Yang, S. Xue, Z. Liang, X. Ren, A. Liu and G. Wu, *Small Struct.*, 2023, **4**, 2200202.

10 X. Zhao, G. Hu, G. Chen, H. Zhang, S. Zhang and H. Wang, *Adv. Mater.*, 2021, **33**, 2007650.

11 S. Wang, F. Ichihara, H. Pang, H. Chen and J. Ye, *Adv. Funct. Mater.*, 2018, **28**, 1803309.

12 Y. Kong, Y. Li, X. Sang, B. Yang, Z. Li, S. Zheng, Q. Zhang, S. Yao, X. Yang, L. Lei, S. Zhou, G. Wu and Y. Hou, *Adv. Mater.*, 2021, **34**, 2103548.

13 X. Peng, L. Zeng, D. Wang, Z. Liu, Y. Li, Z. Li, B. Yang, L. Lei, L. Dai and Y. Hou, *Chem. Soc. Rev.*, 2023, **52**, 2193–2237.

14 J. Choi, B. H. R. Suryanto, D. Wang, H. Du, R. Y. Hodgetts, F. M. F. Vallana, D. R. MacFarlane and A. N. Simonov, *Nat. Commun.*, 2020, **11**, 5546.

15 D. Bao, Q. Zhang, F. Meng, H. Zhong, M. Shi, Y. Zhang, J. Yan, Q. Jiang and X. Zhang, *Adv. Mater.*, 2017, **29**, 1604799.

16 J. G. Chen, R. M. Crooks, L. C. Seefeldt, K. L. Bren, R. M. Bullock, M. Y. Darensbourg, P. L. Holland, B. Hoffman, M. J. Janik, A. K. Jones, M. G. Kanatzidis, P. King, K. M. Lancaster, S. V. Lymar, P. Pfromm, W. F. Schneider and R. R. Schrock, *Science*, 2018, **360**, eaar6611.

17 J. N. Galloway, A. R. Townsend, J. W. Erisman, M. Bekunda, Z. Cai, J. R. Freney, L. A. Martinelli, S. P. Seitzinger and M. A. Sutton, *Science*, 2008, **320**, 889–892.

18 J. W. Erisman, M. A. Sutton, J. Galloway, Z. Klimont and W. Winiwarter, *Nat. Geosci.*, 2008, **1**, 636–639.

19 H. Jia and E. A. Quadrelli, *Chem. Soc. Rev.*, 2014, **43**, 547–564.

20 G. Qing, R. Ghazfar, S. T. Jackowski, F. Habibzadeh, M. M. Ashtiani, C. Chen, M. R. Smith III and T. W. Hamann, *Chem. Rev.*, 2020, **120**, 5437–5516.

21 J. Wang, T. Feng, J. Chen, V. Ramalingam, Z. Li, D. M. Kabtamu, J. He and X. Fang, *Nano Energy*, 2021, **86**, 106088.

22 K. Wang, D. Smith and Y. Zheng, *Carbon Resour. Convers.*, 2018, **1**, 2–31.

23 K. Zhang, A. Cao, L. H. Wandall, J. Vernieres, J. Kibsgaard, J. K. Nørskov and I. Chorkendorff, *Science*, 2024, **383**, 1357–1363.

24 G. Ertl, *Angew. Chem., Int. Ed.*, 2008, **47**, 3524–3535.

25 T. A. Bazhenova and A. E. Shilov, *Coord. Chem. Rev.*, 1995, **144**, 69–145.

26 M. A. Shipman and M. D. Symes, *Catal. Today*, 2017, **286**, 57–68.

27 C. J. M. Ham, M. T. M. Koper and D. G. H. Hetterscheid, *Chem. Soc. Rev.*, 2014, **43**, 5183–5191.

28 S. L. Foster, S. I. P. Bakovic, R. D. Duda, S. Maheshwari, R. D. Milton, S. D. Minteer, M. J. Janik, J. N. Renner and L. F. Greenlee, *Nat. Catal.*, 2018, **1**, 490–500.

29 B. H. R. Suryanto, H. Du, D. Wang, J. Chen, A. N. Simonov and D. R. Macfarlane, *Nat. Catal.*, 2019, **2**, 290–296.

30 S. J. Leigh, *Science*, 1998, **279**, 506–507.

31 G. Zhang, Y. Li, C. He, X. Ren, P. Zhang and H. Mi, *Adv. Energy Mater.*, 2021, **11**, 2003294.

32 L. Wang, M. Xia, H. Wang, K. Huang, C. Qian, C. T. Maravelias and G. A. Ozin, *Joule*, 2018, **2**, 1055–1074.

33 F. Chen, A. Elgazzar, S. Pecaut, C. Qiu, Y. Feng, S. Ashokkumar, Z. Yu, C. Sellers, S. Hao, P. Zhu and H. Wang, *Nat. Catal.*, 2024, **7**, 1032–1043.

34 X. Chen, Y. Cheng, B. Zhang, J. Zhou and S. He, *Nat. Commun.*, 2024, **15**, 6278.

35 Y. Wang, F. Hao, M. Sun, M. Liu, J. Zhou, Y. Xiong, C. Ye, X. Wang, F. Liu, J. Wang, P. Lu, Y. Ma, J. Yin, H. Chen,

Q. Zhang, L. Gu, H. Chen, B. Huang and Z. Fan, *Adv. Mater.*, 2024, **36**, 2313548.
36 X. Zhang, Y. Lyu, H. Zhou, J. Zheng, A. Huang, J. Ding, C. Xie, R. D. Marco, N. Tsud, V. Kalinovych, S. Jiang, L. Dai and S. Wang, *Adv. Mater.*, 2023, **35**, 2211894.
37 S. Ren, R. Gao, N. T. Nguyen and L. Wang, *Angew. Chem., Int. Ed.*, 2024, **63**, e202317414.
38 H. Jiang, G. Chen, O. Savateev and H. Wang, *Joule*, 2023, **7**, 253–256.
39 S. Feng, W. Gao, J. Guo, H. Cao and P. Chen, *ACS Energy Lett.*, 2023, **8**, 1567–1574.
40 L. Gao, Y. Cao, C. Wang, X. Yu, W. Li, Y. Zhou, B. Wang, Y. Yao, C. Wu, W. Luo and Z. Zou, *Angew. Chem., Int. Ed.*, 2021, **60**, 5257.
41 N. H. Deissler, J. B. V. Mygind, K. Li, V. A. Niemann, P. Benedek, V. Vinci, S. Li, X. Fu, P. C. K. Vesborg, T. F. Jaramillo, J. Kibsgaard, J. Drnecc and I. Chorkendorff, *Energy Environ. Sci.*, 2024, **17**, 3482–3492.
42 X. Fu, S. Li, N. H. Deissler, J. B. V. Mygind, J. Kibsgaard and I. Chorkendorff, *ACS Energy Lett.*, 2024, **8**, 3790–3795.
43 Y. Ren, C. Yu, X. Tan, Q. Wei, Z. Wang, L. Ni, L. Wang and J. Qiu, *Energy Environ. Sci.*, 2022, **15**, 2776–2805.
44 A. J. Martín, T. Shinagawa and J. P. Ramírez, *Chem*, 2019, **5**, 263–283.
45 Y. Ren, C. Yu, X. Tan, H. Huang, Q. Wei and J. Qiu, *Energy Environ. Sci.*, 2021, **14**, 1176–1193.
46 W. Bi, N. Shaigan, A. Malek, K. Fatih, E. Gyenge and D. P. Wilkinson, *Energy Environ. Sci.*, 2022, **15**, 2259–2287.
47 A. R. Singh, B. A. Rohr, J. A. Schwalbe, M. Cargnello, K. Chan, T. F. Jaramillo, I. Chorkendorff and J. K. Nørskov, *ACS Catal.*, 2016, **7**, 706–709.
48 E. Skúlason, T. Bligaard, S. Gudmundsdóttir, F. Studt, J. Rossmeisl, F. A. Pedersen, T. Vegge, H. Jónsson and J. K. Nørskov, *Phys. Chem. Chem. Phys.*, 2012, **14**, 1235–1245.
49 Y. Wan, J. Xu and R. Lv, *Mater. Today*, 2019, **27**, 69–90.
50 Y. Zhai, Z. Zhu, C. Zhu, K. Chen, X. Zhang, J. Tang and J. Chen, *Mater. Today*, 2020, **38**, 99–113.
51 X. Chen, Y. Guo, X. Du, Y. Zeng, J. Chu, C. Gong, J. Huang, C. Fan, X. Wang and J. Xiong, *Adv. Energy Mater.*, 2019, **10**, 1903172.
52 Y. Lin, J. Liang, H. Li, L. Zhang, T. Mou, T. Li, L. Yue, Y. Ji, Q. Liu, Y. Luo, N. Li, B. Tang, Q. Wu, M. S. Hamdy, D. Ma and X. Sun, *Mater. Today Phys.*, 2022, **22**, 100611.
53 Z. Zhang, X. Feng, Z. Zhang, L. Chen, W. Liu, L. Tong, X. Gao and J. Zhang, *J. Am. Chem. Soc.*, 2024, **146**, 14898–14904.
54 H. Huo, Q. Zhang, F. Liu and K. He, *Environ. Sci. Technol.*, 2013, **47**, 1711–1718.
55 L. Zhang, J. Liang, Y. Wang, T. Mou, Y. Lin, L. Yue, T. Li, Q. Liu, Y. Luo, N. Li, B. Tang, Y. Liu, S. Gao, A. A. Alshehri, X. Guo, D. Ma and X. Sun, *Angew. Chem., Int. Ed.*, 2021, **60**, 25263–25268.
56 N. Gruber and J. N. Galloway, *Nature*, 2008, **451**, 293–296.
57 Y. Zeng, C. Priest, G. Wang and G. Wu, *Small Methods*, 2020, **4**, 2000672.
58 G. F. Mcisaac, M. B. David, G. Z. Gertner and D. A. Goolsby, *Nature*, 2001, **414**, 166–167.
59 D. E. Canfield, A. N. Glazer and P. G. Falkowski, *Science*, 2010, **330**, 192–196.
60 J. O. Lundberg, E. Weitzberg, J. A. Cole and N. Benjamin, *Nat. Rev. Microbiol.*, 2004, **2**, 593–602.
61 Z. W. Seh, J. Kibsgaard, C. F. Dickens, I. Chorkendorff, J. K. Norskov and T. F. Jaramillo, *Science*, 2017, **355**, eaad4998.
62 J. Liu, D. Richards, N. Singh and B. R. Goldsmith, *ACS Catal.*, 2019, **9**, 7052–7064.
63 D. P. Butcher Jr and A. A. Gewirth, *Nano Energy*, 2016, **29**, 457–465.
64 J. Li, G. Zhan, J. Yang, F. Quan, C. Mao, Y. Liu, B. Wang, F. Lei, L. Li, A. W. M. Chan, L. Xu, Y. Shi, Y. Du, W. Hao, P. K. Wong, J. Wang, S. Dou, L. Zhang and J. C. Yu, *J. Am. Chem. Soc.*, 2020, **142**, 7036–7046.
65 Y. Xiong, Y. Wang, J. Zhou, F. Liu, F. Hao and Z. Fan, *Adv. Mater.*, 2024, **36**, 2304021.
66 Y. Shi, Z. Zhao, D. Yang, J. Tan, X. Xin, Y. Liu and Z. Jiang, *Chem. Soc. Rev.*, 2023, **52**, 6938–6956.
67 H. Xu, Y. Ma, J. Chen, W. Zhang and J. Yang, *Chem. Soc. Rev.*, 2022, **51**, 2710–2758.
68 Y. Pang, C. Su, G. Jia, L. Xu and Z. Shao, *Chem. Soc. Rev.*, 2021, **50**, 12744–12787.
69 C. Guo, J. Ran, A. Vasileff and S. Qiao, *Energy Environ. Sci.*, 2018, **11**, 45–56.
70 X. Zhang, C. Pei, Z. Zhao and J. Gong, *Energy Environ. Sci.*, 2024, **17**, 2381–2405.
71 S. Wang, X. Hai, X. Ding, K. Chang, Y. Xiang, X. Meng, Z. Yang, H. Chen and J. Ye, *Adv. Mater.*, 2017, **29**, 1701774.
72 J. G. Howalt, T. Bligaard, J. Rossmeislb and T. Vegge, *Phys. Chem. Chem. Phys.*, 2013, **15**, 7785–7795.
73 J. Rittle and J. C. Peters, *J. Am. Chem. Soc.*, 2016, **138**, 4243–4248.
74 J. Lim, C. A. Fernández, S. W. Lee and M. C. Hatzell, *ACS Energy Lett.*, 2021, **6**, 3676–3685.
75 S. P. Eckel, Z. Zhang, R. Habre, E. B. Rappaport, W. S. Linn, K. Berhane, Y. Zhang, T. M. Bastain and F. D. Gilliland, *Eur. Respir. J.*, 2016, **47**, 1348–1356.
76 L. Ooyang, J. Liang, Y. Luo, D. Zheng, S. Sun, Q. Liu, Md. S. Hamdy, X. Sun and B. Ying, *Chin. J. Catal.*, 2023, **50**, 6–44.
77 X. Peng, Y. Mi, H. Bao, Y. Liu, D. Qi, Y. Qiu, L. Zhuo, S. Zhao, J. Sun, X. Tang, J. Luo and X. Liu, *Nano Energy*, 2020, **78**, 105321.
78 J. Long, S. Chen, Y. Zhang, C. Guo, X. Fu, D. Deng and J. Xiao, *Angew. Chem., Int. Ed.*, 2020, **59**, 9711–9718.
79 P. Liu, J. Liang, J. Wang, L. Zhang, J. Li, L. Yue, Y. Ren, T. Li, Y. Luo, N. Li, B. Tang, Q. Liu, A. M. Asiri, Q. Kong and X. Sun, *Chem. Commun.*, 2021, **57**, 13562–13565.
80 R. Miao, D. Chen, Z. Guo, Y. Zhou, C. Chen and S. Wang, *Appl. Catal., B*, 2024, **344**, 123662.
81 M. T. Groot and M. T. M. Koper, *J. Electroanal. Chem.*, 2004, **562**, 81–94.
82 R. Lange, E. Maisonhaute, R. Robin and V. Vivier, *Electrochem. Commun.*, 2013, **29**, 25–28.
83 D. Sicsic, F. B. Célérier and B. Tribollet, *Eur. J. Inorg. Chem.*, 2014, 6174–6184, DOI: 10.1002/ejic.201402708.

84 Y. Wang, C. Wang, M. Li, Y. Yu and B. Zhang, *Chem. Soc. Rev.*, 2021, **50**, 6720–6733.

85 D. Xu, Y. Li, L. Yin, Y. Ji, J. Niu and Y. Yu, *Front. Environ. Sci. Eng.*, 2018, **12**, 9, DOI: 10.1007/s11783-018-1033-z.

86 J. Gao, B. Jiang, C. Ni, Y. Qi and X. Bi, *Chem. Eng. J.*, 2020, **382**, 123034.

87 A. R. Cook, N. Dimitrijevic, B. W. Dreyfus, D. Meisel, L. A. Curtiss and D. M. Camaioni, *J. Phys. Chem. A*, 2001, **105**, 3658–3666.

88 Y. Li, Y. K. Go, H. Ooka, D. He, F. Jin, S. H. Kim and R. Nakamura, *Angew. Chem., Int. Ed.*, 2020, **59**, 9744–9750.

89 R. Jia, Y. Wang, C. Wang, Y. Ling, Y. Yu and B. Zhang, *ACS Catal.*, 2020, **10**, 3533–3540.

90 M. D. Bartberger, W. Liu, E. Ford, K. M. Miranda, C. Switzer, J. M. Fukuto, P. J. Farmer, D. A. Wink and K. N. Houk, *Proc. Natl. Acad. Sci. U. S. A.*, 2002, **99**, 10958–10963.

91 S. Z. Andersen, V. Čolić, S. Yang, J. A. Schwalbe, A. C. Nielander, J. M. Mcenaney, K. Enemark-Rasmussen, J. G. Baker, A. R. Singh, B. A. Rohr, M. J. Statt, S. J. Blair, S. Mezzavilla, J. Kibsgaard, P. C. K. Vesborg, M. Cargnello, S. F. Bent, T. F. Jaramillo, I. E. L. Stephens, J. K. Nørskov and I. Chorkendorff, *Nature*, 2019, **570**, 504–508.

92 C. Tang and S. Qiao, *Chem. Soc. Rev.*, 2019, **48**, 3166–3180.

93 L. Li, C. Tang, D. Yao, Y. Zheng and S. Qiao, *ACS Energy Lett.*, 2019, **4**, 2111–2116.

94 H. Iriawan, S. Z. Andersen, X. Zhang, B. M. Comer, J. Barrio, P. Chen, A. J. Medford, I. E. L. Stephens, I. Chorkendorff and Y. Shao-Horn, *Nat. Rev. Methods Primers*, 2021, **1**, 56.

95 H. Liu, N. Guijarro and J. Luo, *J. Energy Chem.*, 2021, **61**, 149–154.

96 L. Shi, Y. Yin, S. Wang, X. Xu, H. Wu, J. Zhang, S. Wang and H. Sun, *Appl. Catal., B*, 2020, **278**, 119325.

97 N. C. Kani, A. Prajapati, B. A. Collins, J. D. Goodpaster and M. R. Singh, *ACS Catal.*, 2020, **10**, 14592–14603.

98 N. Lazouski, M. Chung, K. Williams, M. L. Gala and K. Manthiram, *Nat. Catal.*, 2020, **3**, 463–469.

99 F. Hanifpour, A. Sveinbjörnsson, C. P. Canales, E. Skúlason and H. D. Flosadóttir, *Angew. Chem., Int. Ed.*, 2020, **132**, 23138–23142.

100 W. Shan, F. Liu, H. He, X. Shi and C. Zhang, *ChemCatChem*, 2011, **3**, 1286–1289.

101 H. Shen, C. Choi, J. Masa, X. Li, J. Qiu, Y. Jung and Z. Sun, *Chem*, 2021, **7**, 1708–1754.

102 S. H. Yuen and A. G. Pollard, *J. Sci. Food Agric.*, 1952, **3**, 441–447.

103 ASTM D1426-15, Standard Test Methods for Ammonia Nitrogen in Water, 2021, ASTM International, 100 Barr Harbor Drive, PO Box C700, West Conshohocken, PA 19428-2959, United States.

104 W. T. Bolleter, C. J. Bushman and P. W. Tidwell, *Anal. Chem.*, 1961, **33**, 592–594.

105 C. E. Bower and T. H. Hansen, *Can. J. Fish. Aquat. Sci.*, 1980, **37**, 794–798.

106 H. Verdouw, C. J. A. V. Echteld and E. M. J. Dekkers, *Water Res.*, 1978, **12**, 399–402.

107 N. Amornthammarong and J. Zhang, *Anal. Chem.*, 2008, **80**, 1019–1026.

108 X. Gao, Y. Wen, D. Qu, L. An, S. Luan, W. Jiang, X. Zong, X. Liu and Z. Sun, *ACS Sustainable Chem. Eng.*, 2018, **6**, 5342–5348.

109 L. Zhou and C. E. Boyd, *Aquaculture*, 2016, **450**, 187–193.

110 P. Wang, F. Cchang, W. Gao, J. Guo, G. Wu, T. He and P. Chen, *Nat. Chem.*, 2017, **9**, 64–70.

111 E. W. Rice, B. Baird, A. D. Eaton and L. S. Clesceri,*Standard Methods for the Examination of Water and Wastewater*, American Water Works Association, 2012.

112 F. Zhou, L. M. Azofra, M. Ali, M. Kar, A. N. Simonov, C. M. Worth, C. Sun, X. Zhang and D. R. MacFarlane, *Energy Environ. Sci.*, 2017, **10**, 2516–2520.

113 D. Borden and R. F. Giese, *Clays Clay Miner.*, 2001, **49**, 444–445.

114 A. Leduy and R. Samson, *Biotechnol. Lett.*, 1982, **4**, 303–306.

115 R. Peters, M. Baltruweit, T. Grube, R. C. Samsun and D. Stolten, *J. CO_2 Util.*, 2019, **34**, 616–634.

116 X. Li, P. Anderson, H. R. M. Jhong, M. Paster, J. F. Stubbins and P. J. A. Kenis, *Energy Fuels*, 2016, **30**, 5980–5989.

117 W. Lai, Y. Qiao, J. Zhang, Z. Lin and H. Huang, *Energy Environ. Sci.*, 2022, **15**, 3603–3629.

118 J. Na, B. Seo, J. Kim, C. W. Lee, H. Lee, Y. J. Hwang, B. K. Min, D. K. Lee, H. S. Oh and U. Lee, *Nat. Commun.*, 2019, **10**, 5193.

119 L. Gao, X. Cui, C. D. Sewell, J. Li and Z. Lin, *Chem. Soc. Rev.*, 2021, **50**, 8428–8469.

120 S. Verma, S. Lu and P. J. A. Kenis, *Nat. Energy*, 2019, **4**, 466–474.

121 X. Chen, N. Li, Z. Kong, W. Ong and X. Zhao, *Mater. Horiz.*, 2018, **5**, 9–27.

122 S. Shang, W. Xiong, C. Yang, B. Johannessen, R. Liu, H. Y. Hsu, Q. Gu, M. K. H. Leung and J. Shang, *ACS Nano*, 2021, **15**, 9670–9678.

123 J. Zander, J. Timm, M. Weiss and R. Marschall, *Adv. Energy Mater.*, 2022, **12**, 2202403.

124 X. Wang, G. Fan, S. Guo, R. Gao, Y. Guo, C. Han, Y. Gao, J. Zhang, X. Gu and L. Wu, *Angew. Chem., Int. Ed.*, 2024, **63**, e202404258.

125 Y. Zhao, L. Zheng, R. Shi, S. Zhang, X. Bian, F. Wu, X. Cao, G. I. N. Waterhouse and T. Zhang, *Adv. Energy Mater.*, 2020, **10**, 2002199.

126 G. Dong, X. Huang and Y. Bi, *Angew. Chem., Int. Ed.*, 2022, **61**, e202204271.

127 Q. Han, C. Wu, H. Jiao, R. Xu, Y. Wang, J. Xie, Q. Guo and J. Tang, *Adv. Mater.*, 2021, **33**, 2008180.

128 Z. Zhao, R. Tan, Y. Kong, Z. Zhang, S. Qiu, X. Mu and L. Li, *Angew. Chem., Int. Ed.*, 2023, **62**, e202303629.

129 L. Chen, Y. Hao, Y. Guo, Q. Zhang, J. Li, W. Gao, L. Ren, X. Su, L. Hu, N. Zhang, S. Li, X. Feng, L. Gu, Y. Zhang, A. Yin and B. Wang, *J. Am. Chem. Soc.*, 2021, **143**, 5727–5736.

130 Y. Fang, Y. Xue, L. Hui, H. Yu and Y. Li, *Angew. Chem., Int. Ed.*, 2021, **60**, 3170–3174.

131 Y. Zhao, Y. Zhao, G. I. N. Waterhouse, L. Zheng, X. Cao, F. Teng, L. Wu, C. H. Tung, D. O'Hare and T. Zhang, *Adv. Mater.*, 2017, **29**, 1703828.

132 S. Liu, M. Wang, H. Ji, L. Zhang, J. Ni, N. Li, T. Qian, C. Yan and J. Lu, *Adv. Mater.*, 2023, **35**, 2211730.

133 G. N. Schrauzer and T. D. Guth, *J. Am. Chem. Soc.*, 1977, **99**, 7189–7193.

134 Z. Zhao, D. Wang, R. Gao, G. Wen, M. Feng, G. Song, J. Zhu, D. Luo, H. Tan, X. Ge, W. Zhang, Y. Zhang, L. Zheng, H. Li and Z. Chen, *Angew. Chem., Int. Ed.*, 2021, **60**, 11910–11918.

135 Y. Zhao, Y. Zhao, R. Shi, B. Wang, G. I. N. Waterhouse, L. Wu, C. H. Tung and T. Zhang, *Adv. Mater.*, 2019, **31**, 1806482.

136 S. Tan, H. Feng, Q. Zheng, X. Cui, J. Zhao, Y. Luo, J. Yang, B. Wang and J. G. Hou, *J. Am. Chem. Soc.*, 2020, **142**, 826–834.

137 C. Xu, Y. Zhang, J. Chen, S. Li, Y. Zhang and G. Qin, *Sci. China Mater.*, 2021, **64**, 128–136.

138 W. Zhang, H. He, H. Li, L. Duan, L. Zu, Y. Zhai, W. Li, L. Wang, H. Fu and D. Zhao, *Adv. Energy Mater.*, 2021, **11**, 2003303.

139 C. Liu, D. Hao, J. Ye, S. Ye, F. Zhou, H. Xie, G. Qin, J. Xu, J. Liu, S. Li and C. Sun, *Adv. Energy Mater.*, 2023, **13**, 2204126.

140 P. Xia, X. Pan, S. Jiang, J. Yu, B. He, P. M. Ismail, W. Bai, J. Yang, L. Yang, H. Zhang, M. Cheng, H. Li, Q. Zhang, C. Xiao and Y. Xie, *Adv. Mater.*, 2022, **34**, 2200563.

141 W. Wang, H. Zhou, Y. Liu, S. Zhang, Y. Zhang, G. Wang, H. Zhang and H. Zhao, *Small*, 2020, **16**, 1906880.

142 Y. Guan, H. Wen, K. Cui, Q. Wang, W. Gao, Y. Cai, Z. Cheng, Q. Pei, Z. Li, H. Cao, T. He, J. Guo and P. Chen, *Nat. Chem.*, 2024, **16**, 373–379.

143 J. Li, R. Chen, J. Wang, Y. Zhou, G. Yang and F. Dong, *Nat. Commun.*, 2022, **13**, 1098.

144 R. Chen, S. Shen, K. Wang and F. Dong, *Proc. Natl. Acad. Sci. U. S. A.*, 2023, **120**, e2312550120.

145 Y. Wang and T. J. Meyer, *Chem*, 2019, **5**, 496–497.

146 Y. Yang, S. Wang, H. Wen, T. Ye, J. Chen, C. Li and M. Du, *Angew. Chem., Int. Ed.*, 2019, **58**, 15362–15366.

147 B. Cui, J. Zhang, S. Liu, X. Liu, W. Xiang, L. Liu, H. Xin, M. J. Leflerc and S. Licht, *Green Chem.*, 2017, **19**, 298–304.

148 N. Cao and G. Zheng, *Nano Res.*, 2018, **11**, 2992–3008.

149 M. Wang, S. Liu, T. Qian, J. Liu, J. Zhou, H. Ji, J. Xiong, J. Zhong and C. Yan, *Nat. Commun.*, 2019, **10**, 341.

150 Y. Lin, S. Zhang, Z. Xue, J. Zhang, H. Su, T. Zhao, G. Zhai, X. Li, M. Antonietti and J. Chen, *Nat. Commun.*, 2019, **10**, 4380.

151 G. Lin, Q. Ju, X. Guo, W. Zhao, S. Adimi, J. Ye, Q. Bi, J. Wang, M. Yang and F. Huang, *Adv. Mater.*, 2021, **33**, 2007509.

152 W. Qiu, X. Xie, J. Qiu, W. Fang, R. Liang, X. Ren, X. Ji, G. Cui, A. M. Asiri, G. Cui, B. Tang and X. Sun, *Nat. Commun.*, 2018, **9**, 3485.

153 J. Wang, L. Yu, L. Hu, G. Chen, H. Xin and X. Feng, *Nat. Commun.*, 2018, **9**, 1795.

154 B. A. MacKay and M. D. Fryzuk, *Chem. Rev.*, 2004, **104**, 385–402.

155 H. Qian, S. Xu, J. Cao, F. Ren, W. Wei, J. Meng and L. Wu, *Nat. Sustain.*, 2021, **4**, 417–425.

156 K. Li, D. J. Jacob, H. Liao, J. Zhu, V. Shah, L. Shen, K. H. Bates, Q. Zhang and S. Zhai, *Nat. Geosci.*, 2019, **12**, 906–910.

157 S. Ozgen, S. Cernuschi and S. Caserini, *Renewable Sustainable Energy Rev.*, 2021, **135**, 110113.

158 L. Pagalan, C. Bickford, W. Weikum, B. Lanphear, M. Brauer, N. Lanphear, G. E. Hanley, T. F. Oberlander and M. Winters, *JAMA Pediatr.*, 2019, **173**, 86–92.

159 L. Han, S. Cai, M. Gao, J. Y. Hasegawa, P. Wang, J. Zhang, L. Shi and D. Zhang, *Chem. Rev.*, 2019, **119**, 10916–10976.

160 A. M. Beale, F. Gao, I. L. Gonzalez, C. H. F. Peden and J. Szanyi, *Chem. Soc. Rev.*, 2015, **44**, 7371–7405.

161 C. Liu, Y. Wang and B. Zhang, *Sci. China: Chem.*, 2020, **63**, 1173–1174.

162 K. Otsuka, H. Sawada and I. Yamanaka, *J. Electrochem. Soc.*, 1996, **143**, 3491–3497.

163 P. D. Schepper, V. A. Danilov and J. F. M. Denayer, *Int. J. Energy Res.*, 2016, **40**, 1355–1366.

164 M. Tursun and C. Wu, *Inorg. Chem.*, 2022, **61**, 17448–17458.

165 J. Choi, B. H. R. Suryanto, D. Wang, H. Du, R. Y. Hodgetts, F. M. F. Vallana, D. R. Macfarlane and A. N. Simonov, *Nat. Commun.*, 2020, **11**, 5546.

166 S. S. Markandaraj, T. Markandaraj and S. Shanmugam, *Adv. Sci.*, 2022, **9**, 2201410.

167 B. H. Ko, B. Hasa, H. Shin, Y. Zhao and F. Jiao, *J. Am. Chem. Soc.*, 2022, **144**, 1258–1266.

168 X. Li, K. Chen, X. Lu, D. Ma and K. Chu, *Chem. Eng. J.*, 2023, **454**, 140333.

169 Z. Kou, K. Wang, Z. Liu, L. Zeng, Z. Li, B. Yang, L. Lei, C. Yuan and Y. Hou, *Small Struct.*, 2022, **3**, 2100153.

170 J. Liang, Q. Zhou, T. Mou, H. Chen, L. Yue, Y. Luo, Q. Liu, M. S. Hamdy, A. A. Alshehri, F. Gong and X. Sun, *Nano Res.*, 2022, **15**, 4008–4013.

171 H. J. Chun, V. Apaja, A. Clayborne, K. Honkala and J. Greeley, *ACS Catal.*, 2017, **7**, 3869–3882.

172 Y. Li, C. Cheng, S. Han, Y. Huang, X. Du, B. Zhang and Y. Yu, *ACS Energy Lett.*, 2022, **7**, 1187–1194.

173 Y. Li, S. Zhang, W. Cheng, Y. Chen, D. Luan, S. Gao and X. (David) Lou, *Adv. Mater.*, 2022, **34**, 2105204.

174 Y. Yan, B. Huang, J. Wang, H. Wang and W. Cai, *J. Catal.*, 2007, **249**, 311–317.

175 P. Zhou, N. Li, Y. Chao, W. Zhang, F. Lv, K. Wang, W. Yang, P. Gao and S. Guo, *Angew. Chem., Int. Ed.*, 2019, **58**, 14184–14188.

176 J. Mao, C. He, J. Pei, W. Chen, D. He, Y. He, Z. Zhuang, C. Chen, Q. Peng, D. Wang and Y. Li, *Nat. Commun.*, 2018, **9**, 4958.

177 H. Zhang, P. An, W. Zhou, B. Guan, P. Zhang, J. Dong and X. (David) Lou, *Sci. Adv.*, 2018, **4**, eaao6657.

178 H. Zhang, Y. Li, C. Cheng, J. Zhou, P. Yin, H. Wu, Z. Liang, J. Zhang, Q. Yun, A. Wang, L. Zhu, B. Zhang, W. Cao, X. Meng, J. Xia, Y. Yu and Q. Lu, *Angew. Chem., Int. Ed.*, 2023, **62**, e202213351.

179 H. Liu, K. Xiang, B. Yang, X. Xie, D. Wang, C. Zhang, Z. Liu, S. Yang, C. Liu, J. Zou and L. Chai, *Environ. Sci. Pollut. Res.*, 2017, **24**, 14249–14258.

180 L. Zhang, Q. Zhou, J. Liang, L. Yue, T. Li, Y. Luo, Q. Liu, N. Li, B. Tang, F. Gong, X. Guo and X. Sun, *Inorg. Chem.*, 2022, **61**, 8096–8102.

181 A. Clayborne, H. J. Chun, R. B. Rankin and J. Greeley, *Angew. Chem., Int. Ed.*, 2015, **127**, 8373–8376.

182 S. Deshpande and J. Greeley, *ACS Catal.*, 2020, **10**, 9320–9327.

183 B. He, P. Lv, D. Wu, X. Li, R. Zhu, K. Chu, D. Ma and Y. Jia, *J. Mater. Chem. A*, 2022, **10**, 18690–18700.

184 G. Meng, T. Wei, W. Liu, W. Li, S. Zhang, W. Liu, Q. Liu, H. Bao, J. Luog and X. Liu, *Chem. Commun.*, 2022, **58**, 8097–8100.

185 Y. Feng, Q. Shao, F. Lv, L. Bu, J. Guo, S. Guo and X. Huang, *Adv. Sci.*, 2020, **7**, 1800178.

186 L. Li, C. Tang, B. Xia, H. Jin, Y. Zheng and S. Qiao, *ACS Catal.*, 2019, **9**, 2902–2908.

187 J. Liang, P. Liu, Q. Li, T. Li, L. Yue, Y. Luo, Q. Liu, N. Li, B. Tang, A. A. Alshehri, I. Shakir, P. O. Agboola, C. Sun and X. Sun, *Angew. Chem., Int. Ed.*, 2022, **61**, e202202087.

188 G. Chen, X. Cao, S. Wu, X. Zeng, L. Ding, M. Zhu and H. Wang, *J. Am. Chem. Soc.*, 2017, **139**, 9771–9774.

189 N. Q. Tran, L. T. Duy, D. C. Truong, B. T. N. Le, B. T. Phan, Y. Cho, X. Liu and H. Lee, *Chem. Commun.*, 2022, **58**, 5257–5260.

190 E. J. Zakem, A. A. Haj, M. J. Church, G. L. Dijken, S. Dutkiewicz, S. Q. Foster, R. W. Fulweiler, M. M. Mills and M. J. Follows, *Nat. Commun.*, 2018, **9**, 1206.

191 D. He, Y. Li, H. Ooka, Y. K. Go, F. Jin, S. H. Kim and R. Nakamura, *J. Am. Chem. Soc.*, 2018, **140**, 2012–2015.

192 S. Liu, L. Cui, S. Yin, H. Ren, Z. Wang, Y. Xu, X. Li, L. Wang and H. Wang, *Appl. Catal., B*, 2022, **319**, 121876.

193 H. Li, C. Yan, H. Guo, K. Shin, S. M. Humphrey, C. J. Werth and G. Henkelman, *ACS Catal.*, 2020, **10**, 7915–7921.

194 Y. Arikawa, Y. Otsubo, H. Fujino, S. Horiuchi, E. Sakuda and K. Umakoshi, *J. Am. Chem. Soc.*, 2018, **140**, 842–847.

195 Y. Guo, J. R. Stroka, B. Kandemir, C. E. Dickerson and K. L. Bren, *J. Am. Chem. Soc.*, 2018, **140**, 16888–16892.

196 R. Zhang, S. Zhang, Y. Guo, C. Li, J. Liu, Z. Huang, Y. Zhao, Y. Li and C. Zhi, *Energy Environ. Sci.*, 2022, **15**, 3024–3032.

197 W. Qiu, X. Chen, Y. Liu, D. Xiao, P. Wang, R. Li, K. Liu, Z. Jin and P. Li, *Appl. Catal., B*, 2022, **315**, 121548.

198 Y. Wang, W. Zhou, R. Jia, Y. Yu and B. Zhang, *Angew. Chem., Int. Ed.*, 2020, **59**, 5350–5354.

199 J. Lim, C. Liu, J. Park, Y. Liu, T. P. Senftle, S. W. Lee and M. C. Hatzell, *ACS Catal.*, 2021, **11**, 7568–7577.

200 H. Shin, S. Jung, S. Bae, W. Lee and H. Kim, *Environ. Sci. Technol.*, 2014, **48**, 12768–12774.

201 C. Fierro, *J. Phys. Chem.*, 1988, **92**, 4401–4405.

202 S. Seraj, P. Kunal, H. Li, G. Henkelman, S. M. Humphrey and C. J. Werth, *ACS Catal.*, 2017, **7**, 3268–3276.

203 H. Li, S. Guo, K. Shin, M. S. Wong and G. Henkelman, *ACS Catal.*, 2019, **9**, 7957–7966.

204 S. García, L. Zhang, G. W. Piburn, G. Henkelman and S. M. Humphrey, *ACS Nano*, 2014, **8**, 11512–11521.

205 S. E. Braley, J. Xie, Y. Losovyj and J. M. Smith, *J. Am. Chem. Soc.*, 2021, **143**, 7203–7208.

206 J. R. Stroka, B. Kandemir, E. M. Matson and K. L. Bren, *ACS Catal.*, 2020, **10**, 13968–13972.

207 Q. Chen, X. An, Q. Liu, X. Wu, L. Xie, J. Zhang, W. Yao, M. S. Hamdy, Q. Kong and X. Sun, *Chem. Commun.*, 2022, **58**, 517–520.

208 Y. Wang, A. Xu, Z. Wang, L. Huang, J. Li, F. Li, J. Wicks, M. Luo, D. H. Nam, C. S. Tan, Y. Ding, J. Wu, Y. Lum, C. T. Dinh, D. Sinton, G. Zheng and E. H. Sargent, *J. Am. Chem. Soc.*, 2020, **142**, 5702–5708.

209 L. Mattarozzi, S. Cattarin, N. Comisso, P. Guerriero, M. Musiani, L. V. Gómez and E. Verlato, *Electrochim. Acta*, 2013, **89**, 488–496.

210 L. Li, C. Tang, X. Cui, Y. Zheng, X. Wang, H. Xu, S. Zhang, T. Shao, K. Davey and S. Qiao, *Angew. Chem., Int. Ed.*, 2021, **60**, 14131–14137.

211 X. Li, Z. Li, L. Zhang, D. Zhao, J. Li, S. Sun, L. Xie, Q. Liu, A. A. Alshehri, Y. Luo, Y. Liao, Q. Kong and X. Sun, *Nanoscale*, 2022, **14**, 13073–13077.

212 G. Wen, J. Liang, L. Zhang, T. Li, Q. Liu, X. An, X. Shi, Y. Liu, S. Gao, A. M. Asiri, Y. Luo, Q. Kong and X. Sun, *J. Colloid Interface Sci.*, 2022, **606**, 1055–1063.

213 C. Wang, W. Zhou, Z. Sun, Y. Wang, B. Zhang and Y. Yu, *J. Mater. Chem. A*, 2021, **9**, 239–243.

214 S. Ye, Z. Chen, G. Zhang, W. Chen, C. Peng, X. Yang, L. Zheng, Y. Li, X. Ren, H. Cao, D. Xue, J. Qiu, Q. Zhang and J. Liu, *Energy Environ. Sci.*, 2022, **15**, 760–770.

215 T. Ling, D. Yan, H. Wang, Y. Jiao, Z. Hu, Y. Zheng, L. Zheng, J. Mao, H. Liu, X. Du, M. Jaroniec and S. Qiao, *Nat. Commun.*, 2017, **8**, 1509.

216 F. Lei, L. Zhang, Y. Sun, L. Liang, K. Liu, J. Xu, Q. Zhang, B. Pan, Y. Luo and Y. Xie, *Angew. Chem., Int. Ed.*, 2015, **54**, 9266–9270.

217 J. Sun, D. Alam, R. Daiyan, H. Masood, T. Zhang, R. Zhou, P. J. Cullen, E. C. Lovell, A. Jalili and R. Amal, *Energy Environ. Sci.*, 2021, **14**, 865–872.

218 I. Katsounaros, M. Dortsiou and G. Kyriacou, *J. Hazard. Mater.*, 2009, **171**, 323–327.

219 R. Chauhan and V. C. Srivastava, *Chem. Eng. J.*, 2020, **386**, 122065.

220 M. Teng, J. Ye, C. Wan, G. He and H. Chen, *Ind. Eng. Chem. Res.*, 2022, **61**, 14731–14746.

221 G. Chen, Y. Yuan, H. Jiang, S. Ren, L. Ding, L. Ma, T. Wu, J. Lu and H. Wang, *Nat. Energy*, 2020, **5**, 605–613.

222 D. Xu, Y. Li, L. Yin, Y. Ji, J. Niu and Y. Yu, *Front. Environ. Sci. Eng.*, 2018, **12**, 9, DOI: 10.1007/s11783-018-1033-z.

223 H. Liu, J. Park, Y. Chen, Y. Qiu, Y. Cheng, K. Srivastava, S. Gu, B. H. Shanks, L. T. Roling and W. Li, *ACS Catal.*, 2021, **11**, 8431–8442.

224 M. Duca and M. T. M. Koper, *Energy Environ. Sci.*, 2012, **5**, 9726–9742.

225 E. Murphy, Y. Liu, I. Matanovic, S. Guo, P. Tieu, Y. Huang, A. Ly, S. Das, I. Zenyuk, X. Pan, E. Spoerke and P. Atanassov, *ACS Catal.*, 2022, **12**, 6651–6662.

226 S. Guo, K. Heck, S. Kasiraju, H. Qian, Z. Zhao, L. C. Grabow, J. T. Miller and M. S. Wong, *ACS Catal.*, 2018, **8**, 503–515.

227 S. E. Bae, K. L. Stewart and A. A. Gewirth, *J. Am. Chem. Soc.*, 2007, **129**, 10171–10180.

228 F. Chen, Z. Wu, S. Gupta, D. J. Rivera, S. V. Lambeets, S. Pecaut, J. Y. T. Kim, P. Zhu, Y. Z. Finfrock, D. M. Meira, G. King, G. Gao, W. Xu, D. A. Cullen, H. Zhou, Y. Han, D. E. Perea, C. L. Muhich and H. Wang, *Nat. Nanotechnol.*, 2022, **17**, 759–767.

229 H. Liu, X. Lang, C. Zhu, J. Timoshenko, M. Rüscher, L. Bai, N. Guijarro, H. Yin, Y. Peng, J. Li, Z. Liu, W. Wang, B. R. Cuenya and J. Luo, *Angew. Chem., Int. Ed.*, 2022, **61**, e202202556.

230 R. Zhang, D. Shuai, K. A. Guy, J. R. Shapley, T. J. Strathmann and C. J. Werth, *ChemCatChem*, 2013, **5**, 313–321.

231 Y. Wang, H. Li, W. Zhou, X. Zhang, B. Zhang and Y. Yu, *Angew. Chem., Int. Ed.*, 2022, **61**, e202202604.

232 X. Deng, Y. Yang, L. Wang, X. Fu and J. Luo, *Adv. Sci.*, 2021, **8**, 2004523.

233 R. Amaral and N. Y. Dzade, *Mater. Today Commun.*, 2024, **38**, 107824.

234 J. F. Callejas, C. G. Read, C. W. Roske, N. S. Lewis and R. E. Schaak, *Chem. Mater.*, 2016, **28**, 6017–6044.

235 R. Prins and M. E. Bussell, *Catal. Lett.*, 2012, **142**, 1413–1436.

236 Y. Yang, C. O. Hernández, V. A. P. O'Shea, J. M. Coronado and D. P. Serrano, *ACS Catal.*, 2012, **2**, 592–598.

237 W. R. A. M. Robinson, J. N. M. Gestel, T. I. Korányi, S. Eijsbouts, A. M. van der Kraan, J. A. R. van Veen and V. H. J. Beer, *J. Catal.*, 1996, **161**, 539–550.

238 L. Wei, D. Liu, B. A. Rosales, J. W. Evans and J. Vela, *ACS Catal.*, 2020, **10**, 3618–3628.

239 R. Zhang, Y. Guo, S. Zhang, D. Chen, Y. Zhao, Z. Huang, L. Ma, P. Li, Q. Yang, G. Liang and C. Zhi, *Adv. Energy Mater.*, 2022, **12**, 2103872.

240 I. Katsounaros, D. Ipsakis, C. Polatides and G. Kyriacou, *Electrochim. Acta*, 2006, **52**, 1329–1338.

241 M. Dortsiou and G. Kyriacou, *J. Electroanal. Chem.*, 2009, **630**, 69–74.

242 Z. Wu, M. Karamad, X. Yong, Q. Huang, D. A. Cullen, P. Zhu, C. Xia, Q. Xiao, M. Shakouri, F. Chen, J. Y. Kim, Y. Xia, K. Heck, Y. Hu, M. S. Wong, Q. Li, I. Gates, S. Siahrostami and H. Wang, *Nat. Commun.*, 2021, **12**, 2870.

243 Z. Zheng, L. Qi, Y. Xue and Y. Li, *Nano Today*, 2022, **43**, 101431.

244 Y. Xue, Q. Yu, Q. Ma, Y. Chen, C. Zhang, W. Teng, J. Fan and W. Zhang, *Environ. Sci. Technol.*, 2022, **56**, 14797–14807.

245 J. Liu, M. S. Kelley, W. Wu, A. Banerjee, A. P. Douvalis, J. Wu, Y. Zhang, G. C. Schatz and M. G. Kanatzidis, *Proc. Natl. Acad. Sci. U. S. A.*, 2016, **113**, 5530–5535.

246 Y. Song, D. Johnson, R. Peng, D. K. Hensley, P. V. Bonnesen, L. Liang, J. Huang, F. Yang, F. Zhang, R. Qiao, A. P. Baddorf, T. J. Tschaplinski, N. L. Engle, M. C. Hatzell, Z. Wu, D. A. Cullen, H. M. Meyer III, B. G. Sumpter and A. J. Rondinonoe, *Sci. Adv.*, 2018, **4**, e1700336.

247 C. Li, T. Wang, Z. Zhao, W. Yang, J. Li, A. Li, Z. Yang, G. A. Ozin and J. Gong, *Angew. Chem., Int. Ed.*, 2018, **57**, 5278–5282.

248 B. Zhou, P. Ou, N. Pant, S. Cheng, S. Vanka, S. Chu, R. T. Rashid, G. Botton, J. Song and Z. Mi, *Proc. Natl. Acad. Sci. U. S. A.*, 2020, **117**, 1330–1338.

249 H. Fu, P. Varadhan, M. Tsai, W. Li, Q. Ding, C. Lin, M. Bonifazi, A. Fratalocchi, S. Jin and J. He, *Nano Energy*, 2020, **70**, 104478.

250 J. Zheng, Y. Lyu, M. Qiao, R. Wang, Y. Zhou, H. Li, C. Chen, Y. Li, H. Zhou, S. Jiang and S. Wang, *Chem*, 2019, **5**, 617–633.

251 M. G. Walter, E. L. Warren, J. R. Mckone, S. W. Boettcher, Q. Mi, E. A. Santori and N. S. Lewis, *Chem. Rev.*, 2010, **110**, 6446–6473.

252 J. Hou, M. Yang and J. Zhang, *Nanoscale*, 2020, **12**, 6900–6920.

253 K. Peramaiah, V. Ramalingam, H. Fu, M. M. Alsabban, R. Ahmad, L. Cavallo, V. Tung, K. Huang and J. He, *Adv. Mater.*, 2021, **33**, 2100812.

254 Y. J. Jang, A. E. Lindberg, M. A. Lumley and K. S. Choi, *ACS Energy Lett.*, 2020, **5**, 1834–1839.

255 S. Zhou, K. Sun, C. Y. Toe, J. Yin, J. Huang, Y. Zeng, D. Zhang, W. Chen, O. F. Mohammed, X. Hao and R. Amal, *Adv. Mater.*, 2022, **34**, 2201670.

256 H. E. Kim, J. Kim, E. C. Ra, H. Zhang, Y. J. Jang and J. S. Lee, *Angew. Chem., Int. Ed.*, 2022, **61**, e202204117.

257 D. Liu, J. Wang, S. Bian, Q. Liu, Y. Gao, X. Wang, P. K. Chu and X. Yu, *Adv. Funct. Mater.*, 2020, **30**, 2002731.

258 H. Huang, W. Tu, L. Fang, Y. Xiao, F. Niu, H. Zhu, X. Zhu, L. Wang, Y. Xiong, J. Feng, H. Li, M. Zhang, Y. Zhang, Y. Yao, Y. Zhou, H. Li and Z. Zou, *ACS Energy Lett.*, 2023, **8**, 4235–4241.

259 A. Tayyebi, R. Mehrotra, M. A. Mubarok, J. Kim, M. Zafari, M. Tayebi, D. Oh, S. H. Lee, J. E. Matthews, S. W. Lee, T. J. Shin, G. Lee, T. F. Jaramillo, S. Y. Jang and J. W. Jang, *Nat. Catal.*, 2024, **7**, 510–521.

260 M. S. Iqbal, Y. Ruan, R. Iftikhar, F. Z. Khan, W. Li, L. Hao, A. W. Robertson, G. Percoco and Z. Sun, *Ind. Chem. Mater.*, 2023, **1**, 563–581.

261 J. Kibsgaard, J. K. Nørskov and I. Chorkendorff, *ACS Energy Lett.*, 2019, **4**, 2986–2988.

262 L. F. Greenlee, J. N. Renner and S. L. Foster, *ACS Catal.*, 2018, **8**, 7820–7827.

263 X. Fu, J. Zhang and Y. Kang, *Chem. Catal.*, 2022, **2**, 2590–2613.

264 F. Fichter, P. Girard and H. Erlenmeyer, *Helv. Chim. Acta*, 1930, **13**, 1228–1236.

265 E. Peled, *J. Electrochem. Soc.*, 1979, **126**, 2047.

266 A. Tsuneto, A. Kudo and T. Sakata, *Chem. Lett.*, 1993, 851–854.

267 A. Tsuneto, A. Kudo and T. Sakata, *J. Electroanal. Chem.*, 1994, **367**, 183–188.

268 J. M. McEnaney, A. R. Singh, J. A. Schwalbe, J. Kibsgaard, J. C. Lin, M. Cargnello, T. F. Jaramillo and J. K. Nørskov, *Energy Environ. Sci.*, 2017, **10**, 1621–1630.

269 W. Chang, A. Jain, F. Rezaie and K. Manthiram, *Nat. Catal.*, 2024, **7**, 231–241.

270 E. F. Mcfarlane and F. C. Tompkins, *Trans. Faraday Soc.*, 1962, **58**, 997–1007.

271 A. N. Dey, *Thin Solid Films*, 1977, **43**, 131–171.

272 R. Subbaraman, D. Tripkovic, D. Strmcnik, K. C. Chang, M. Uchimura, A. P. Paulikas, V. Stamenkovic and N. M. Markovic, *Science*, 2011, **334**, 1256–1260.

273 N. Lazouski, Z. J. Schiffer, K. Williams and K. Manthiram, *Joule*, 2019, **3**, 1127–1139.

274 K. Li, S. Z. Andersen, M. J. Statt, M. Saccoccio, V. J. Bukas, K. Krempl, R. Sažinas, J. B. Pedersen, V. Shadravan, Y. Zhou, D. Chakraborty, J. Kibsgaard, P. C. K. Vesborg,

J. K. Nørskov and I. Chorkendorff, *Science*, 2021, **374**, 1593–1597.

275 B. H. R. Suryanto, K. Matuszek, J. Choi, R. Y. Hodgetts, H. Du, J. M. Bakker, C. S. M. Kang, P. V. Cherepanov, A. N. Simonov and D. R. Macfarlane, *Science*, 2021, **372**, 1187–1191.

276 S. Z. Andersen, M. J. Statt, V. J. Bukas, S. G. Shapel, J. B. Pedersen, K. Krempl, M. Saccoccio, D. Chakraborty, J. Kibsgaard, P. C. K. Vesborg, J. Nørskov and I. Chorkendorff, *Energy Environ. Sci.*, 2020, **13**, 4291–4300.

277 G. Soloveichik, in 2019 AIChE Annual Meeting (AIChE, 2019). **https://arpa-e.energy.gov/technologies/programs/refuel**.

278 K. Steinberg, X. Yuan, C. K. Klein, N. Lazouski, M. Mecklenburg, K. Manthiram and Y. Li, *Nat. Energy*, 2023, **8**, 138–148.

279 R. Tort, O. Westhead, M. Spry, B. J. V. Davies, M. P. Ryan, M. M. Titirici and I. E. L. Stephens, *ACS Energy Lett.*, 2023, **8**, 1003–1009.

280 X. Fu, J. B. Pedersen, Y. Zhou, M. Saccoccio, S. Li, R. Sažinas, K. Li, S. Z. Andersen, A. Xu, N. H. Deissler, J. B. V. Mygind, C. Wei, J. Kibsgarrd, P. K. Vesborg, J. K. Nørskov and I. Chorkendorff, *Science*, 2023, **379**, 707–712.

281 X. Fu, A. Xu, J. B. Pedersen, S. Li, R. Sažinas, Y. Zhou, S. Z. Andersen, M. Saccoccio, N. H. Deissler, J. B. V. Mygind, J. Kibsgaard, P. C. K. Vesborg, J. K. Nørskov and I. Chorkendorff, *Nat. Commun.*, 2024, **15**, 2417.

282 S. Li, Y. Zhou, K. Li, M. Saccoccio, R. Sažinas, S. Z. Andersen, J. B. Pedersen, X. Fu, V. Shadravan, D. Chakraborty, J. Kibsgaard, P. C. K. Vesborg, J. K. Nørskov and I. Chorkendorff, *Joule*, 2022, **6**, 2083–2101.

283 H. Du, M. Chatti, R. Y. Hodgetts, P. V. Cherepanov, C. K. Nguyen, K. Matuszek, D. R. MacFarlane and A. N. Simonov, *Nature*, 2022, **609**, 722–727.

284 X. Cai, X. Li, J. You, F. Yang, Z. Shadike, S. Qin, L. Luo, Y. Guo, X. Yan, S. Shen, G. Wei, Z. J. Xu and J. Zhang, *J. Am. Chem. Soc.*, 2023, **145**, 25716–25725.

285 S. Li, Y. Zhou, X. Fu, J. B. Pedersen, M. Saccoccio, S. Z. Andersen, K. E. Rasmussen, P. J. Kempen, C. D. Damsgaard, A. Xu, R. Sažinas, J. B. V. Mygind, N. H. Deissler, J. Kibsgaard, P. C. K. Vesborg, J. K. Nørskov and I. Chorkendorff, *Nature*, 2024, **629**, 92–97.

286 X. Fu, V. A. Niemann, Y. Zhou, S. Li, K. Zhang, J. B. Pedersen, M. Saccoccio, S. Z. Andersen, K. E. Rasmussen, P. Benedek, A. Xu, N. H. Deissler, J. B. V. Mygind, A. C. Nielander, J. Kibsgaard, P. C. K. Vesborg, J. K. Nørskov, T. F. Jaramillo and I. Chorkendorff, *Nat. Mater.*, 2024, **23**, 101–107.

287 K. Li, S. G. Shapel, D. Hochfilzer, J. B. Pedersen, K. Krempl, S. Z. Andersen, R. Sažinas, M. Saccoccio, S. Li, D. Chakraborty, J. Kibsgaard, P. C. K. Vesborg, J. K. Nørskov and I. Chorkendorff, *ACS Energy Lett.*, 2022, **7**, 36–41.

288 C. Chen, Y. Li and P. Yang, *Joule*, 2021, **5**, 737–742.

289 Y. Li, Y. Ji, Y. Zhao, J. Chen, S. Zheng, X. Sang, B. Yang, Z. Li, L. Lei, Z. Wen, X. Feng and Y. Hou, *Adv. Mater.*, 2022, **34**, 2202240.

290 X. Cai, Z. Shadike, X. Cai, X. Li, L. Luo, L. An, J. Yin, G. Wei, F. Yang, S. Shen and J. Zhang, *Energy Environ. Sci.*, 2023, **16**, 3063–3073.

291 S. Chen, S. Perathoner, C. Ampelli, C. Mebrahtu, D. Su and G. Centi, *ACS Sustainable Chem. Eng.*, 2017, **5**, 7393–7400.

292 J. Shao, H. Jing, P. Wei, X. Fu, L. Pang, Y. Song, K. Ye, M. Li, L. Jiang, J. Ma, R. Li, R. Si, Z. Peng, G. Wang and J. Xiao, *Nat. Energy*, 2023, **8**, 1273–1283.

293 D. Liu, Z. Meng, Y. Zhu, X. Sun, X. Deng, M. Shi, Q. Hao, X. Kang, T. Dai, H. Zhong, J. Yan and Q. Jiang, *Angew. Chem., Int. Ed.*, 2024, **63**, e202315238.

294 J. C. Bui, E. W. Lees, D. H. Marin, T. N. Stovall, L. Chen, A. Kusoglu, A. C. Nielander, T. F. Jaramillo, S. W. Boettcher, A. T. Bell and A. Z. Weber, *Nat. Chem Eng.*, 2024, **1**, 45–60.

295 Z. Xu, L. Wan, Y. Liao, M. Pang, Q. Xu, P. Wang and B. Wang, *Nat. Commun.*, 2023, **14**, 1619.

296 L. Mi, Q. Huo, J. Cao, X. Chen, H. Yang, Q. Hu and C. He, *Adv. Energy Mater.*, 2022, **12**, 2202247.

297 J. Li, B. Sheng, Y. Chen, J. Yang, P. Wang, Y. Li, T. Yu, H. Pan, L. Qiu, Y. Li, J. Song, L. Zhu, X. Wang, Z. Huang and B. Zhou, *Nat. Commun.*, 2024, **15**, 7393.

298 L. Mi, Q. Huo, J. Cao, X. Chen, H. Yang, Q. Hu, C. He, J. Wang, G. Ran, J. Gao, D. Li, G. I. N. Waterhouse, R. Shi, W. Zhang, J. Tang, L. Wu, Y. Zhao and T. Zhang, *Adv. Mater.*, 2025, **37**, 2420199.

299 Y. Li, Q. Zhang, H. Dai, D. He, Z. Ke and X. Xiao, *Energy Environ. Sci.*, 2024, **17**, 9233–9243.

300 A. Zabelina, E. Miliutina, J. Dedek, A. Trelin, D. Zabelin, R. Valiev, R. Ramazanov, V. Burtsev, D. Popelkova, M. Stastny, V. Svorcik and O. Lyutakov, *ACS Catal.*, 2023, **13**, 10916–10926.

301 Y. Fang, M. Li, Y. Gao, Y. Wen and B. Shan, *Angew. Chem., Int. Ed.*, 2025, **64**, e202415729.

302 P. Wang, P. Li, Z. Pan, K. Liu, M. Xie, L. Zhou, M. Zhou, G. Yu and Z. Jin, *Nat. Commun.*, 2025, **16**, 5581.